POLITECNICO DI TORINO

Faculty of Environmental Engineering

Master's Degree Program in Natural Hazards and Civil Defense

Master's thesis

Temperature, pressure, and carbon dioxide trends in karst environment.

Bossea cave case study

Professors:

Prof. Adriano Fiorucci

Prof. Bartolomeo Vigna

Candidate:

Giulia Messina

A.a. 2022/2023

Summary

LIST OF FIGURES

LIST OF TABLES

1 Introduction

Karst is a distinctive landscape that is formed by the dissolution of soluble rocks such as limestone and dolomite. Karst landscapes are characterized by unique surface and subsurface features, including sinkholes, underground rivers, caves, and disappearing streams. These features are created as rainwater and groundwater dissolve the soluble rock, creating underground net of channels and caves. Karst landscapes are of fundamental importance for biodiversity (Medellin et al., 2017), water resources as an important source of fresh water (Stevanović, 2019), carbon storage (Pla et al., 2016) as important sinks for carbon dioxide and finally economic values, as popular tourism destinations, generating income for local communities through the provision of accomodation, food and beverages, and other services(Wang et al., 2019).

Bossea Cave, also known as the Grotta di Bossea, is a karst cave located in the province of Cuneo in the Piedmont region of Italy. It is situated in the Maritime Alps, near the village of Frabosa Sottana. In the Italian karst panorama Bossea cave represents a key spot, not only because it is one of the largest tourist caves in Italy with a length of approximately 2.5 km and a depth of 200 m, but also because it hosts one of the most complete and active laboratories at the European level. The cave is characterized by a variety of unique features, including stalactites, stalagmites, underground lakes, and streams.

The cave has been open to the public since the 1960s and attracts thousands of visitors each year. It is managed by the Regional Natural Park of the Maritime Alps and is recognized as a Site of Community Importance (SIC) by the European Union due to its ecological and geological importance.

The objective of this analysis is to determine the dynamics of heat exchange between air, water and rock in the Bossea cave, characterizing the subjects involved in the exchange

and to assess the relationship the cave has with the external environment. The aim of this work is to provide an overview of the available data and perform a preliminary analysis, which will serve as a solid groundwork for the subsequent research.

This purpose was achieved by mean of the temperature data of air, water and rock, compared with the pressure and carbon dioxide levels in the cave thanks to a dense network of probes both inside and outside the cave. The data analysed comes from 40 thermometers (air, water and rock temperature) 36 of which are calibrated by the National Institute for Research and Metrology, 3 anemometers (one cup and two ultrasonic) and 4 carbon dioxide meters. The sensors are located in six main stations: Exterior, Entrance and Electrical Panel, Porfiroidi, Milano, Sacrestia and Fondo.

The data set analyzed covers the period 26/06/2021-06/09/2022. Nonetheless, the instrumentation has experienced malfunctions, resulting in missing data.

Initially, research will cover the dynamics of the air flow within the cave by analyzing mainly the air temperatures and comparing the evidence obtained from the different stations. Observing a strong seasonal trend for the data from the more superficial sensors, the data sets from each station will divided into two time periods in order to verify the external seasonal influence on the cave temperatures. To obtain an overall view of the temperatures, which is difficult due to the large amount of data, the box plot will be used.

Being Bossea is a tourist cave (17471 visitors in 2022) it is affected by the heat emitted by people entering it (Pulido-Bosch et al., 1997; Šebela et al., 2019; Šebela & Pipan, 2015; Šebela & Turk, 2011, 2014). In order to distinguish and process separately the long-term effects on temperatures from the short-term ones, the Fourier transform and moving average with three different moving window lengths will be applied to three sensors chosen as examples. Being CO_2 levels closely related to human respiration, they will be also compared to the number of daily entrances into the cave

Carbon dioxide in caves can have several sources (Kukuljan et al., 2021): the degassing of water from the main collector or secondary drips, the advection and diffusion from the soil, decomposition of organic matter, geogenic production and finally anthropogenic

respiration. To differentiate between natural and human-caused influences on CO2 levels, the levels recorded from 01/01/2020 to 01/05/2020 will be compared with those from the same period in 2021. It should be noted that during the mentioned months of 2020, tourist activities were absent due to the COVID-19 closures aimed at preventing infection.

The study of cave airflow mechanisms, cave temperatures, CO_2, and pressure levels is significant for several reasons. Firstly, caves are unique ecosystems that can be adversely affected by changes in airflow dynamics, temperature, CO_2 and pressure levels. Understanding these factors can help identify potential environmental threats and mitigate their impact on the cave ecosystem. Additionally, Caves can play a role in carbon sequestration, as CO_2 can dissolve in groundwater and precipitate as carbonate minerals in the cave environment. Understanding the factors that influence CO_2 levels in caves can inform our understanding of global carbon cycles and the potential for cave-based carbon sequestration.

2 The Karst environment

Limestone is a sedimentary rock whose main component is the minerals calcite and aragonite. This rock is composed mainly of calcium carbonate ($CaCO_3$), a chemical compound that is soluble in water and easily eroded. $CaCO_3$ can have two polymorphs: calcite, and aragonite. The phenomenon that acts by eroding limestone on a large scale through the action of precipitation water is called karstification.

The term karst takes its name from the geographical area of the “Carso”, Karst, located between Friuli Venezia Giulia and Slovenia. There, the karst phenomenon was studied for the first time, and from that moment onwards the term "karstification" referred to all phenomena that presented the characteristics found in the Trieste area.

Karstification indicates a set of chemical-physical phenomena through which rocks are both dissolved and eroded, resulting in the formation of particular morphologies on the surface and at depth. The best known of these processes concerns the dissolution of carbonate rocks by carbonic acid (H_2CO_3), which consists of four main reactions:

a. The reaction between carbon dioxide and water to form carbonic acid:

$$H_2O + CO_2 \rightleftarrows H_2CO_3$$

b. The dissolution of carbonic acid in water to form bicarbonate and hydrogen ions:

$$H_2CO_3 \rightleftarrows H^+ + HCO_3^-$$

c. The dissolution of bicarbonate ion in water to form carbonate and hydrogen ions:

$$HCO_3^- \rightleftarrows H^+ + CO_3^{2-}$$

d. The dissolution of calcium carbonate in the water forms calcium and carbonate:

$$CaCO_3 \rightleftarrows Ca^{2+} + CO_3^{2-}$$

The overall equilibrium is:

$$CaCO_3 + H_2O + CO_2 \rightleftarrows Ca^{2+} + 2HCO_3^{2+} \quad (1)$$

The above reactions are a function of factors such as water temperature, pressure, and CO_2 concentration, and can proceed from left to right and vice versa. In the first case, the carbonates are brought into solution: rainfall is enriched with CO_2 first in the atmosphere, then in the CO_2-rich soil due to organic decomposition, becoming a weak solution of carbonic acid (a), which, in turn, partially dissociates into bicarbonate (b) and carbonate (c) ions. Rainwater then percolates within the fractures of the carbonate mass, soluble in acid solutions (d), widening them and creating conduits of even considerable size.

On the other hand, when the reaction proceeds in the other direction, varying the pH of the solution can cause precipitation of $CaCO_3$, to form speleothems (literally 'cave deposits') such as the well-known stalactites, stalagmites, but also draperies (Figure 2.1), helictites (Figure 2.2), etc.

Figure 2.1 Drapery (source mercercaverns.net)

Figure 2.2 Helictites (source: https://www.nps.gov/)

However, not only carbonate but all types of rocks are subject to dissolution. The same karstic mechanism can occur in other rocks, which differ from limestone and evaporitic

rocks simply because the reactions have longer timescales: in the latters, the timescale is relatively short (always in the geological sense), while in the formers, dissolution takes much longer. As evaporitic rocks are mainly composed of sulphate rocks (gypsum and anhydrite) or halite (rock salt), they are extremely soluble even without the presence of acids (as well as carbonic acid in the reactions listed above) to be dissolved. Ice, on the other hand, deserves a separate consideration: although it is not a rock in the strict sense of the word, it can be affected by karst phenomena, as it has a high melting capacity that allows the formation of shafts, called moulins, meanders, and conduits similar to those existing in more classic karst environments. Limestones, some conglomerates, and all the intermediate phases existing between calcareous, dolomitic, and detrital rocks can also undergo karst processes, although the degree of karstification is lower about the decrease in the in carbonate ratio.

The speed at which the reaction (1) proceeds also depends on the type of carbonate in question, and appears to be slower for dolomites, i.e. double carbonates of calcium and magnesium ($CaMg(CO_3)_2$) and faster for limestones, composed of $CaCO_3$. In turn, $CaCO_3$ also has two polymorphs with two different solubility products: calcite and aragonite. Limestones and dolomites turn out to be the most important carbonate rocks for karst systems.

The typical karst conduits, which can also reach very large dimensions, are formed, as mentioned, by percolation of rainwater into the fractures, which, being a weak solution of carbonic acid, progressively dissolves the rock in contact with it, widening the fractures even in a short time. In addition, larger conduits normally have larger flows and enlarge

faster thanks to erosion. This creates a network of underground cavities explored by cavers.

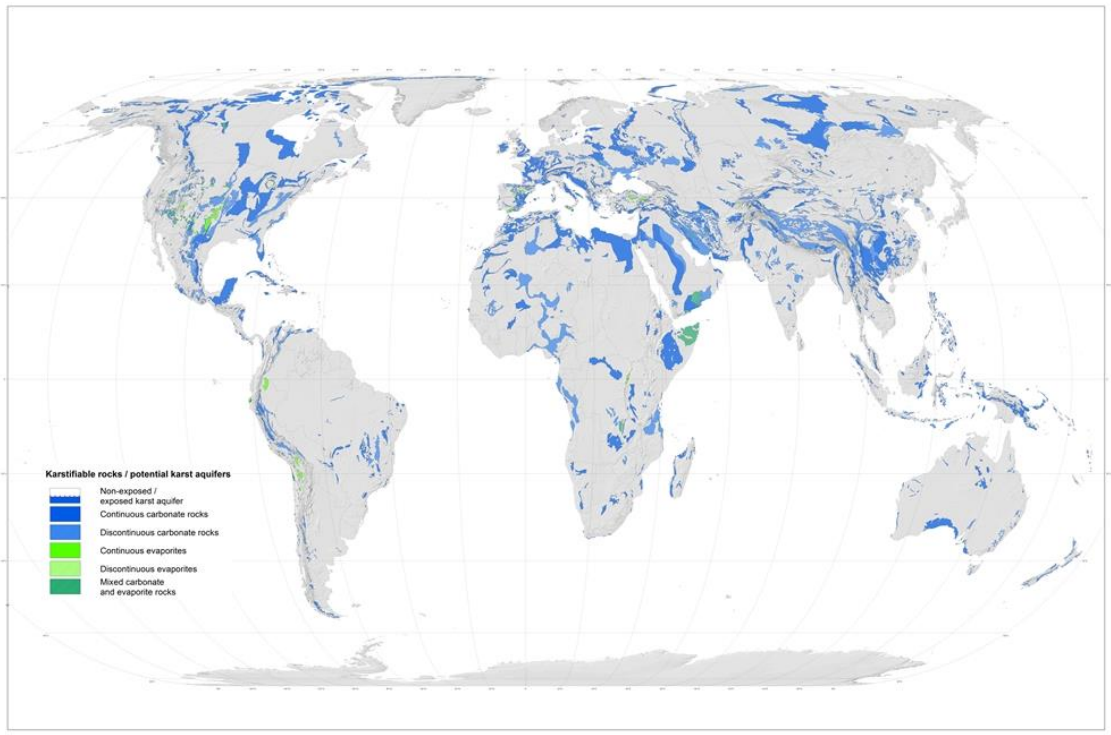

Figure 2.3 World distribution of karstifiable rocks (Chen et al., 2017)

Only 13% of the world's land surface is characterized by karst as shown in Figure 2.3 (Dai et al., 2017), yet its importance can be seen in in many fields, including several natural resources such as water for drinking and agricultural irrigation (Goldscheider et al., 2020). According to recent estimates, most of the planet's major springs have karst origin and are supplying 9.2% of global water demand (Stevanović, 2019), equal to 678 million people.

2.1 Karst landscape features

The elements that characterize karst morphologies are varied and mainly concern both the surface environment (epigean), with morphologies generally caused by water runoff on exposed rock surfaces or covered by detritus or soil, and the deep environment

(hypogean) in which morphologies are due to the deep circulation of infiltration waters. Infiltration-related forms, including sinkholes and cave entrances, while manifesting themselves on the surface, are linked to the subsurface karst and can therefore constitute a network of fractures and conduits, developing from surface to deep karst.

Areas subject to karstification may show common characteristics on the surface that make them easily recognizable. The most conspicuous of these is the absence of an organized hydrographic network and the almost complete infiltration of rainwater with consequent circulation at depth, through fractures and ponor. Some of these can be concealed by vegetation cover, soil, or sedimentary deposits of various kinds. A priori it is necessary to distinguish between covered, medium covered, or uncovered karst, or between high altitude karst, with an absorbent area located at an altitude of over 2000 m, medium altitude karst, with an absorbent area between 1000 and 2000 m, and low altitude karst, with an absorbent area of less than 1000 m altitude.

Figure 2.4 Karren fields near the Tsanfleuron glacier, Switzerland (source: Frédéric Maziere)

Karst environments located at high altitudes are generally characterized by sparse vegetation cover and almost absent soil. The superficial karst forms are flanked or modified by periglacial or glacial forms, which on the whole can commonly be described as glaciokarst forms such as glacial-karst basins, i.e. large plateaux located in mountainous environments, surrounded by steep slopes, in which glacial remodeling can be recognized. The most common karst forms, such as karren fields, dolines, closed valleys generally elongated according to the direction of the main tectonic discontinuities, and tectonic-karst depressions, are then flanked by debris accumulations, moraines, and mounded rocks.

Karren or lapiaz (Figure 2.4) are morphologies that can be observed on compact surfaces of bare karst rock and are formed through the exposure to rainwater erosion. Karren fields are characterized by a set of small furrows that are usually discontinuous, sinuous, and anastomosed.

Figure 2.5 Sinkholes in Maungati, New Zealand (source: Mytchall Bransgrove)

The low-altitude karst differs from the former for the presence of considerable vegetation cover and greater soil thickness. Here, although generally present, the forms described above are covered by vegetation. However, larger forms such as dolines, and other more

or less extensive structural depressions, sometimes abundantly covered by soil and vegetation cover, may be visible. Often barren, hilly reliefs may be separated by usually dry torrential incisions. The more depressed areas may host sinkholes, which are constantly evolving and dispose of water carried by small temporary streams. Dolines are among the most characteristic forms of karst areas and appear as funnel-shaped, rounded, or elongated depressions, varying in diameter and depth from a few to many meters, filled with debris and covered with grassy vegetation. They may originate from the collapse of underlying cavities or by dissolution. We talk about ponor if a watercourse flows into these depressions (Figure 2.5).

The mid-altitude karst, with intermediate characteristics between the two, just described, is characterized by the presence of a grassy cover, shrubs of different sizes, and an abundance of detrital deposits.

Caves are undoubtedly the most obvious morphological expressions of the karst landscape. They are defined as 'voids' of varying sizes that are normally interconnected to form underground karst systems (Eusebio et al., 2010).

3 Bossea Cave

Bossea cave is a show cave situated in the Ligurian Alps in the Municipality of Frabosa Soprana (CN), southern Piedmont, NW of Italy. The entrance of the cave opens on the western slope of the Corsaglia Valley at an altitude of 836 m above sea level. It represents the terminal part of a karst catchment that drains water from the Corsaglia and Maudagna valleys for a total of 6 km of longitudinal extension (Nannoni et al., 2020). It is located in the north-eastern sector of the carbonate area called Mondolé-Artesinera-Bossea (Figure 3.1) that includes other important karst systems such as those of Stalla Bourch (Abissi Bacardi and Artesinera) and the Mondolé (Balma Ghiacciata, Abisso Dolly, etc.).

Mean annual precipitation ranges between 1100 and 1200 mm.

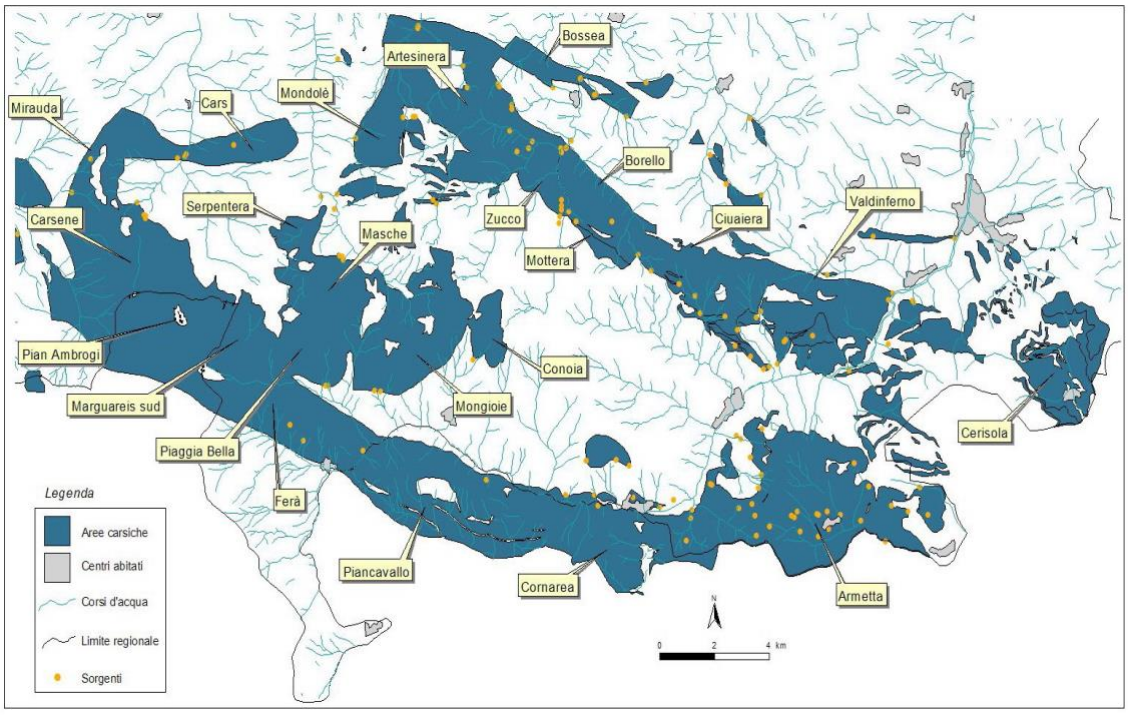

Figure 3.1 Mondolé-Artesinera-Bossea karstic area (Fonte: B. Vigna)

The length of the cave, as far as is known today, is about 3 km, with an altitude difference of almost 200 m. The cavity is very articulated and complex and presents a great variety of environments (Figure 3.3) such as:

- The canyon segment, located in the final area of the cave, is carved entirely into the karstic rock by the Mora River, the main collector. It begins at Lake Loser (a full-load siphon) and ends at Ernestina's waterfall. The entire section is only in contact with karstic rock and is nearly flat (1/1000 slope).
- The great halls segment is formed by a succession of large, steeply sloping rooms (Sala Garelli and Sala del Tempio) with evident collapse morphology. In this part of the cave the Mora river, which runs the whole length of the cave, flows through the contact between carbonates and underlying insoluble rocks;
- The entrance area consists of corridors of modest cross-sections, some of which are fossil/semi-fossil. One of these corridors constitutes the tourist entrance to the cave. The Mora River infiltrates inside these small corridors and springs then through bedding contacts along the Corsaglia River, as shown by the images taken by the thermal camera (Figure 3.2).

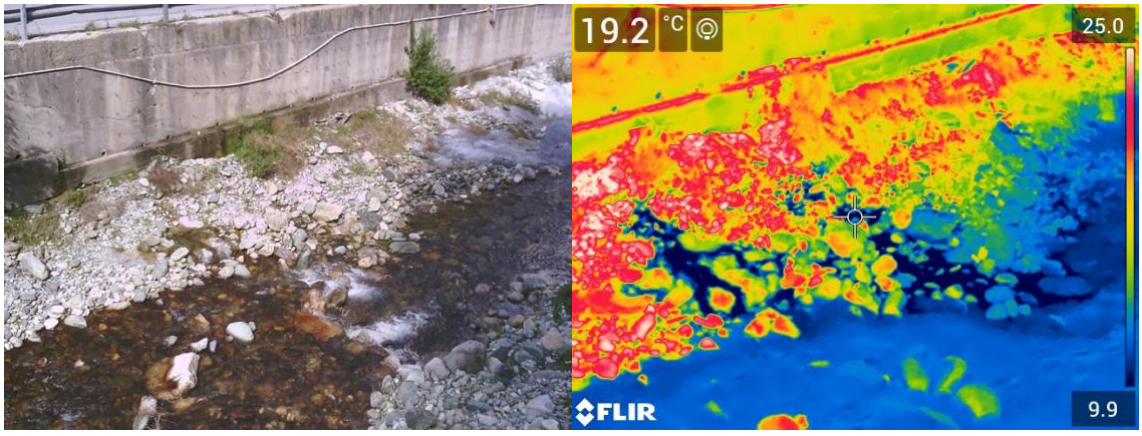

Figure 3.2 Original image (left) and thermal camera image (right)

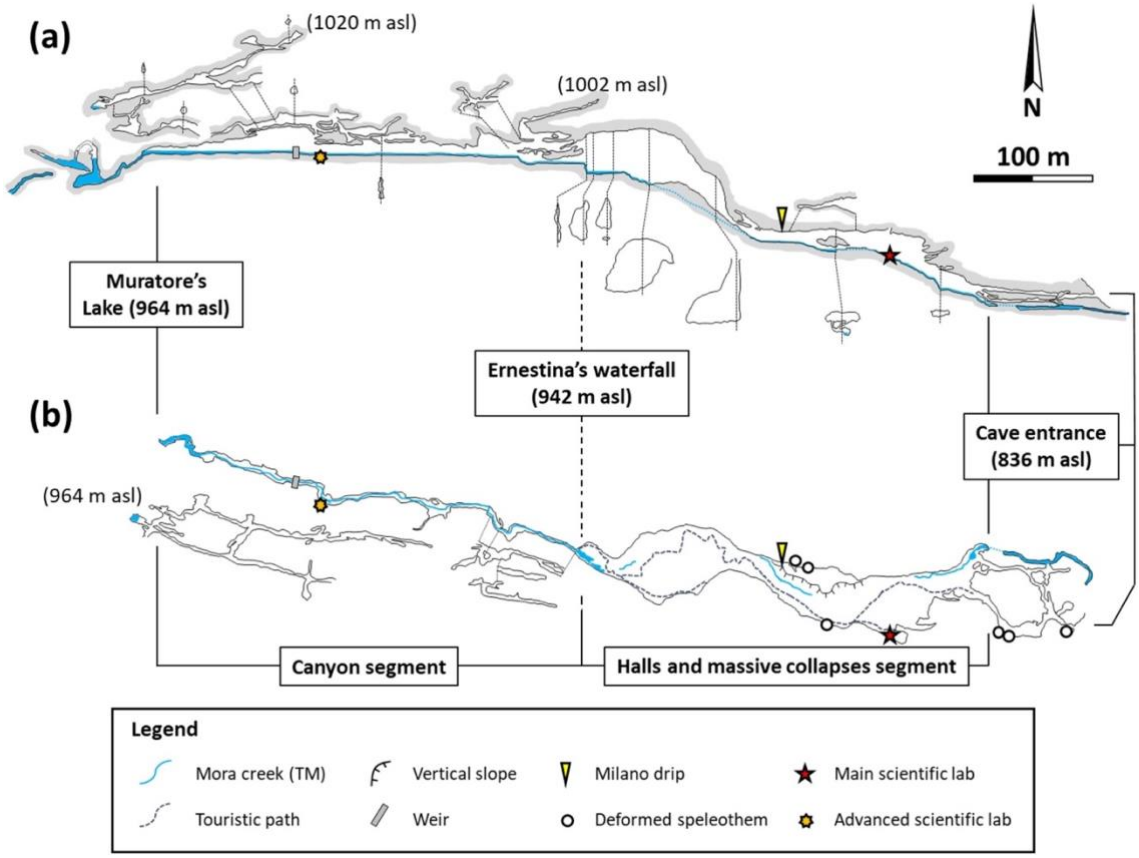

Figure 3.3 Vertical profile (a) and plan view of Bossea karst system (Antonellini et al., 2019)

3.1 Geological and geomorphological setting

The sector above Bossea Cave consists of a narrow band of limestone and dolomitic limestone referable to the Ligurian Briançonnais succession dated from the Middle Triassic to Cretaceous (Figure 3.4)

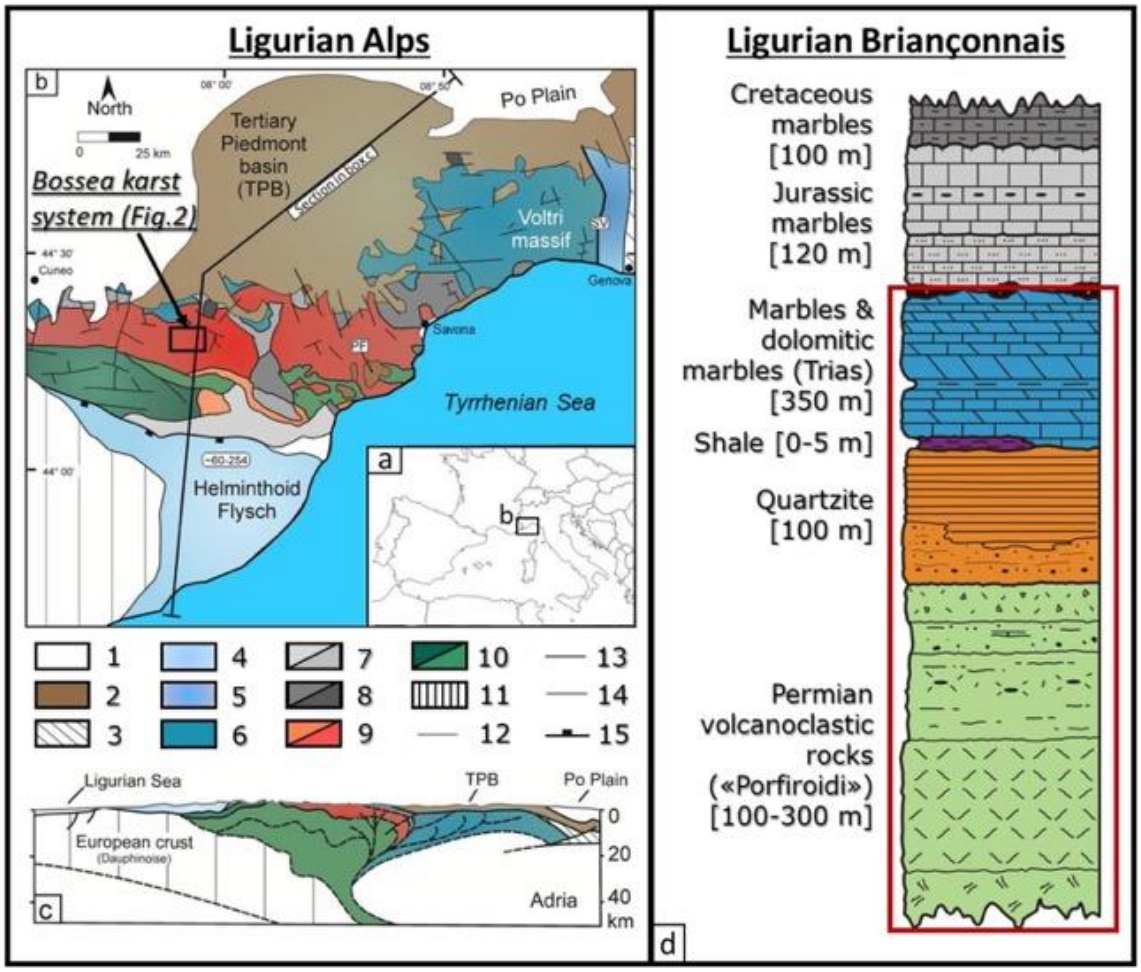

Figure 3.4 Map of the Ligurian Alps and location of the Bossea karst system (Antonellini et al., 2019) *(a) Index map. (b) Simplified regional geological map. Legend: 1. Plio-Quaternary deposits, 2. Oligo-Miocene deposits, 3. Apennine units; Piedmont-Ligurian units: 4. Helminthoid Flysch, 5. Sestri-Voltaggio zone, 6. Ophiolitic units; Pre-piedmont units: 7. Meso-Cenozoic cover, 8. Pre-Variscan basement; Briançonnais units: 9. Internal units, 10. External units; 11. Dauphinois units. Structural elements: 12. Unconformity, 13. Thrust, 14. Major late/post-orogenic faults (D4/D5), 15. Detachment fault. Late alpine faults: PF. Pietra Finale, SV: Sestri-Voltaggio. (c) Crustal cross-section across the Western Alps. The trace of the cross-section is in (b). (d) Stratigraphic section for the Ligurian Briançonnais, the red rectangle evidences the portion outcropping in the Bossea area.*

The carbonate structure is limited by the pre-Triassic rocks of the metamorphic basement, represented by practically waterproof and quite deformable porphyroids and by quartzites that are instead very fragile rocks. In some areas, the quartzites, subjected to considerable tension, have fractured to such an extent that, along the most important sliding planes, assume a condition comparable to the hydrogeological effects of permeable rock. An important deformation surface, oriented East with inclinations varying between 5° and 35°, between the metamorphic basement and the carbonate cover, characterizes the easternmost portion of the area and has heavily conditioned groundwater circulation. The metamorphic rocks near this surface are intensely fractured with areas also characterized by the presence of cataclastites and mylonites. The waters of the main collector, circulating through this contact, progressively dug a deep and wide gorge, mainly set in the metamorphic rocks, resulting in the collapse of the portions of the overlying carbonate mass and the formation of the gigantic halls that characterize the first part of Bossea Cave.

The carbonate rocks in the volume above the cavity show much less fracturing, with a decametric spacing: in correspondence with these discontinuities the water circulation is imposed and therefore constitutes the unsaturated zone of this portion of the karstic system. The thickness of this zone ranges between a few tens of meters in the sector near the cave entrance and over 150 meters at the end of the cavity (Figure 3.5).

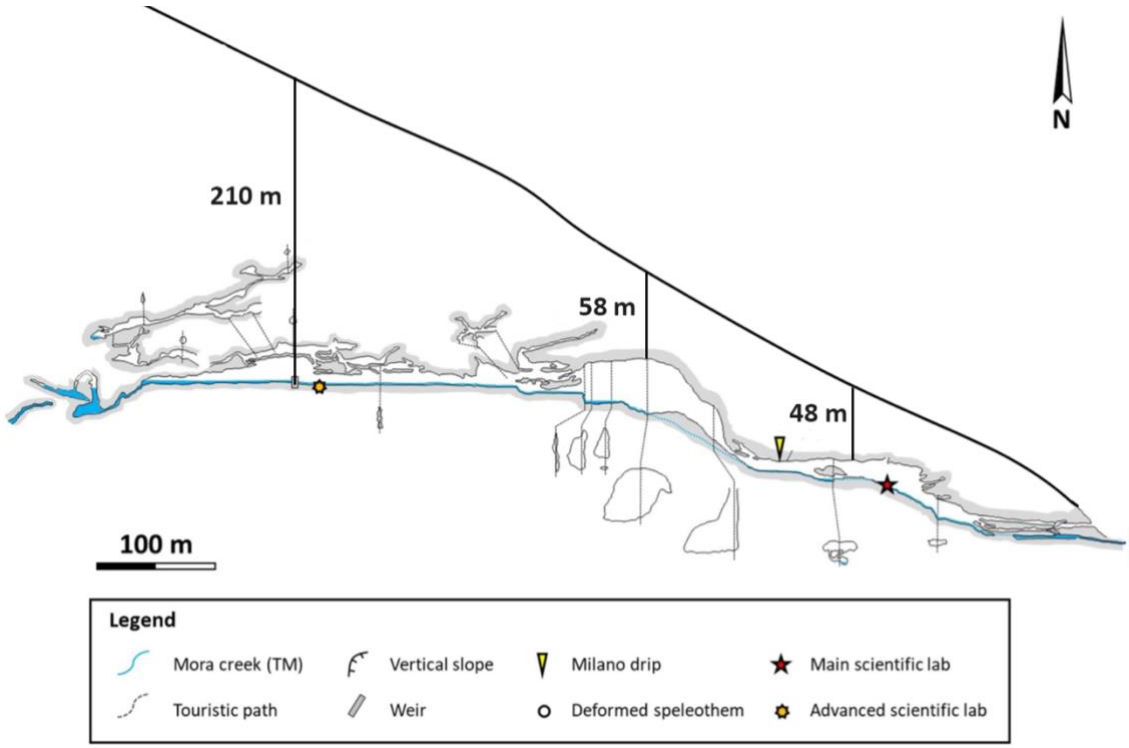

Figure 3.5 Thickness of the unsaturated zone above the cavity (Antonellini et al., 2019)

The dynamics of the formation of the karst ducts of the area foresees the infiltration of meteoric water inside the cracks of the rock, widening and descending by gravity since it encounters a waterproof and not easily assaulted by water obstacle, the porphyroids, above which the water have accumulated, saturating in the first place the cracks and then, at the lowest point of the outflow, finding a way of outflow to the surface.

3.2 Underground water circulation

Firstly, it is necessary to clarify how water circulation takes place in karstic environments. In soils, in the fractures generated by the tectonic phenomena, a water circulation that tends to widen the fractures and to connect them is imposed. The deepening of these fissures is mainly caused by the dissolution of the carbonates present in the calcarean rock, but also by its erosion. Two special situations can coexist in the same karst network: a circulation in well-drained ducts, in which the water circulates freely and where the

network organizes in a very similar way to that of surface hydrography; then a circulation in completely submerged areas in which a hydrostatic condition persists, in such a way as to generate almost circular pipes that connect each other with complex paths forming labyrinths or breaking up the very fractured areas that slowly empty of the rocky material, giving rise to gigantic salons.

The flow rate range of the karst sources is generally relevant compared to that of the sources in porous rocks, with very rapid flow changes; so, it may happen that a source switch in a few hours from a capacity of a few liters per second to that of a few thousand liters per second. The water that reaches the karst network normally comes from external precipitation, rain, snow, or condensation inside the cave (De Freitas & Schmekal, 2006), present mainly in conditions of particularly humid air circulation.

The Mora River arises from the sump situated at the end of the cave and explored in 1999 by the G.S.A.M. and CSARI (Bruxelles) for 250 meters long and up to a depth of 54 meters. The group could not continue due to a large accumulation of dangerously unstable clayey debris that partially blocked the duct. This accumulation was due to a large landslide falling upstream of the sump, caused by an exceptionally violent flood in 1996 (Zunino M, 2020).

After the sump, the Mora River proceeds along the upper part of the cave which is a high and narrow canyon with a low gradient (1 m/km), that ends at Ernestina Lake. After that, it runs through the “great halls” area (from 940 m s.l.m. to 826 m s.l.m.) mainly under the rockfalls that occurred in these big rooms and probably took place in the middle and lower Pleistocene, when the lifting of the entire carbonate sector determined the rejuvenation of both superficial and deep drainage networks (Vigna, 2020). During the Pliocene hot phases, the “full load” drainage system must have been developed, then partly deepened by the vadose circulation. In Bossea Cave, the deepening of the karst network has mainly affected the intensely fractured meta-vulcanites generating a gorge that reached a width of more than 50-70 m. Since the ceiling, consisting of fractured carbonate rocks, was in a condition of non-equilibrium, it collapsed giving rise to the large halls that nowadays characterize the tourist branch. In this sector, the dissolutive speleogenesis is secondary

and was important mainly in the inception stage (Antonellini et al., 2019). Finally, the river infiltrates a network of full-load conduits and springs later along the Corsaglia riverbed, as shown by the thermal camera (Figure 3.2), at 800 m s.l.m.

In a karst environment, three main types of circulation can normally be recognized that differ according to the hydrodynamic response to the incoming flows:

- Systems with high flow organization (Figure 3.6, a.): in this situation the aquifer has usually a very high permeability due to the presence of large karst ducts that quickly drain incoming flows. For this reason, sudden growth in outcoming flow is coupled with infiltrating events such as heavy rainfalls, snow melting, and river leakages. The rise in the flow rate is normally followed by a drop in water temperature and mineralization, all since the outflowing water is mainly the same that infiltrated during the input event. This kind of response is usually called “replacement”.

  In these systems, it is difficult to recognize a properly saturated area due to the high organization of the karst system, in which the circulation occurs through preferential drainage paths.
- Systems with moderate flow organization (Figure 3.6, b.): usually have high permeability, and the water circulation takes place partly in the fractures of the rock mass and partly in the ducts which are interrelated. These systems normally react by mobilizing, thanks to the hydraulic pressure provided by the water supplies, the water already present inside the aquifer that was in equilibrium with the rock mass and by replacing it with new water, at least for the first part of the event. This results in a sudden increase in mineralization and temperature values at the source (that can sometimes be interpreted as the temperature of the rocks). This kind of response is usually called “piston”.
- Systems with no flow organization (Figure 3.6, c.) have usually a low permeability due to the fracture network and have a well-developed saturation area. In this case, the pressure wave given by the infiltrative events fails to propagate inside the aquifer. The waters move very slowly indeed, so mild

increases in flow over time and rather constant high values of temperature and mineralization are observed at the source.

The three cases mentioned above are the result of three different geomorphological situations, two of which are visible and distinguishable in Bossea.

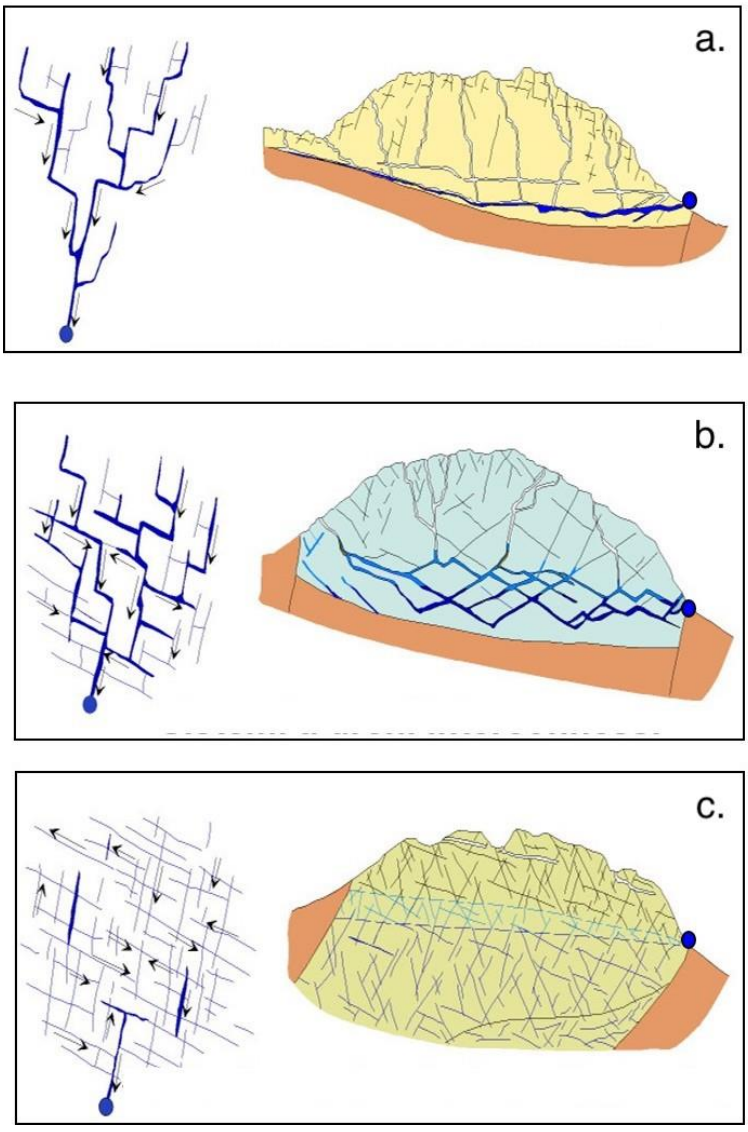

Figure 3.6 Three aquifer models: a System with dominant drainage. b System with interconnected drainage. c System with dispersive circulation. In yellow carbonatic aquifer, in brown impermeable rocks (Vigna 2001)

Figure 3.7 Microkarst in the unsaturated area above Bossea cave (photo from 24/09/2022 field survey)

The Mora stream is the result of water circulation in the network created by proper karstification. Medium/large conduits are feeding it, as shown by the analysis of data from the weir built upstream of Lake Ernestina. Secondary flows, on the other hand, are the result of the microkarst formed at Bossea, i.e. water circulation in small fractures that, reacting to the pressure wave caused by infiltrative contributions, mobilizes the water present in them and replace it with newly infiltrated water. The latter circulates at such a small speed that it in turn returns to equilibrium with the rock mass. The effects of microkarst are easily visible near the cave entrance as shown in Figure 3.7.

3.2.1 Mora River

The Mora stream runs through the entire cave, largely flowing beneath the deposits deriving from the collapse of the main halls. It is monitored by a weir equipped with a multi-parameter probe (levels, electrical conductivity, and temperature) installed in the stilling basin upstream of the weir. Data are acquired every 15 minutes. From the level data, the flow rate is derived thanks to the equation of the thick-walled weir:

$$Q = \mu * b * L * \sqrt{2g * L}$$

Where b is the width of the rectangular threshold equal to 1.2 m and μ is the outflow coefficient, which is constant and, for a broad-walled weir, equal to 0.385.

The precise location of the weir is shown in Figure 3.3.

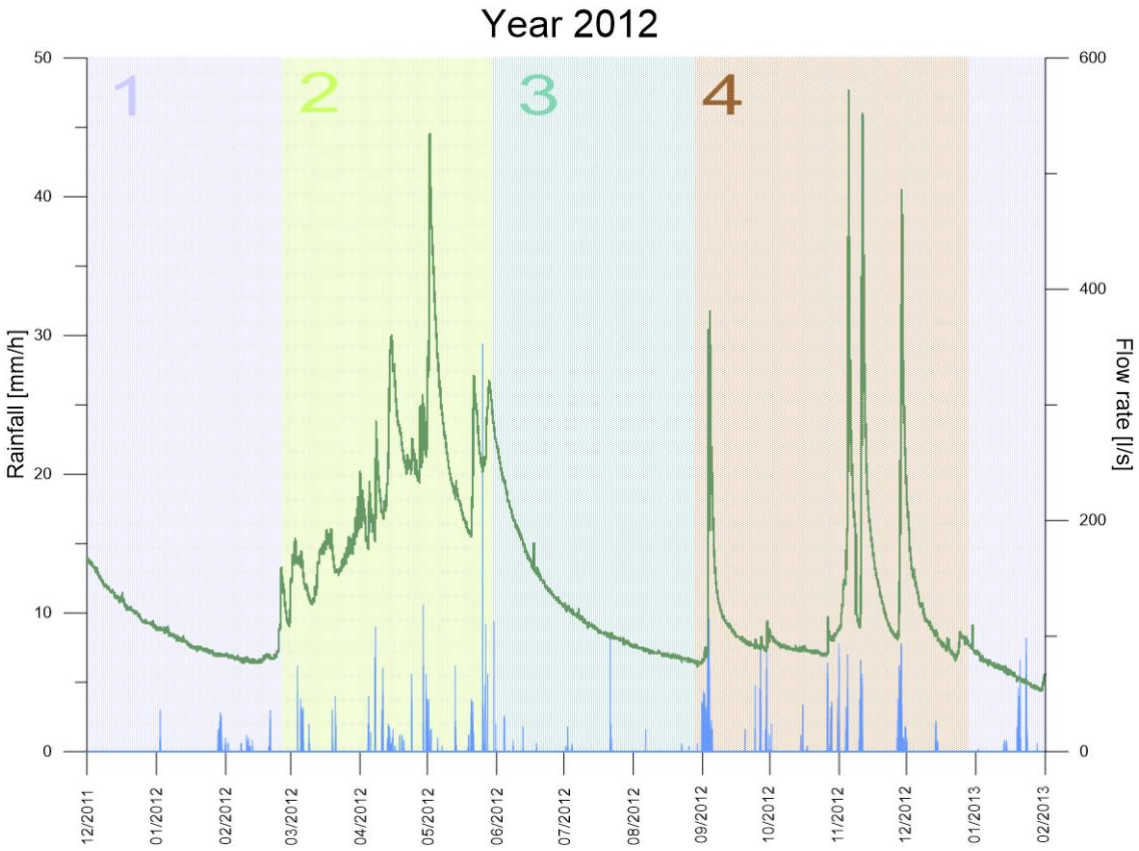

Figure 3.8 the Year 2012, Mora River flow rate and Borello station precipitations

The Mora River (Figure 3.8) has winter dry periods because, since much of the catchment area is located above 1,500 m asl, it is affected by sub-zero temperatures for most of the season, which results in solid precipitation (snow) being stored on the surface until the snowmelt period (Figure 3.8, 1). As the surface temperature increases, a flood related to nival melting occurs, which is easily recognizable as it shows a substantial increase in flow in the April/May period (Figure 3.8, 2). In addition, the nival melt flood is recognizable since it exhibits a steady increase in flow rates, as emphasized by the area subtended by the graph in Figure 3.8. Peak flows during this period may be due to particularly warm days that accelerate snowmelt flow.

During the summer, precipitation events consist mainly of thunderstorms, which can have significant intensity but short or very short duration. This type of event does not

contribute to the flow rate since most of the water fails to infiltrate and is lost either through surface runoff or evapotranspiration, which plays an important role in this season. (Figure 3.8, 3).

This period is followed by autumn rainfall, which, unlike summer rainfall, manages to infiltrate due to the prolonged duration of the events; Water, in this case, has time to infiltrate and contribute to the flow rate (Figure 3.8, 4). Peak flows due to these events reach maximum values of 1000-1200 l/s, but can also exceed 1800 l/s during exceptional events. It was precisely during one of these exceptional events (October 1996) that the Mora showed a flow rate (estimated, as the volumes were so large that any instrumentation installed at the time was inefficient) of 6000 l/s. Since the 1996 event, the waters of the collector are no longer as clear as before, and, during flooding periods, in which the higher water velocity mobilizes the fine particles deposited in the final siphon, there are very important turbidity peaks (Vigna, 2020). The increase in turbidity is due to the reduction of the surface layer consisting of medium-large clasts, which acted as a filter before the infiltration into the karst system, due to a large number of debris flows that occurred on the surface following the major precipitation event. The debris flows removed the aforementioned filter, increasing the infiltration rate and thus decreasing the sedimentation rate.

To understand the overall functioning of the water system, it is also interesting to compare the flow rate, electrical conductivity, and temperature of the main collector. In terms of available data used for the analysis, the years 2020 and 2021 were considered. The missing periods are mainly due to instrumentation malfunctions. The most significant missing periods are:

- from 17/10/2020 to 31/12/2020 for temperature and electrical conductivity data;
- from 27/08/2021 to 13/10/2021 for flow rate, temperature, and electrical conductivity.

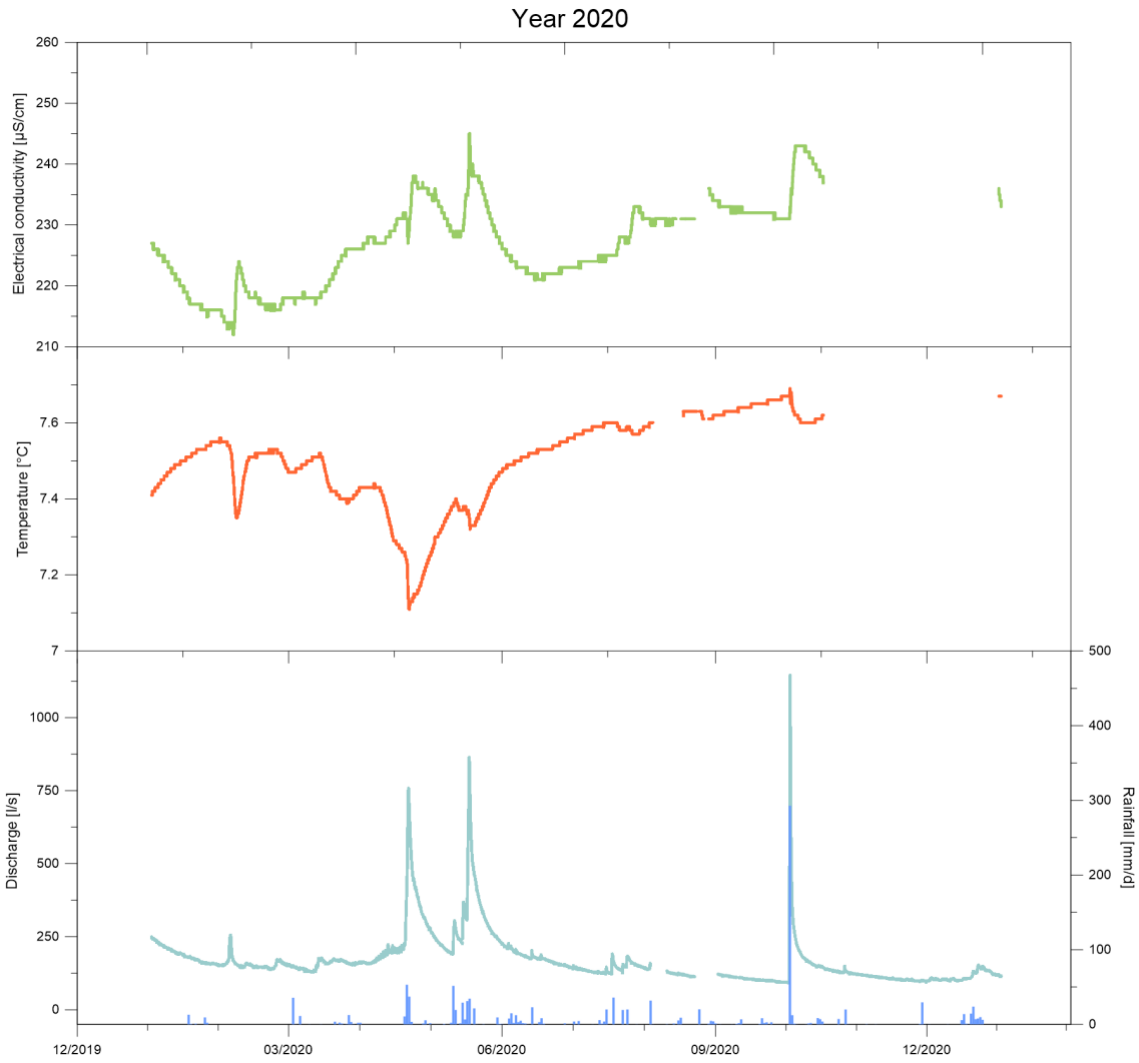

Figure 3.9The year 2020, Main collector

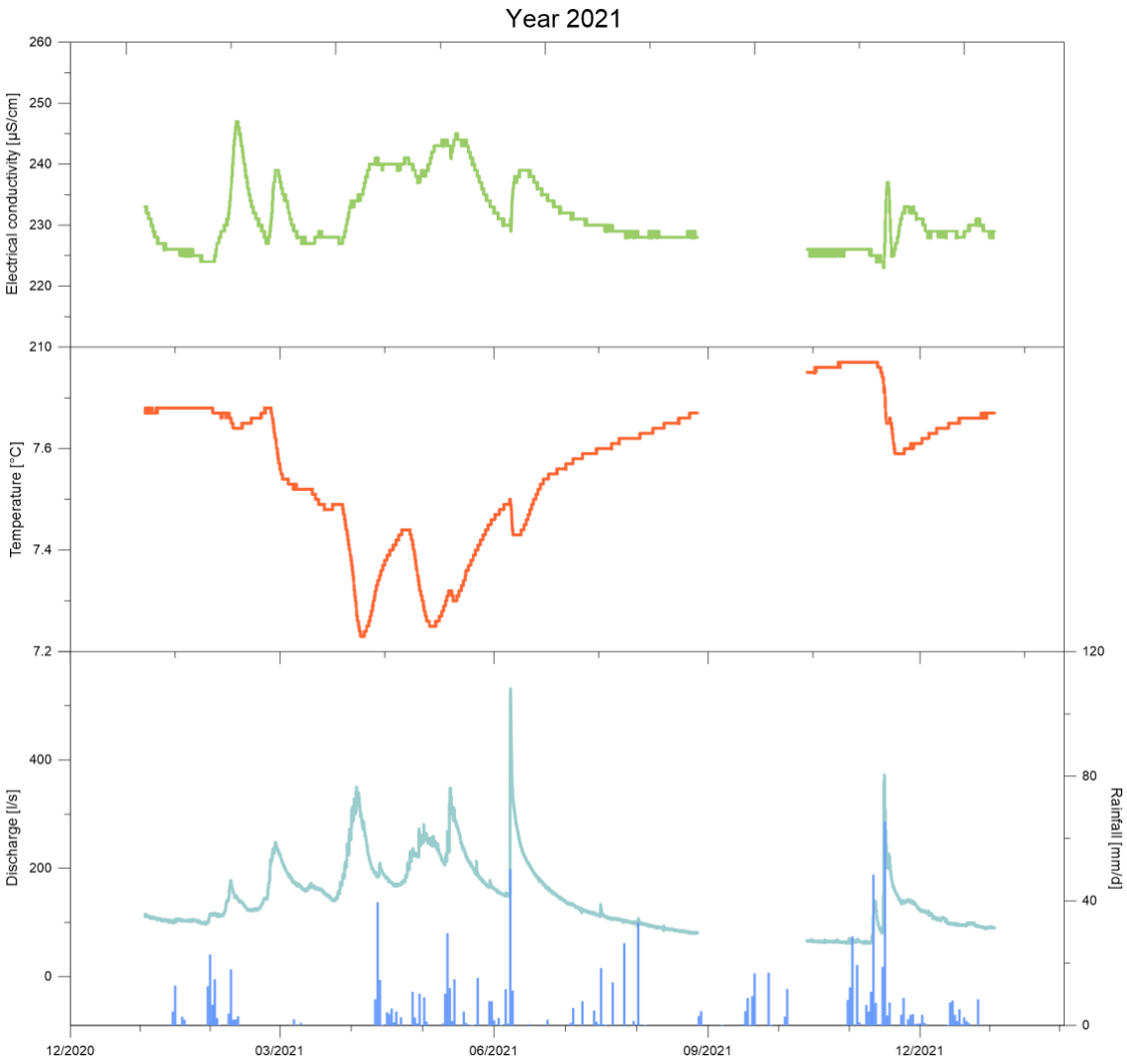

Figure 3.10 The year 2021, Main collector

Rainfall data shown in Figure 3.9 and Figure 3.10 are taken from the Borello station, which is located a few hundred meters from the Bossea entrance.

Firstly, it is considered that mineralization is generally very low (an average of 226 µS/cm for 2020 and 231 µS/cm for 2021), due to the contribution of water from metavulcanites, quartzites, and surface debris. In fact, in karstic environments such as the one studied, higher CE values would be expected, mainly due to the dissolution of carbonates. The passage into less soluble rocks such as the aforementioned quartzites and metavulcanites, on the other hand, causes very low mineralization.

The temperature fluctuates very little (between 7.2 and 7.8 °C) with lows during floods due to snowmelt, where the water infiltrates at a temperature of 0°C-1°C. Temperature decreases during flow increases.

3.2.2 Seepages

Concerning the seepages, 8 main seepage points are monitored by probes for water temperature, electrical conductivity, and water level every 15-60 minutes. These points are Polla delle Anatre, Polla Orso, Polletta, Milano, Onda, Balena, Torre, Laghi Pensili. Small triangular or rectangular weirs were realized at these points. For two other drip points, the flow rate is measured through a pluviograph. Most of the secondary seepages are usually dry or with a low flow rate, except for Polla delle Anatre. Each one of these seepages is the result of circulation in the pattern of fractures, mostly due to discontinuities with very small or no karst.

Polla delle Anatre, the main seepage in terms of discharge, is characterized by a very constant flow rate over time, around 0.5 l/s, with temporary increases in flow related to pressure waves generated by infiltration processes that remobilize more mineralized and hotter waters that reside in the less permeable sectors of the rock mass (micro-cracks and layer joints). The seepage has clear piston flow behaviour (Figure 3.11 and Figure 3.12) since, as the flow rate increases, there are synchronous increases in conductivity and temperature. Water that has been remobilized by pressure waves can be imagined as being in equilibrium with the rock mass in which it lies for a long time. The associated temperature peaks can therefore be interpreted as the average temperature within the rock mass. Apart from these moderate increases in temperature and flow rate, Polla delle Anatre has a very constant water temperature (9.95 °C) and flow rate (0.5 l/s) as seen in Figure 3.11 and Figure 3.12, which is influenced only by heavy rainfall events.

Polla delle Anatre is monitored by the construction of a triangular weir and the installation of a multi-parameter probe (level, temperature, and electrical conductivity) in the stilling basin. The flow rate is derived using the calibration curve shown below.

$$Q = 41.392 * (H - 0.022)^{1.4273144}$$

The curve is normally realized by carrying out some manual measurement to correlate the measured level with the flow rate of the water supply. These are normally taken in different hydrological periods to make the curve as representative as possible. The oscillation of the discharge in Figure 3.11 and Figure 3.12 is due to problems with the measuring instrument.

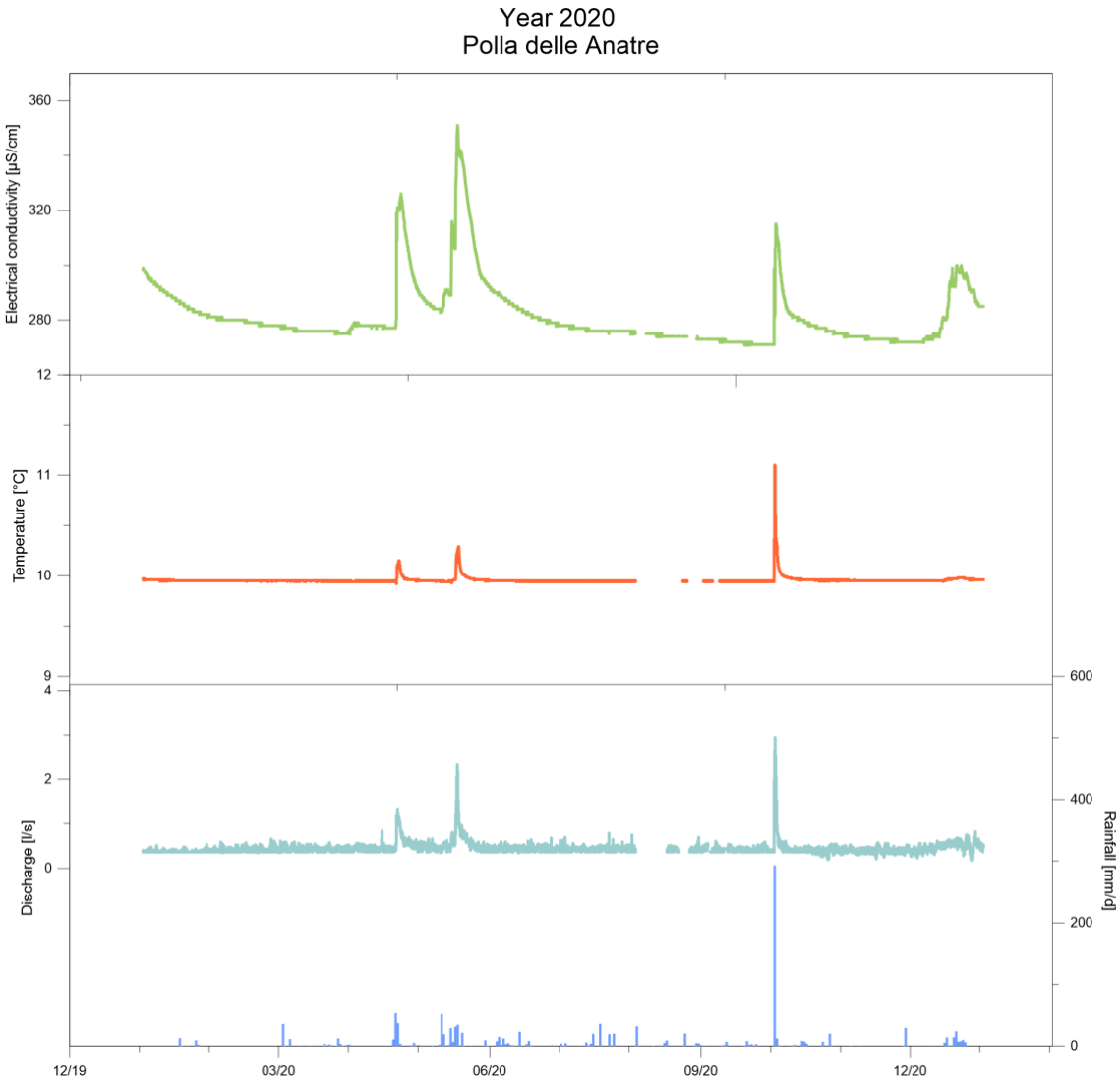

Figure 3.11 Flow rate, temperature, and electrical conductivity values in Polla delle Anatre related to precipitation rate (year 2020)

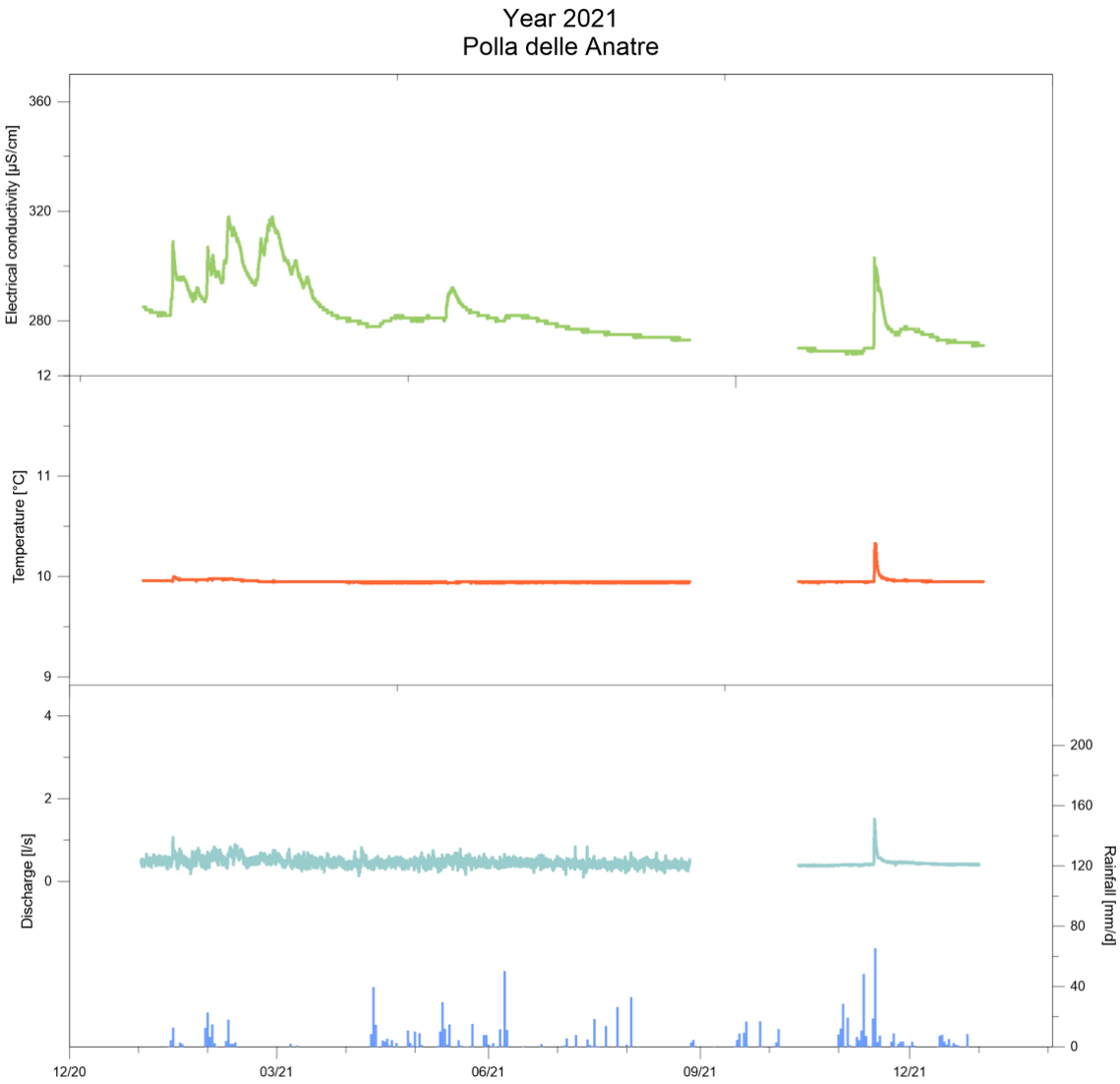

Figure 3.12 Flow rate, temperature, and electrical conductivity values in Polla delle Anatre related to precipitation rate (year 2021)

Other secondary venues, such as Polletta, Milano, and Onda have very similar responses. Consisting of drips for most of the year, they reach flow rates of less than 1 l/s only during major infiltration events. In that case, the flow rate increases rapidly and takes a few weeks to return to its original state (Nannoni, 2019). Conductivity values for these secondary flows tend to be very high (400 µS/cm for Polletta and above 500 µS/cm in Milano), but they undergo a temporary and sudden decrease (Figure 3.13 and Figure 3.14) coinciding with the arrival of the pressure wave due to new inputs. This could be linked

to the mobilization of water from portions that are not usually drained by the streams in question, such as the more impermeable rocks mentioned above (Vigna, 2020).

The water temperature of November 2021 and April/May 2022 flood events are compared to the one of the days before it (Figure 3.13 and Figure 3.14). Related data are shown in Table 3.1 and Table 3.2.

The only one to show a negative downturn is the main collector, which, as noted above, is fed by the drainage of the main fractures and ducts of the karst network. The secondary drips, on the other hand, show increases due to the remobilization of the water present in the micro-karst reticulum, which is therefore in equilibrium with the temperature of the rock mass.

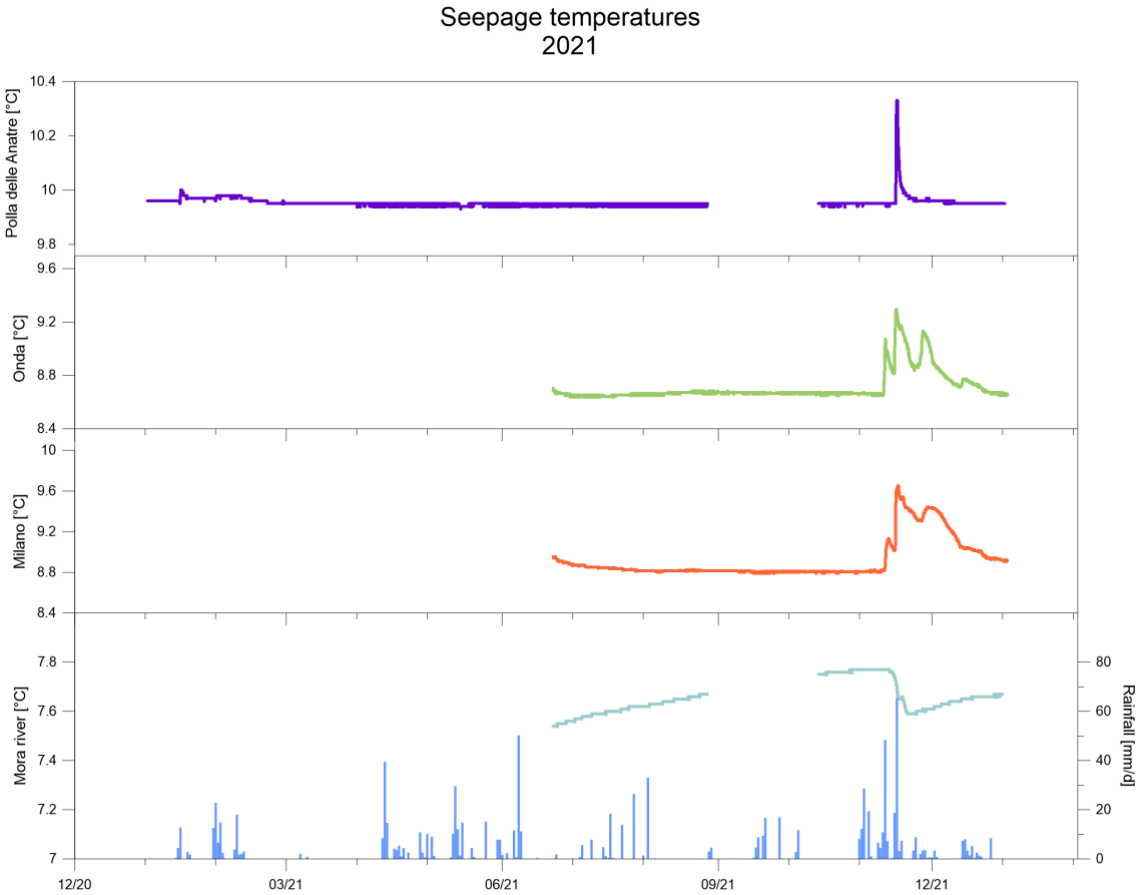

Figure 3.13 Comparison between water temperatures of secondary drips and main collector (year 2021)

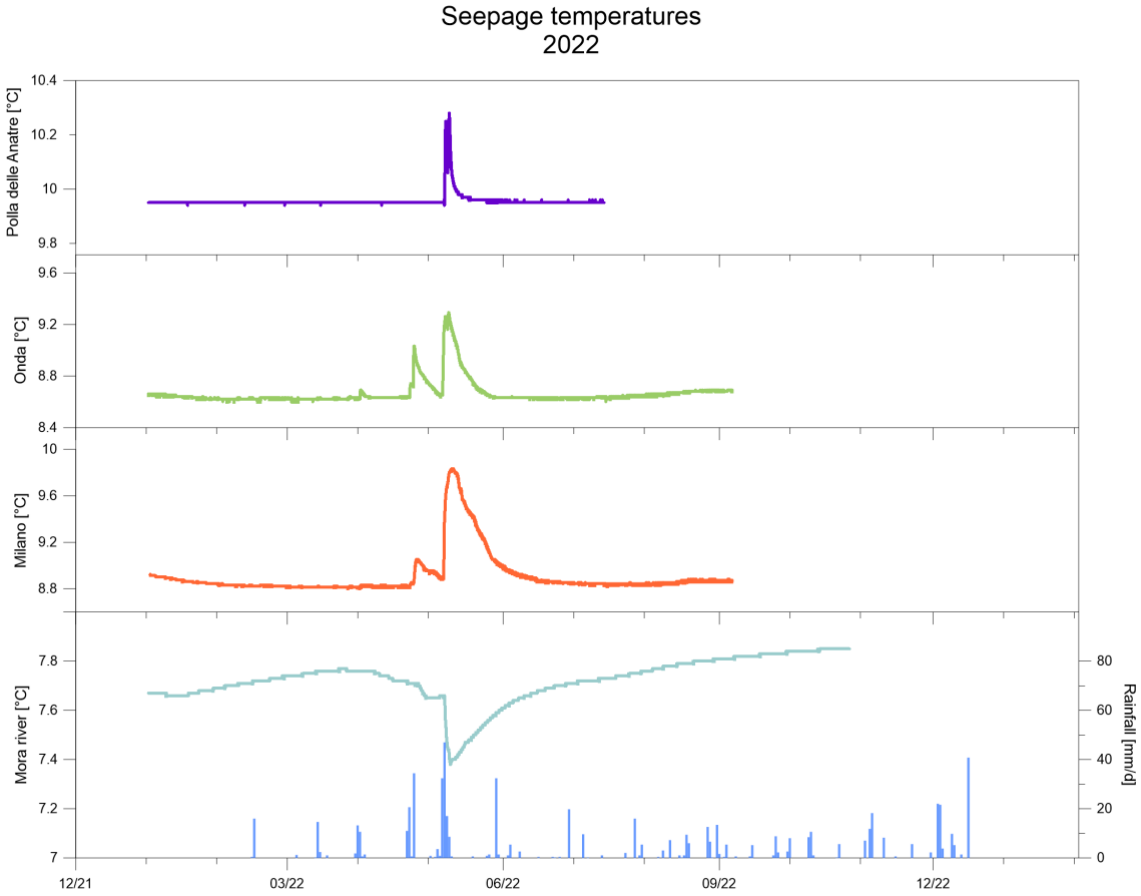

Figure 3.14 Comparison between water temperatures of secondary drips and main collector (year 2022)

Table 3.1 November 2021 precipitation event

	Mean value	Max	Min	Delta
Stillicidio Milano (°C)	8.81	9.65	-	0.85
Onda (°C)	8.66	9.29	-	0.63
Anatre (°C)	9.95	10.33	-	0.38
Main collector (°C)	7.76	-	7.59	-0.17
Main collector flow rate (m/s)	64.83	372.18	-	307.35

Table 3.2 May 2022 precipitation event

	Mean value	Max	Min	Delta
Stillicidio Milano (°C)	8.82	9.83	-	1.01
Onda (°C)	8.63	9.29	-	0.66

Anatre (°C)	9.95	10.28	-	0.33
Main collector (°C)	7.75	-	7.38	-0.37
Main collector flow rate (m/s)	71.70	684.80	-	613.10

The mean value in Table 3.1 and Table 3.2 is calculated during the 10 days before the event.

Other water drips such as Polla Orso and Balena have the same kind of response, typical of piston systems. They are normally dry during the year, especially following recent years characterized by few precipitation events.

3.3 Catchment area and unsaturated zone

The catchment area represents the external surface within which the infiltrative inputs feed the source under investigation. It may coincide with the basin boundary, depending on the presence or absence of underground or surface watersheds. The latter are often easily recognizable on sight while the recognition of the former, on the other hand, is more complex, as they may consist of anticlinal structures or stratigraphies of particular conformation.

The catchment area of the Bossea system is characterized by a Triassic-Cretaceous carbonate sequence varying in width from 600 to 1200 m laterally confined by quartzites and meta-vulcanites that constitute the impermeable rock complex (Figure 3.15)

Infiltrative inputs (rain, snowmelt, sub-surface losses) feeding a spring can be divided into two categories: primary and secondary. The former infiltrates underground as it reaches the surface, without undergoing runoff, while the latter reaches the ground in an impermeable area and, after the runoff, infiltrates into the subsoil contributing to the recharge of the aquifer. Bossea's karst system is an example of a mix between the two types: in fact, it receives primary infiltration, the infiltrative contributions that infiltrate directly into the carbonate mass, and secondary infiltration, due to runoff from low-permeable rocks (quartzites and meta-vulcanites) or detrital masses above them. Almost a third of the water that runs through the Bossea underground stream comes from non-

karstic areas, and an important contribution is given by the quartzites, which works as a giant drainage system often interposed at the contact between the substrate and limestone outcrops. Most of the inputs, therefore, come from sinkholes present on Rio Bertino and Rio Roccia Bianca in the contact area between carbonate rocks and poorly permeable rocks. Only during flood periods some of the water of these two streams fails to infiltrate into the sinkholes and flows downstream.

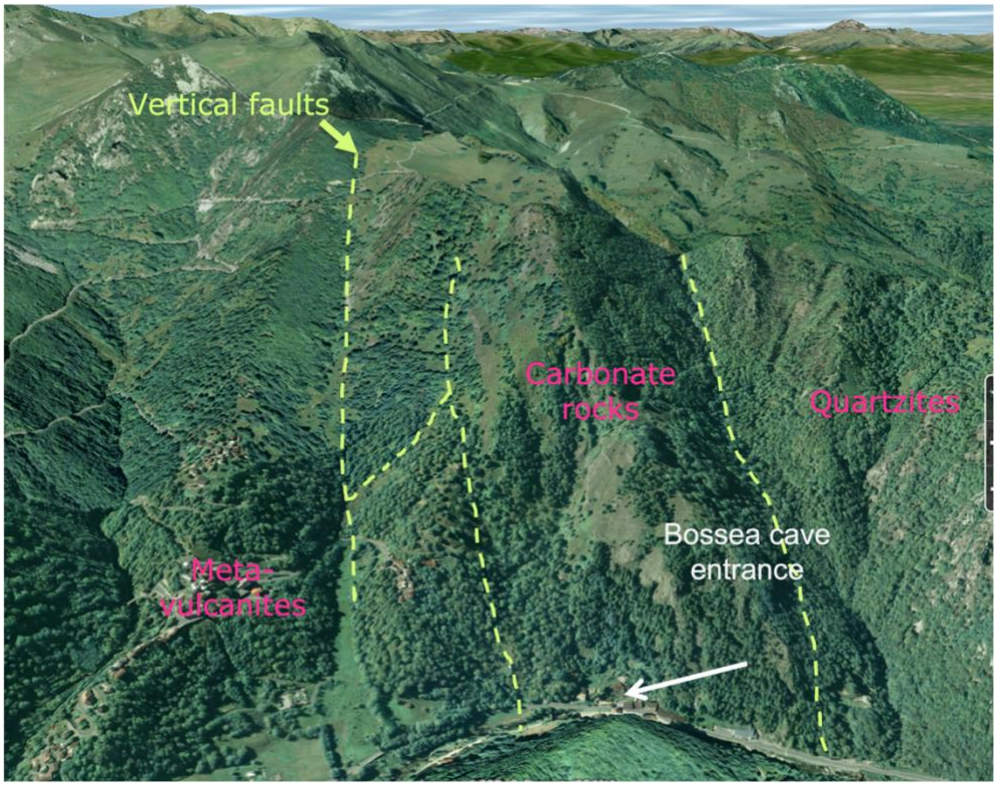

Figure 3.15 Carbonate belt laterally confined by poorly permeable rocks (quartzites and meta-vulcanites) through vertical faults (Vigna, 2020)

To prove the connection between these sinkholes and the Bossea karst system, tracer tests were carried out. This type of test involves introducing a tracer into the groundwater flow network and monitoring it at the supposed arrival points. The tracer must have characteristics to perform the test correctly, such as:

- a very high solubility in water to be able to approximate the introduction of the tracer as instantaneous. The tracer is normally in a solid state, then mixed with water and injected;
- be chemically neutral (conservative), i.e. not undergo adsorption phenomena or chemical reactions that would decrease its concentration;
- be physically neutral, i.e. not separate by gravity or become trapped in the pores of the lithological matrix;
- not change the dynamic characteristics of water (viscosity or density);
- possess a very low limit of detection to be easily detected at source, especially in the case of large distances between input and source;
- be easily analyzable and cheap;
- nontoxic;

Between the various types of tracers on the market, Tinopal and Fluorescein, fluorescent tracers, were chosen for the tests. The former has the advantage of being practically invisible at low concentrations (at high concentrations it has a bluish color), while the latter has a highly visible yellow fluorescent color which can sometimes create unnecessary alarm among the civilian population (Figure 3.16). Tinopal, however, is very photosensitive and it is therefore preferable that it be injected at night to avoid an artificially attenuated concentration on arrival.

Figure 3.16 Tracing tests with fluoroscein (left) and Tinopal (right). (Source: Bartolomeo Vigna)

Tracer tests are particularly useful to verify the limits of a hydrogeological structure and to check the water connection between two known points. If an automatic acquirer can be installed, in addition to proving the actual connection between two points, it is also possible to obtain the tracer breakthrough curve, which can provide useful information regarding the organization of the drainage network of a hydrogeological system (Gattinoni & Scesi, 2018; Vigna, 2020). From the concentration and arrival times of the tracer, the type of aquifer under investigation can be assumed as:

- Drainage-dominant if the tracer return curve shows a peak with a very high concentration in a very short time. In this case, the dispersion of the tracer is very low and the water flow, running through large drainage channels, has a high velocity.
- Interconnected drainage system if, on the other hand, there will be a discrete dispersion of the tracer, with no high-water flow velocities. The breakthrough curve will therefore present attenuated or multiple peaks.
- Dispersive circulation. In this case, this type of test is not always useful since, even in the presence of an effective connection between the two locations, the breakthrough curve may be very delayed and diffuse.

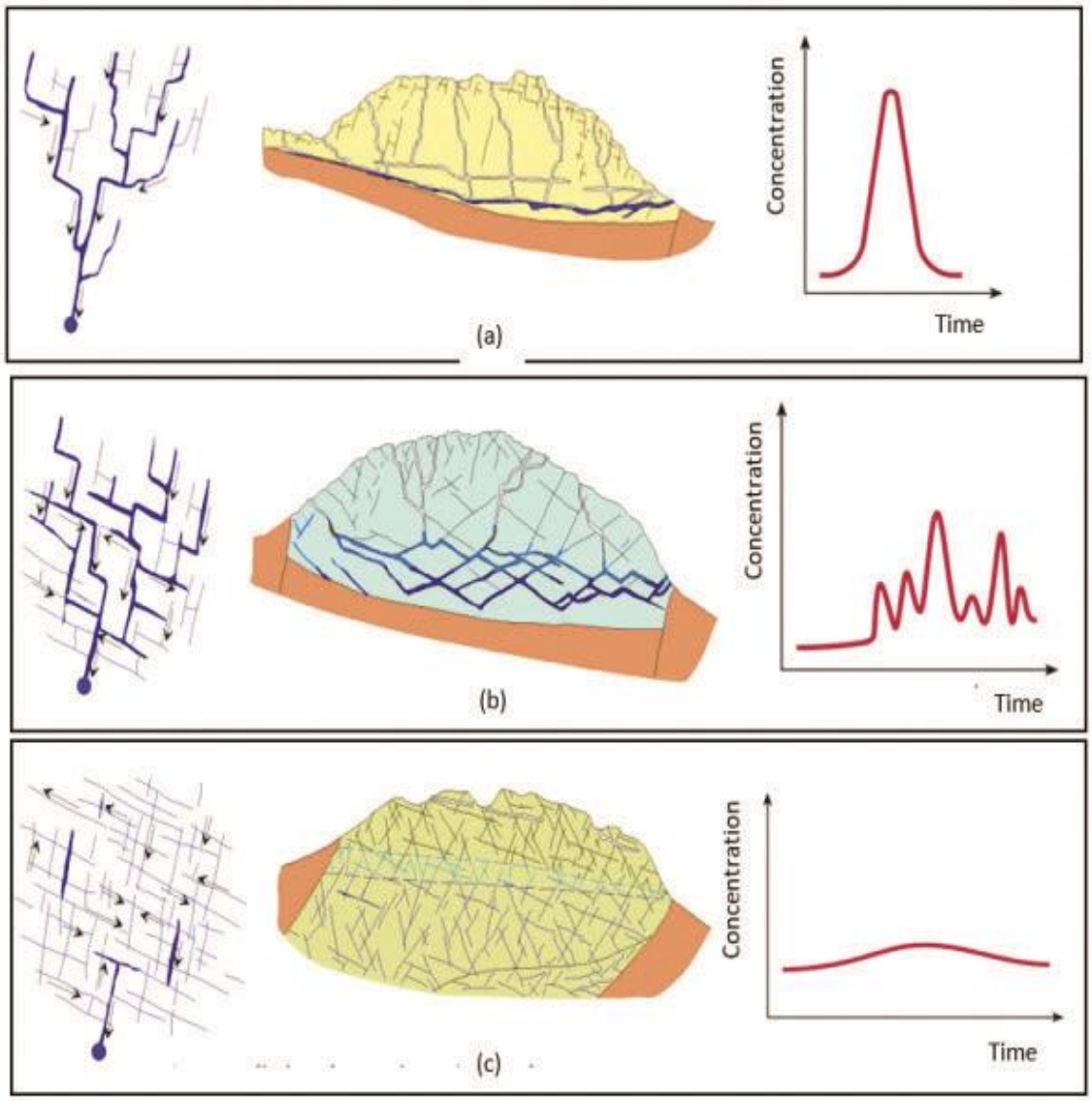

Figure 3.17 The three types of aquifer and their time-concentration curve during tracing tests (Gattinoni & Scesi, 2018)

Table 3.3 Tracer velocity under different conditions

Hydrological conditions	**Maximum velocity (m/day)**
Flood	2460
Normal	1300
Dry	644

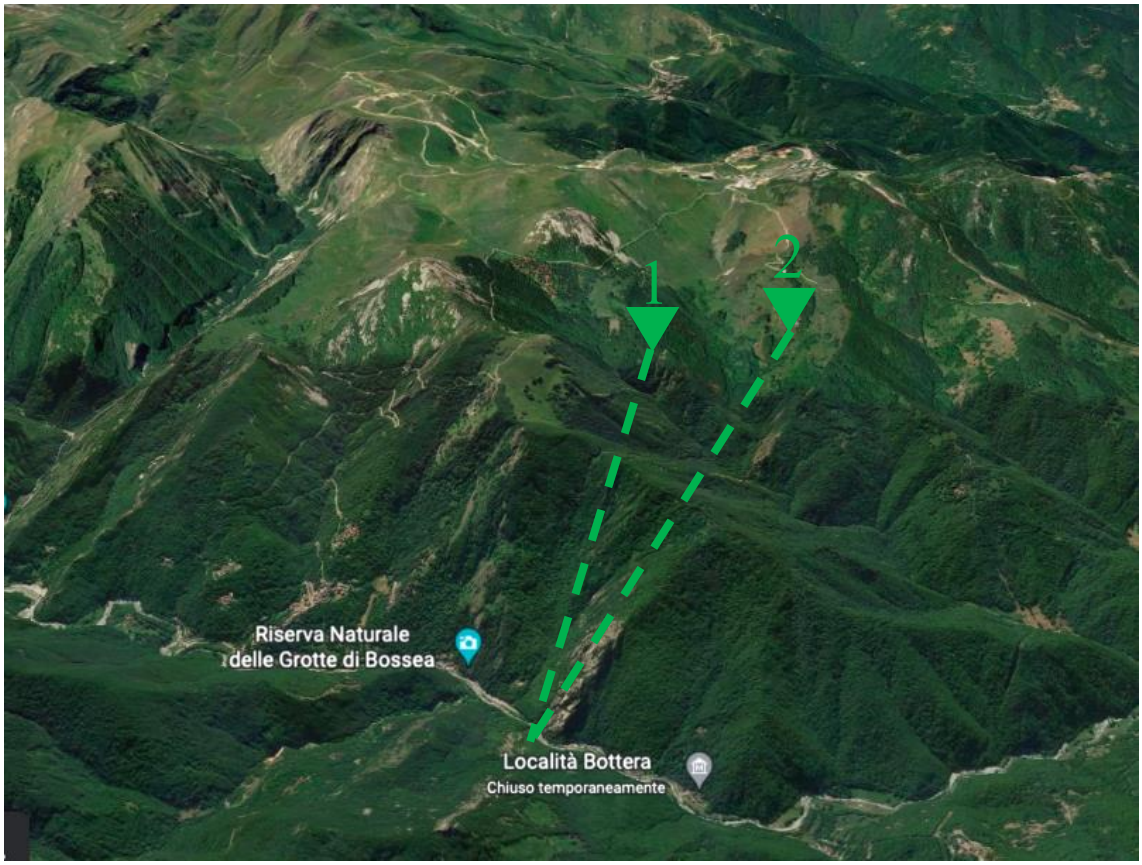

Figure 3.18 Tracing test. 1 Rio Roccia Bianca, 2 Rio Bertino (https://earth.google.com/web/)

The tests carried out in Bossea saw the simultaneous introduction of the two types of tracers in the Rio Bertino and Rio Roccia Bianca valleys which are the main absorbent valleys (Figure 3.18). The automatic acquirer was then installed at Bossea to verify the connection. The following restitution curves were then obtained (Figure 3.19), from which it can be seen that the water from Rio di Roccia Bianca leaks arrive in Bossea in a shorter time and with a much higher concentration than that from Rio Bertino.

The same test carried out at Rio Roccia Bianca was repeated under different hydrological conditions of the system (during flood, normal and dry conditions), obtaining the breakthrough curves shown in Figure 3.20.

From the tracer breakthrough curves, one can easily estimate the maximum tracer flow velocity, shown in Table 3.3.

Further tracing tests were carried out in the area above the cavity to assess how the water flows in the 'unsaturated' zone, where the subterranean flow moves through the small fracture network of the rock mass, giving rise to the aforementioned secondary seepages. The arrival curves show how the tracer moves much more slowly, with flow velocities between 30 and 60 m/day. In Figure 3.20 the fluorescein arrival is very prolonged in time (more than a month due to the considerable dispersion in the fracture network) with temporary decreases in concentration due to the arrival and mixing of new water.

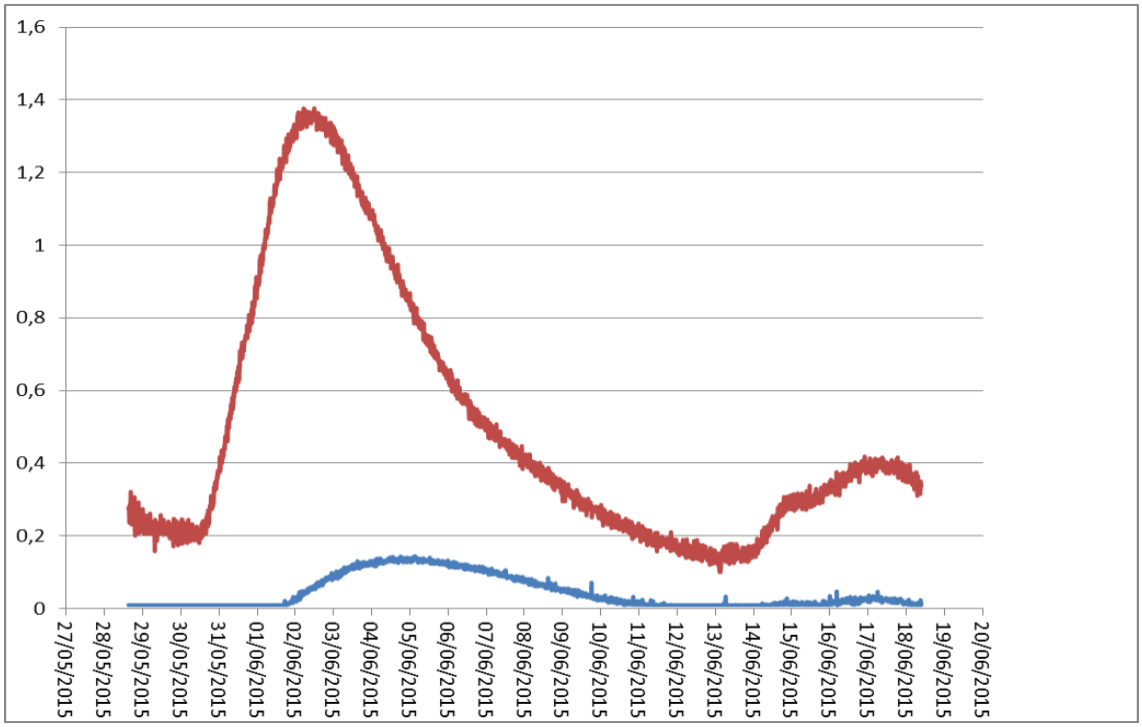

Figure 3.19 In red the restitution curve of Roccia Bianca (peak after 5 days), in blue from Rio Bertino (peak after 7 days). On Y axis Dye concentration [ppb]. Source Vigna, 2020

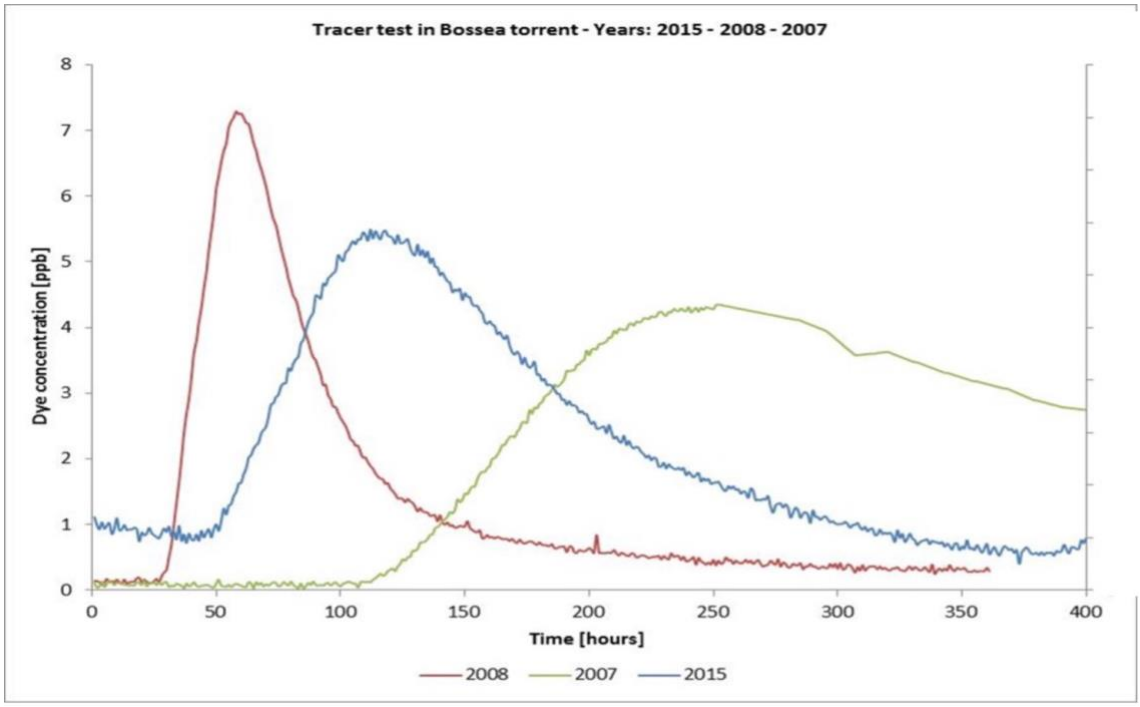

Figure 3.20 Red: during a flood event, blue normal flux conditions, green low water level conditions. Source Vigna, 2020

Bossea supply area deduced from hydrogeological surveys, tracer tests, and the hydrogeological balance is depicted in Figure 3.21. It extends as far as the Rio Roccia Bianca and Rio Bertino, reaching as far as the Colle del Prel (Figure 3.22 and Figure 3.23) for a total area of 5.55 km^2. It is mainly represented by steep SE-facing slopes with bare rock outcrops alternating with stretches of mixed deciduous and larch woodland and a thin soil cover. The steep morphology at the surface limits infiltration, especially during heavy storms (Figure 3.24).

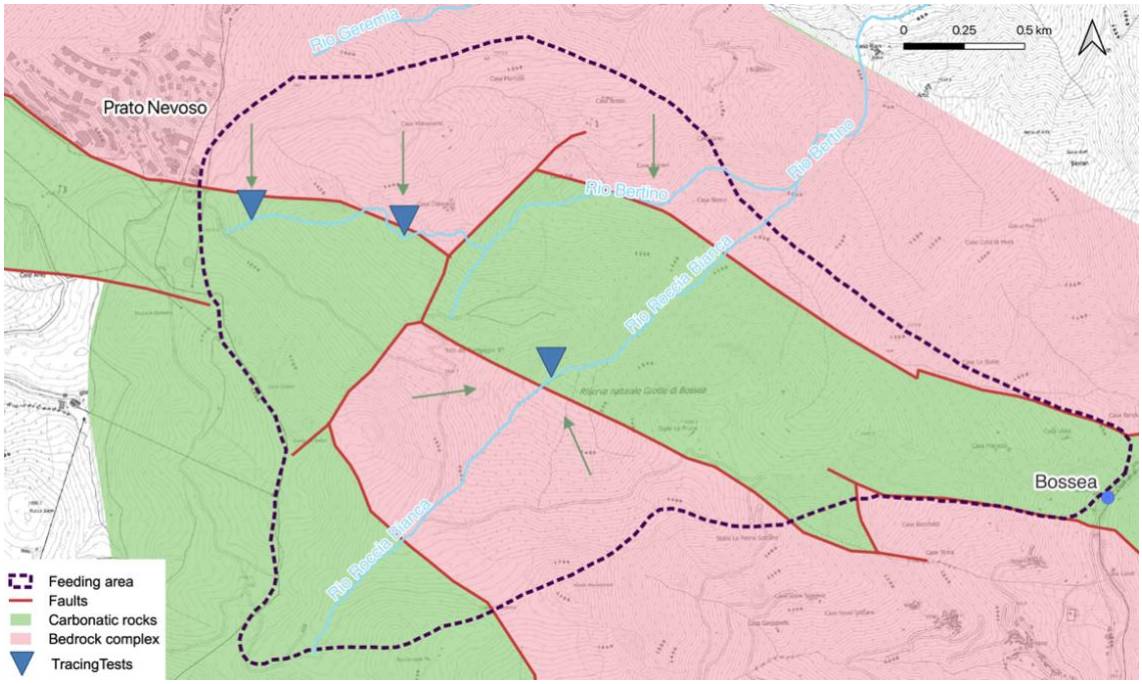

Figure 3.21 Tracing tests in the catchment area of Bossea

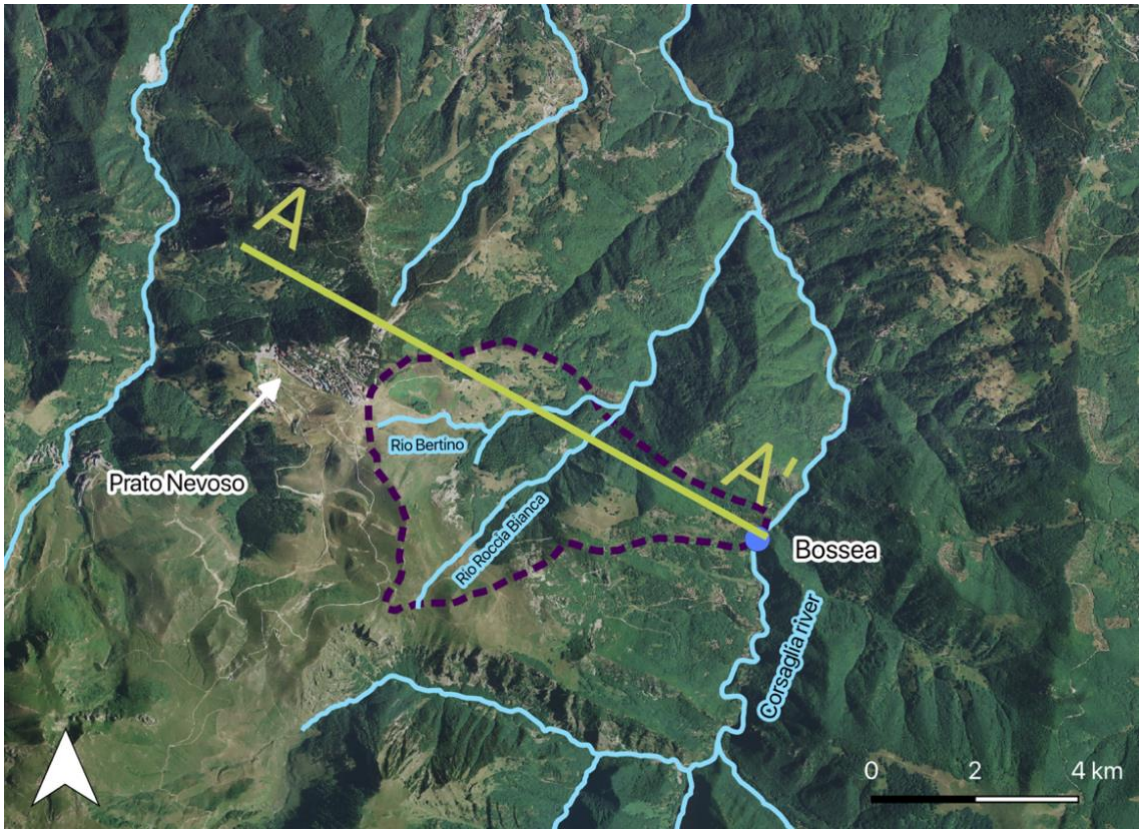

Figure 3.22 Plan of the section A-A'

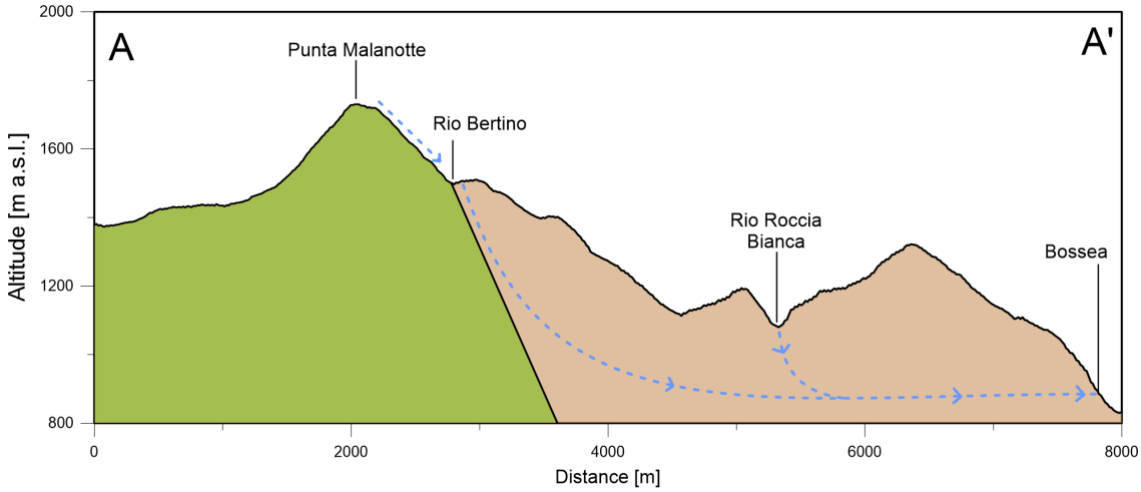

Figure 3.23 Section A-A' in the catchment area of Bossea. In brown limestones, in green the basement complex

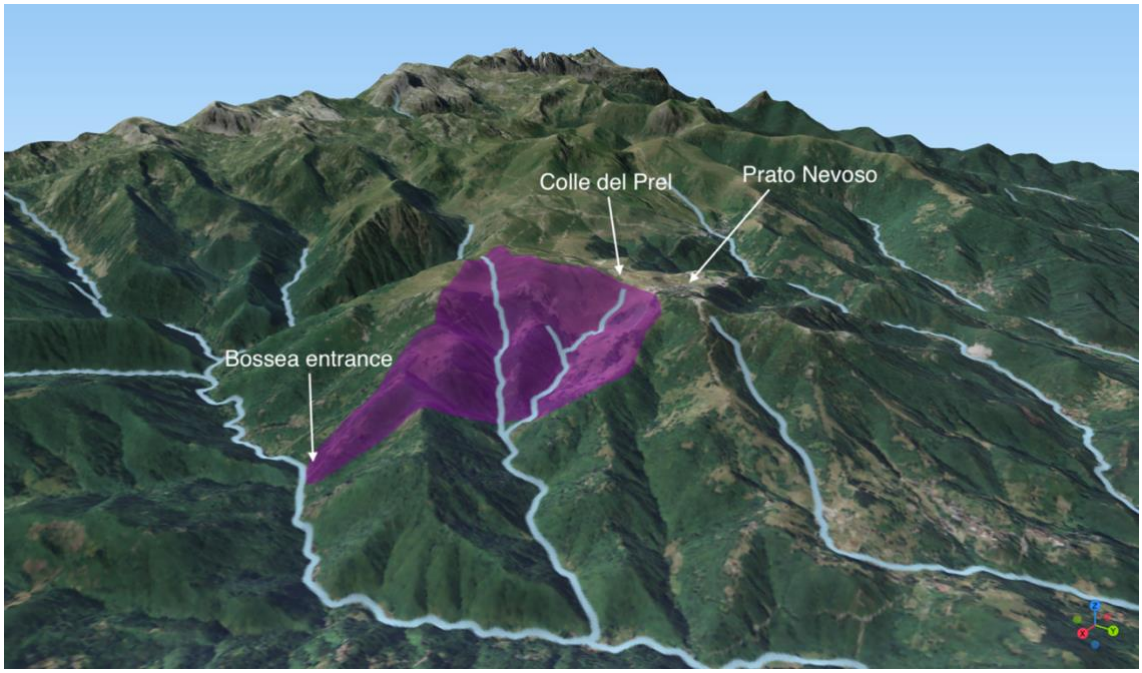

Figure 3.24 View of the area over Bossea. In purple the catchment area

In 2019, a laser scanner and total station survey were carried out inside the cave, and a drone flight outside it. This resulted in an accurate 3D model of the cave morphology and the rock thicknesses above it (Figure 3.25 and Figure 3.26).

As can be seen, one of the points closest to the surface turns out to be Sacristy, although it is already inside the main halls. As will be seen later, this factor is of particular interest for the study of temperatures at this station.

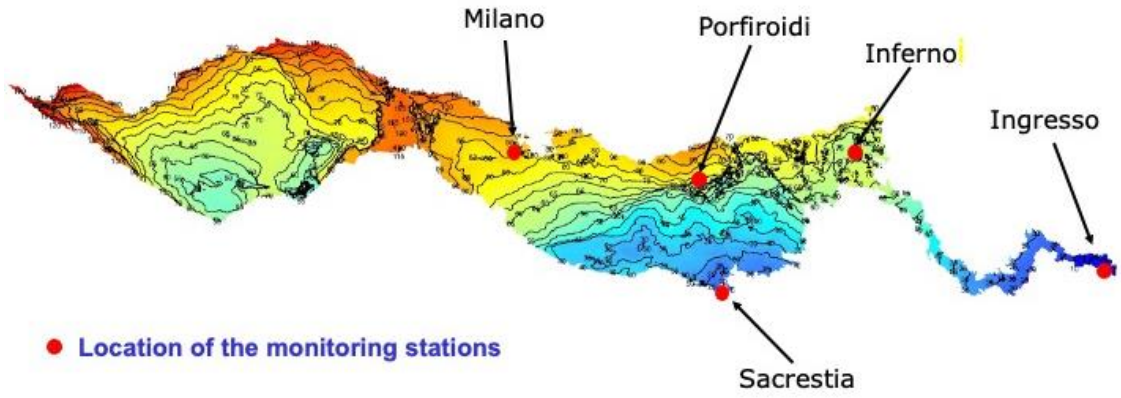

Figure 3.25 Rock thicknesses above the cave

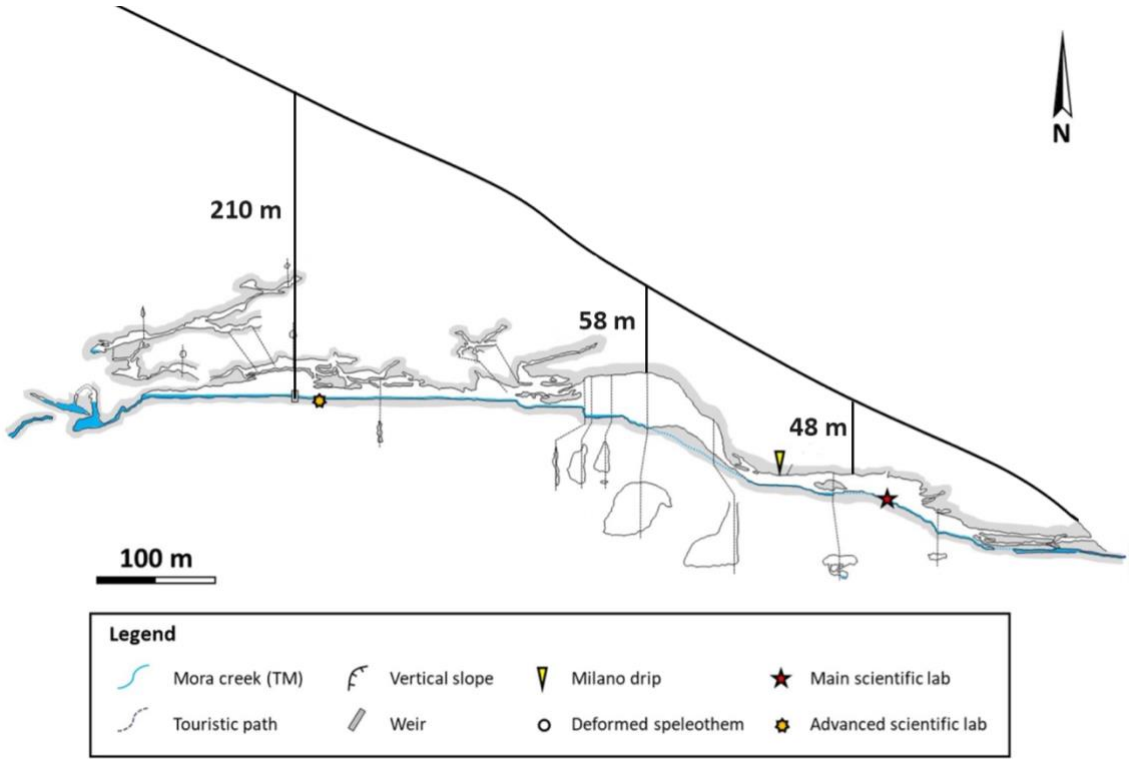

Figure 3.26 Rock thicknesses in the area above Bossea (Antonellini et al., 2019)

3.4 Bossea as a show cave

It is first necessary to define what is meant by show caves. A show cave defined as "a natural occurring void beneath the surface of the earth that has been made accessible to the public for tours" (Cigna, 2019). Show caves are typically equipped with lighting, pathways, and other features that make them accessible and safe for visitors to explore. The goal of a show cave is to provide visitors with an educational and entertaining experience, while also protecting the natural environment of the cave.

Show caves often constitute a hub around which tourist facilities are built, contributing to the economic livelihood of the local population. In the context of Italian tourist caves, the Grotta di Bossea is of fundamental importance. As a show cave, Bossea attracts a large number of visitors each year, both from Italy and from around the world. The cave is known for its unique features, such as the underground lake and waterfalls, as well as

the impressive stalactites and stalagmites that adorn its chambers. Visitors can explore the cave on guided tours, which provide information about the cave's geology, history, and ecology.

An accurate account of the flow of tourists has been kept in recent years (Figure 3.27 and Figure 3.28). The year 2021 was affected by the covid pandemic and the cave was closed for the first months of 2021. There were 11631 visitors during the opening period (1/05/2020-31/12/2020), peaking on 15/08/2021 (237 visitors). The absence of visitors for part of the year provided a unique opportunity to collect data and conduct studies that are not affected by the presence of people.

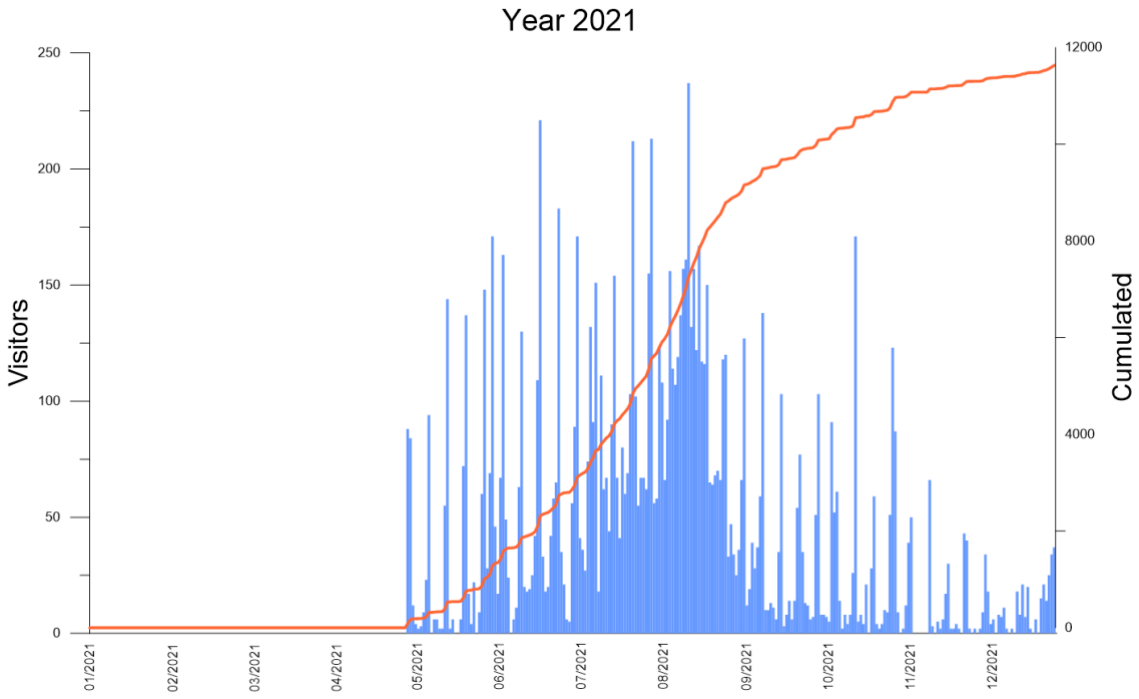

Figure 3.27 Tourist flow during the year 2021

The total number of entries recorded in 2022 was 17471, with the highest number of visitors reaching a peak of 407 people on August 15, 2022, which is a public holiday in Italy. As expected, there is a significant contrast in the number of tickets sold between weekdays (with an average of approximately 25 people per day) and holidays (with an average of 95 people per day) for both years. This difference is clearly visible in both Figure 3.27 and Figure 3.28, with peaks at weekly intervals and corresponding changes

in the cumulate slope illustrating the distinct patterns of ticket sales between these two types of days.

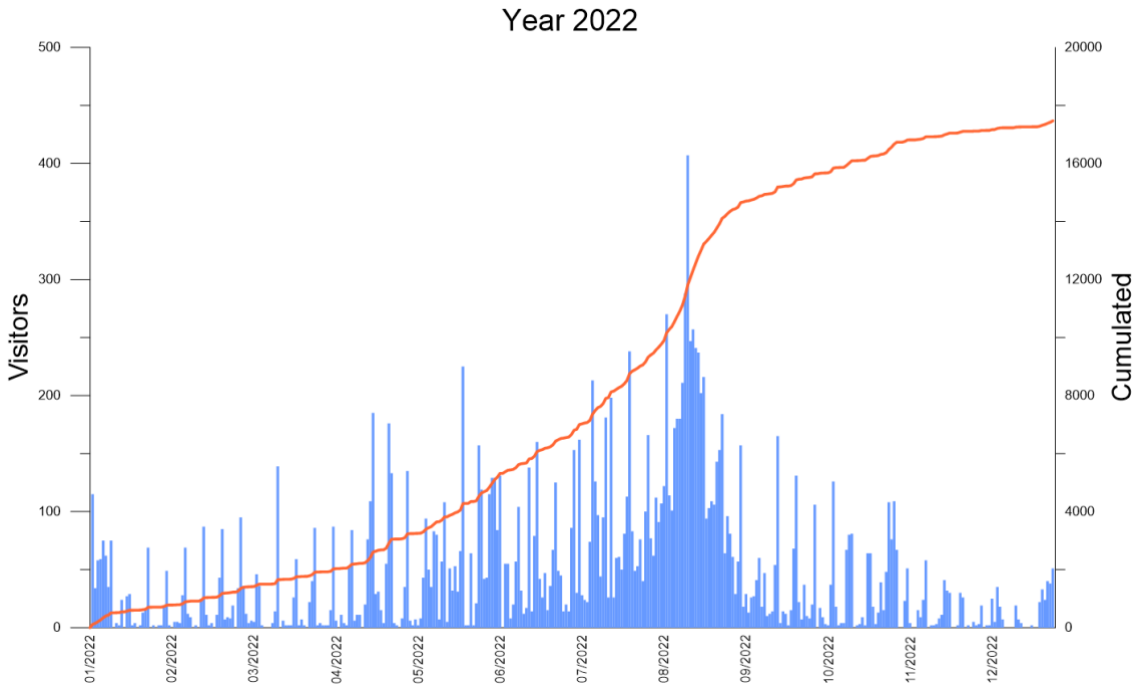

Figure 3.28 Tourist flow during the year 2022

4 Instrumentation used for data analysis

4.1 Historical background

The "Underground Karst Laboratory of the Bossea Cave," located inside the cave, is a scientific research organization affiliated with the Bossea Operating Structure of the Italian Alpine Club Headquarters. It serves as a national center for karst studies and conducts ongoing research in various fields, including karst hydrogeology, hypogean meteorology, natural radioactivity, and biospeleology. The Laboratory has been collaborating continuously with the Politecnico di Torino since 1983, and since the mid-1990s, it has also engaged in periodic collaborations with other scientific research institutions specializing in environmental radioactivity.

The Bossea laboratory was established in October 1969 by a team of members within the Maritime Alps Speleological Group of the CAI of Cuneo (Peano, 2002). They set up the first equipment in the lower part of the cave to study the fauna and flora typical of the underground environment. Initially, a hydrometric station and a few thermometric stations were installed in the upper part of the cave for the hydrogeological and climatological study of the cavity. Subsequently, all the instruments outlined in this chapter were progressively installed, making Bossea the most prominent and comprehensive underground karst laboratory in operation in Italy and one of the firsts on the European continent.

Since its first equipment, the cave has undergone two several main additions: during the ’80s “laboratorio superiore” was installed in the upper part of the cave, while in the early ‘90s took place the “Sacrestia” lab installation (Figure 4.1). Compared to Laboratorio

Superiore, the latter has the advantage of being accessible even during flood events and being far from the tourist path, so it is now the main laboratory of the cave.

Figure 4.1 Bossea Cave main lab (Sacrestia)

4.2 Instrumentation localization

The cave has a high density of instrumentation, mainly concentrated in the main laboratory. To correctly interpret the data, a good 3D understanding of the space in which they are placed is crucial.

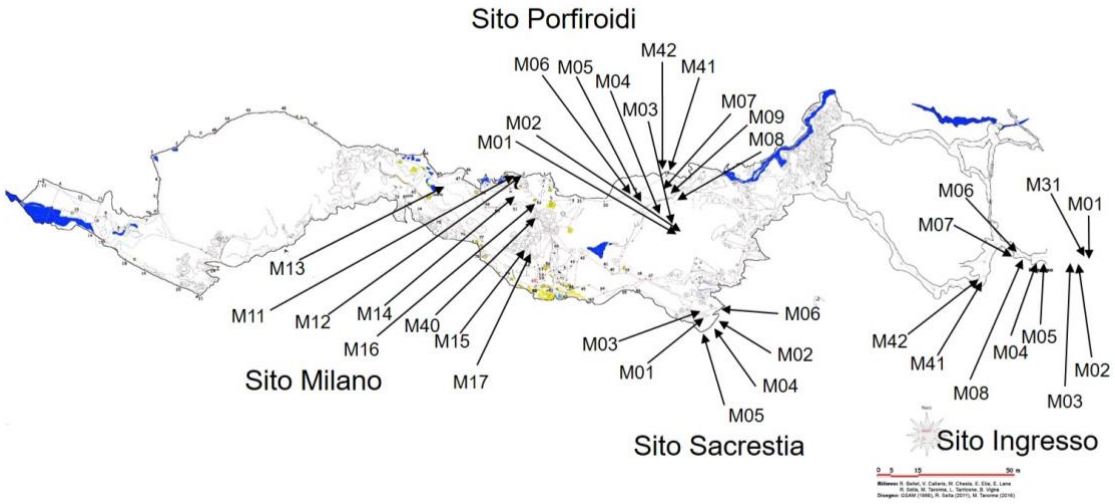

Figure 4.2 Location of instruments (source: Bartolomeo Vigna, 2023)

The four main instrument installation sites are shown in Figure 4.2 with the respective codes for each probe.

4.2.1 Ingresso

Ingresso, "entrance" in Italian, is the first measurement site found when approaching the cave entrance. Part of this site is located outside the cave and part is inside.

On the outside, in addition to 2 rock sensors at different depths (M02 and M03, 50 cm and 100 cm deep respectively) Figure 4.3, there are:

- A cup anemometer;
- Two pluviographs, one heated and one not;
- An air temperature (M01, Figure 4.3), pressure (M01, Figure 4.3) and humidity sensor;

- Air temperature sensor near ground;
- Two rain temperature sensors;
- One snowmelt flow meter;

The other two rock temperature sensors (M04 at 1 m and M05 at 0.50 m) are in a sheltered area of the entrance but not yet beyond the threshold of the cave.

The first ultrasound anemometer is placed on the threshold in the upper part. The second is placed on the floor, a few meters ahead and to the side, so as not to interfere with the tourist path.

Advancing into the cave, still following the fossil branch that characterizes this first cave portion, are found in order:

- M08, rock temperature sensor at 0,50 m depth;
- M06 and M07air sensors located at the shaft's top and bottom, respectively.
- M41 and M42, at the point called the 'switchboard', air temperature sensors at the shaft's top and bottom, respectively.

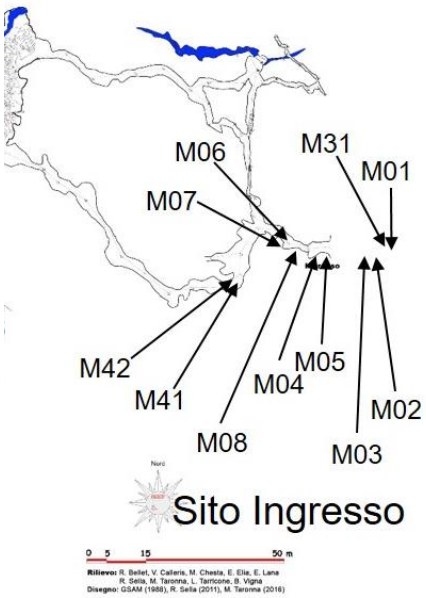

Figure 4.3 Ingresso site (source: Vigna, 2023)

4.2.2 Porfiroidi

Porfiroidi, also known as Porphyroids (Figure 4.5), is situated in the initial spacious chamber of the cave where the height of the chamber reaches a maximum of 40 meters. As visitors progress along the tourist trail, they will reach the station shortly after entering the hall.

Figure 4.4 Sensors protected against falling water drops

Instruments that measure air temperature are located at different heights in the section. The highest (about 15 m as the crow flies from the tourist path) is M06. We then find

M05 and M04, a few meters above and below the tourist path respectively, and M03 in the lowest part. M01 and M02 are located below the previously mentioned collapse debris because that is where the river flows. In fact, M01 measures the air temperature at a point very close to the Mora stream, and M02 measures its temperature. M01, due to the proximity of the stream and thus the very high moisture contents and low temperature, is clearly affected by condensation effects and thus cannot be considered as a proper measurement of air temperature, but more of the temperature of the sensor itself.

In order to limit the influence of the heat emitted by the rock, the air temperature sensors were placed on a cantilevered support, while to prevent condensation drops from falling directly onto the sensor, they were protected by a Plexiglas canopy (Figure 4.4).

M41 and M42 are positioned at the seepage Wave and are used to measure the rock temperature (at a depth of 0.5 m) and water temperature near the rock, respectively. Additionally, a multi-parameter probe that measures level, electrical conductivity, and temperature is inserted into the stilling basin of a small weir. This weir is mostly dry throughout the hydrological year.

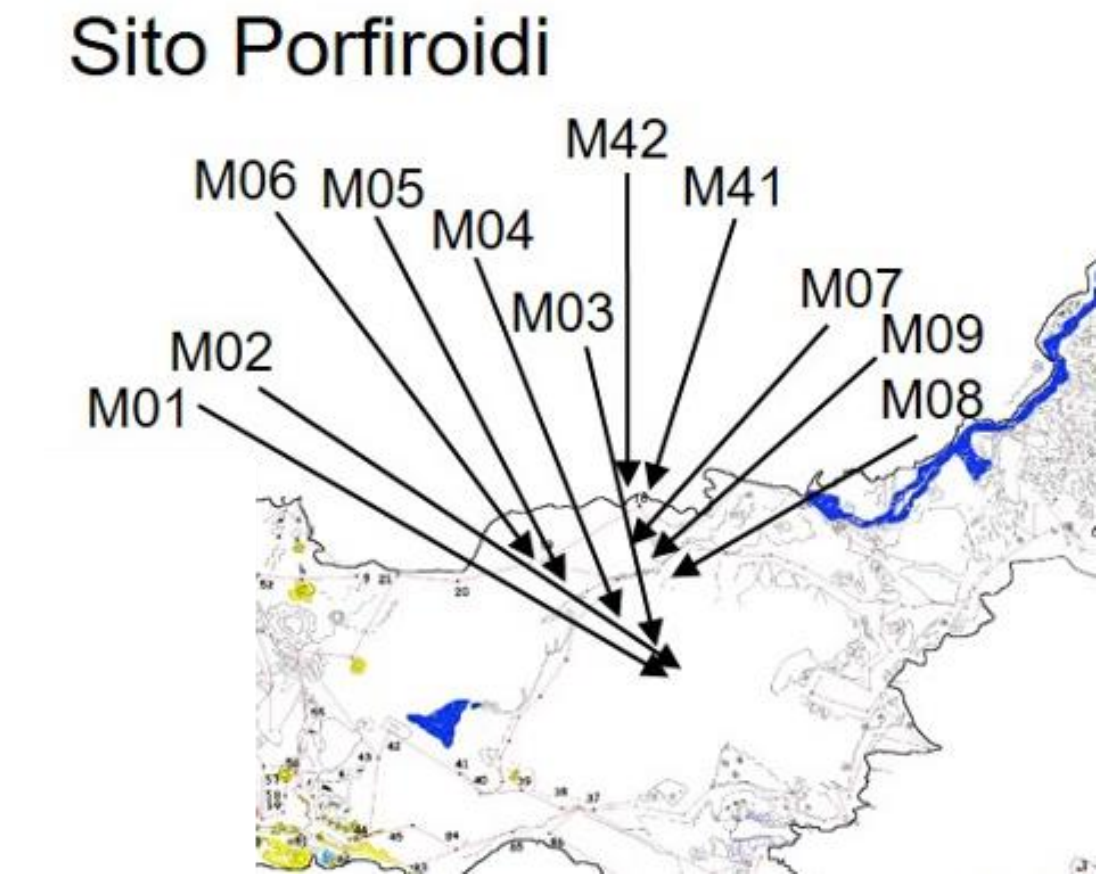

Figure 4.5 Porfiroidi site

4.2.3 Sacrestia

The Sacrestia site, "Sacristy", is located in the main laboratory, where the main radon measurements are made. Before the entrance to the laboratory, there are two CO_2 meters, one on the path and one on the ceiling.

In this small side room of the cave, which is the closest point to the outside surface, the following probes are located:

- Water temperature of water-bearing veins at depths of 0.45 and 0.25 m (called M01 and M03, respectively) and rock near them at the depth of 0.1 m (M02);
- Rock temperature at the depths of 0.5 and 1 m (M04, M05);
- Air temperature (M06).

This area is inaccessible to tourists and, although quite sheltered, is located near the Bear Hall, where the tour stops for a longer period. A plaza is made in this area where chairs are also set up and where shows such as concerts are occasionally held.

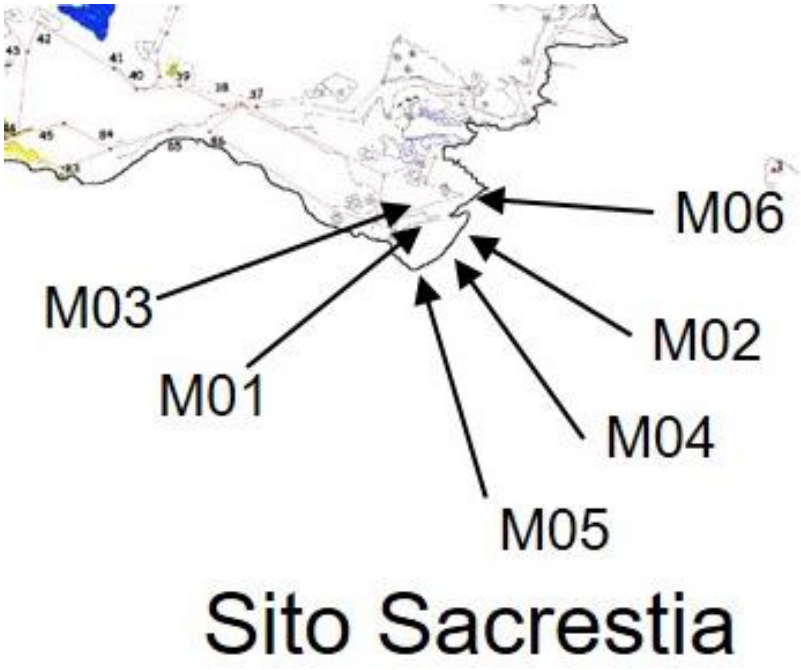

Figure 4.6 Sacrestia site

4.2.4 Milano

At the highest part of the hall is the Milan site. In this area, the main collector flows below the debris without surfacing. Here are located a pressure and temperature gauge, not calibrated by INRiM, the National Institute of Research and Metrology.

M11 and M12, are rock temperature sensors installed at depths of 0.5 m and 1 m, respectively. There is also one sensor for monitoring the temperature of the water seepage named Milan. Additionally, four air temperature sensors are placed at different locations, namely M14 which is installed on a rock block, M15 which is the lowest, M16 which is on the tip of a pole and hoisted using a system similar to that used for flags, and M17 which is installed near a hot-wire anemometer (which is not currently operational). Finally, two ultrasonic anemometers are situated just upstream of the Milano yard. One

is located on the ceiling, while the other is on the floor at the narrowest point in the salon cross-section.

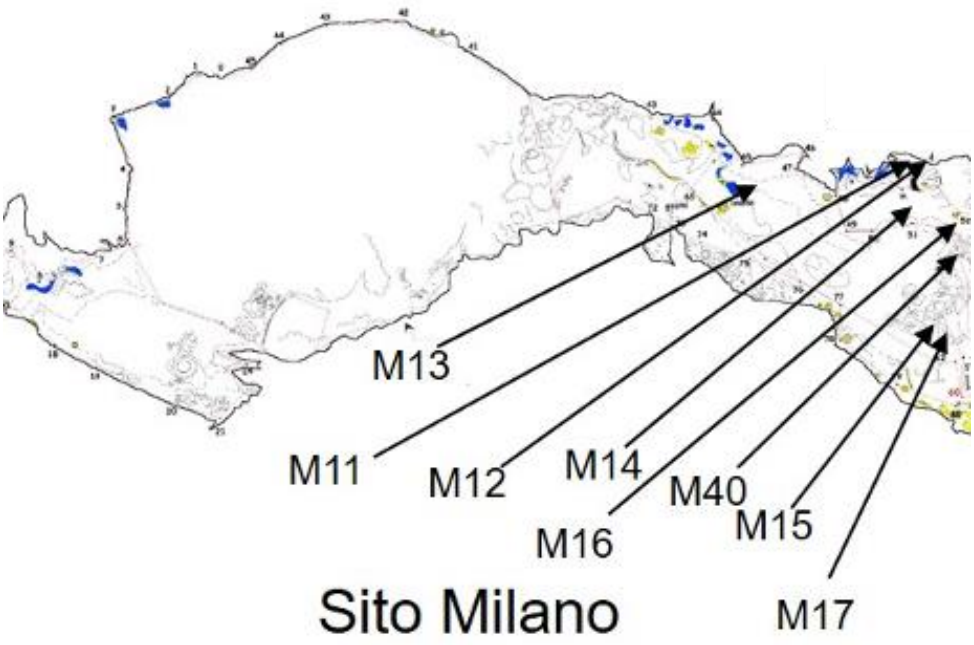

Figure 4.7 Milano site

4.2.5 Laboratorio superiore

At the end of the tourist trail is the Ernestina waterfall, which marks the end of the great hall area. Passing the waterfall, one enters a canyon that has a modest cross-section in his first part and where the upper laboratory is equipped (not shown in Figure 4.2 as not yet involved in the survey by laser scanner). There are found:

- 2 rock temperature sensors, one in the upper part of the section and one in the lower part;
- 2 air temperature sensors, one in the upper part of the section and one in the lower part.

There is also a temperature and pressure sensor, which has not been calibrated by INRiM.

At this point Polla delle Anatre is found which, among the secondary water inlets, is the most important in terms of flow rate and is equipped with a small, thin-walled triangular weir in whose stilling basin a multi-parameter probe (level, temperature, and electrical conductivity) is deployed.

4.3 INRiM calibration

All the instruments from which the data were recorded underwent calibration.

Calibrations make it possible to determine the measurement errors to ensure more accurate and reliable measurement results ensuring traceability to SI (International System of Units). For Bossea cave instruments, the calibration was carried out by INRiM, the National Institute of Research and Metrology, which provides a comprehensive range of calibration and measurement services in the various areas of metrology, guaranteeing metrological traceability in accordance with the ILAC-P10 "ILAC Policy on the Traceability of Measurement Results" criteria.

To carry out the calibration, the unshielded sensors were immersed in alcohol in a PolyScience thermostat bath at the calibration points corresponding to temperatures of 0°C, 5°C, 8°C, 11°C and 14°C. An additional return to 8°C was carried out to assess hysteresis.

Prior to immersion, the sensors were placed in a specially created copper comparator block in order to increase the homogeneity of the comparison medium and reduce the associated uncertainty. Together with the sensors under test, three previously calibrated Pt100 sensors were inserted into the comparator block, which was read using a Fluke Superthermometer 1594A high-precision bridge. The values of the three references were averaged to obtain the average temperature of the comparator block and the uniformity medium: the extreme values were also used to assess the homogeneity of the medium itself. Due to the limitation of only 10 channels for reading the sensors under test, four consecutive batches were required at each calibration point.

Calibration curves were therefore obtained, one for each instrument, in the format:

$$T_{corr} = a\,T_{read}^2 + (1+b)T_{read} + c \qquad 2$$

Where T_{read} is the temperature value read and a, b, and c are the three correction parameters.

The measurement uncertainty is the estimate linked to a test result that characterizes the range of values within which the true value of the instruments is assumed to lie. This was assessed by INRiM using the extended uncertainty quantity, i.e. the half-confidence interval of the measurement result and equal to Ut=0.03°C, given at a 95% confidence interval. It consists of the following components:

$$U_t = 2 * \sqrt{u_{st.dev}^2 + u_{res}^2 + u_{hyst}^2 + u_{stab}^2 + u_{spatial}^2 + u_{cal}^2 + u_{daq}^2 + u_{interp}^2} \qquad 3$$

- $u_{st.dev}$, statistical uncertainty due to the standard deviation of the sensor readings under test;
- u_{res}, uncertainty due to the datalogger resolution of the sensors under test;
- u_{hyst}, uncertainty due to hysteresis;
- u_{stab}, defined as the time average of the max-min measured by the three reference sensors during the acquisition;
- $u_{spatial}$, defined as the spatial average of the max-min measured by the external reference sensors;
- u_{cal}, calibration uncertainty of the reference;
- u_{daq}, reading uncertainty of the datalogger associated with the reference;
- u_{interp}, uncertainty due to mathematical interpolation.

This way, the corrected data were obtained, which will be used in the following analyses.

These sensors were calibrated using the aforementioned process on 08/06/21 and put into service on site from 26/06/21. Since the installation, INRiM researchers have visited Bossea every year for further instrument calibrations and to assess the instrumental drift.

In 2021, a similar inspection was conducted to test the functionality of the instruments installed at the end of 2019, specifically 31 temperature sensors calibrated using the

PolyScience thermostatic bath method described earlier. The inspection uncovered significant issues with at least 3 of the 6 sensors examined. When changing the channels to test the functionality of the sensors, an unusual behavior was observed, where the temperature readings appeared to be higher when a single probe was connected to the data logger, but immediately dropped when any other sonde was connected. To eliminate the possibility of connector-related issues, the connectors were disconnected from the sondes and switched randomly. The bad readings appeared to follow the probe during channel switching, indicating that the problem was unlikely to be caused by the connectors.

Sensors have then been checked through the same thermostatic bath at 11°C (one at the temperature points as calibration and the one closer to the actual temperature of the cave). The tested sensors showed a significant dispersion in their raw readings (from 8.9°C to 10.8°C), the three most problematic sensors are those for which errors had already been found in the room temperature reading, but all 6 seemed to have undergone significant changes in their resistivity properties.

As a final test, to check whether the sensors had suffered insulation leakage and whether water, due to the high humidity of the cave environment, had penetrated the capsule and the sensing elements. The sensors have been put in a Kambic climatic chamber model MeteoCal, at 35 °C and 10 % of relative humidity, and left there for several days, to dry the sensors as much as possible. While 3 days after the start of the test the sensors showed the same dispersion as previously tested (Table 4.1), after 12 days the values were very close to the correct one (

Table 4.2), confirming the hypothesis that the malfunctions were due to some sort of insulation failure and water infiltration inside the sheath.

Table 4.1 Resistance measured in a climatic chamber at 35 °C and 10 % RH after three days of the connector-less sondes.

	Resistance (ohm)

M01	112.71
M02	113.54
M03	113.53
M04	112.99
M05	113.31
M06	113.56

Table 4.2 Resistance measured in climatic chamber at 35 °C and 10 % RH after twelve days of the connector-less sondes.

	Resistance (ohm)
M01	113.47
M02	113.55
M03	113.55
M04	113.54
M05	113.55
M06	113.56

For this reason, many of the sensors were changed or sent back to the mother company to be corrected and then re-installed or installed as new until they assumed their current configuration, which was described in the previous chapter.

4.4 Data availability

The cave environment is notoriously complex for the installation of instrumentation. The humidity is in fact around 100% and, as previously noted, can cause damage to the instrumentation resulting in measurement errors that are not always so easy to recognize.

To limit this effect, electrical resistances have been installed, in the acquisition boxes that are not watertight, which, by heating the small environment, prevent condensation inside them (Figure 4.8).

Like the electrical resistances, much of the instrumentation in Bossea requires electricity for its operation. While it is easy to access, given that Bossea is a show cave, there is a strong dependence on it: power supply failures and voltage dips are in fact the main causes of data gaps.

For each sensor at each station, the period in which data are available are given in Table 4.3, Table 4.4, Table 4.5, Table 4.6 and Table 4.7.

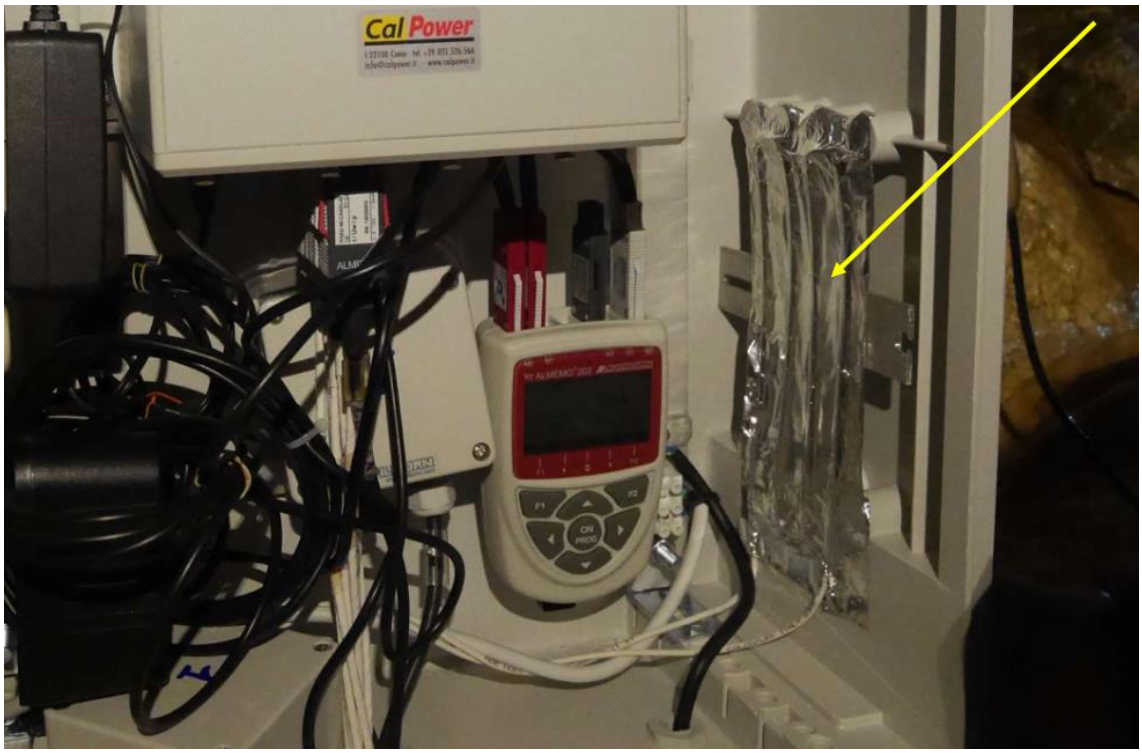

Figure 4.8 Electrical resistor inside the multi-channel data logger (source: Bartolomeo Vigna, 2022)

Table 4.3 Ingresso data availability

	I data interval		II data interval		Total amount of data [days]
M01	13-mag-21	9-mag-22	9-giu-22	6-set-22	450
M02	23-giu-21	9-mag-22	9-giu-22	6-set-22	409

M03	23-giu-21	9-mag-22	9-giu-22	6-set-22	409
M04	23-giu-21	9-mag-22	9-giu-22	6-set-22	409
M05	23-giu-21	9-mag-22	9-giu-22	6-set-22	409
M06	23-giu-21	9-mag-22	9-giu-22	6-set-22	409
M07	23-giu-21	9-mag-22	9-giu-22	6-set-22	409
M08	23-giu-21	9-mag-22	9-giu-22	6-set-22	409
M31	13-mag-21	9-mag-22	9-giu-22	6-set-22	450
M41	13-lug-21	9-mag-22	9-giu-22	6-set-22	389
M42	13-lug-21	9-mag-22	9-giu-22	6-set-22	389

Table 4.4 Porfiroidi data availability

	Data interval		**Total amount of data [days]**
M00	22-giu-21	6-set-22	441
M01	22-giu-21	6-set-22	441
M02	22-giu-21	6-set-22	441
M03	22-giu-21	6-set-22	441
M04	22-giu-21	6-set-22	441
M05	22-giu-21	6-set-22	441
M06	22-giu-21	6-set-22	441
M07	22-giu-21	6-set-22	441
M08	22-giu-21	6-set-22	441
M09	22-giu-21	6-set-22	441
M41	22-giu-21	6-set-22	441
M42	22-giu-21	6-set-22	441

Table 4.5 Sacrestia data availability

	Data interval		**Total amount of data [days]**
M01	22-giu-21	6-set-22	441
M02	22-giu-21	6-set-22	441
M03	22-giu-21	6-set-22	441
M04	22-giu-21	6-set-22	441
M05	22-giu-21	6-set-22	441
M06	22-giu-21	6-set-22	441

Table 4.6 Milano data availability

	Data interval		Total amount of data [days]
M11	22-giu-21	6-set-22	441
M12	22-giu-21	6-set-22	441
M13	22-giu-21	6-set-22	441
M14	22-giu-21	6-set-22	441
M15	22-giu-21	6-set-22	441
M16	22-giu-21	6-set-22	441
M17	22-giu-21	6-set-22	441

Sensors M10 and M40 in the Milano site have been particularly problematic. The data availability is shown in Table 4.7.

Table 4.7 Milan data availability for M10 and M40

	I data interval		II data interval		III data interval		Total amount of data [days]
M10	13-mag-21	10-nov-21	23-dic-21	8-lug-22	14-lug-22	6-set-22	432
M40	13-mag-21	10-nov-21	23-dic-21	8-lug-22	14-lug-22	6-set-22	432

Regarding the data acquisition interval, they are recorded every 10 minutes for the air/water/rock temperature data listed above. The same applies to electrical conductivity and secondary flow levels. As far as the main collector is concerned, data are acquired every 15 minutes.

5 Air circulation results

Although the air in caves is considered to be much more stable than the outside atmosphere since it is not directly affected by solar radiation and other atmospheric factors, it cannot be seen as constant, neither in terms of temperature, nor in terms of movement (Badino G, 1995; De Freitas, 1987; De Freitas & Schmekal, 2006; Kašing & Lenart, 2020; Luetscher et al., 2008; Pflitsch et al., 2010) and the variation of airflows in time and space remains an open question in many situations. The study of cave atmosphere, although a circumscribed topic, is of fundamental importance among other subjects for palaeoclimatology (Affolter et al., 2015; Domínguez-Villar et al., 2013; Riechelmann et al., 2013), for the protection of the cave environment from anthropic impacts (Pulido-Bosch et al., 1997; Šebela et al., 2019; Šebela & Pipan, 2015; Šebela & Turk, 2011, 2014) and for being a receptacle of endemic fauna (Medellin et al., 2017).

The climate in the cave environment is dominated by two fluids (Badino G, 1995; Luetscher & Jeannin, 2004) and one solid (Salmon et al., 2023): air, water and rock. Water is found in both liquid and gaseous form (due to moisture, De Freitas, 1987). Under special conditions, it may also be present in the form of ice (Luetscher et al., 2008).

Four thermodynamic quantities characterize air (Lismonde, 2002):

- Mass density: the mass contained in the unit volume. Air density depends on his temperature, pressure, and composition. For instance, air density will be 1.225 kg/m³, considering a volume of dry air at 15°C and 105 Pa. As the other gases, as air heats up it expands, decreasing in density and becoming lighter. At the same time, since water has a lower molar weight than air (18 g versus 28.9 g), moist air, which is composed of air and water vapour, is lighter than dry air.
- Pressure: normally measured in Pa. If one imagines isolating a cube of air and replaces external actions with forces, pressure is the normal stress that should be

applied to replace the air outside the imaginary cube (Lismonde, 2002). Through its gradient, it is one factor that makes the fluid move. Atmospheric pressure is of the order of 10^5 Pa and varies in time (due to physical changes e.g. the temperature variations) and in space (it changes with altitude).

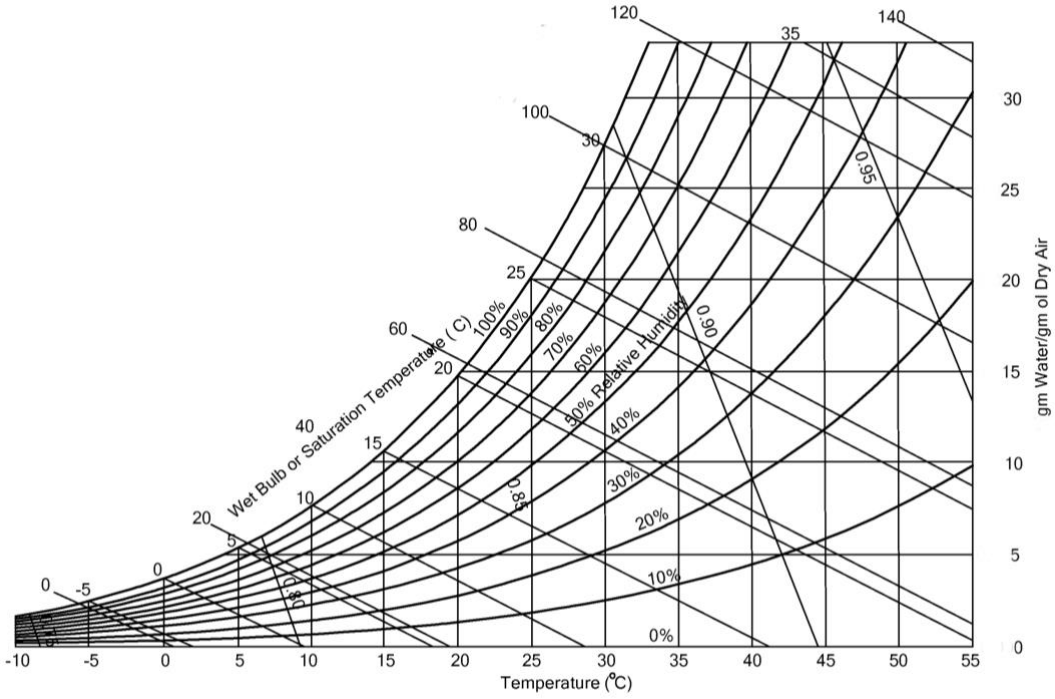

Figure 5.1 Psychrometric chart

- The temperature of a gas is related to the kinetic energy of its particles, with higher temperatures indicating greater particle agitation. In subsurface climatology, temperatures ranging from -10°C to +35°C are typical (Lismonde, 2002). As altitude increases, both in the troposphere and in caves, the air temperature generally decreases (Badino G, 2010). While the atmospheric temperature gradient is -6.5°C/Km, this can vary depending on factors such as latitude, time of year, and weather conditions (Badino G, 2010). In contrast, the temperature gradient in caves can vary widely and is typically between 2.8 to 5°C/km, depending on the climatic conditions (Badino G, 1995; Jeannin P-Y, 1989; Jeannin P-Y et al., 1997).

Temperature also affects air humidity since the latter is directly proportional to it. According to the psychrometric diagram (Figure 5.1), air with a particular temperature can only contain a limited amount of water vapour at atmospheric pressure, and this amount increases as the temperature rises. Hence, changes in temperature can lead to either condensation or water evaporation. In caves, where air saturation levels are often near 100%, visible examples of this phenomenon are observed. For instance, when saturated air in thermal equilibrium with the cave exits and undergoes a temperature drop, it condenses some of its water vapour content. Conversely, during summer, cooler air entering the cave condenses near the entrance.

- Velocity: is a vector. If we impose a straight pipe in which air moves, the average perimeter velocity is parallel to the pipe. However, in instantaneous measurements it can be directed in any direction due to turbulence and geometry of the conduit.

5.1 Air current

The cave environment, although protected from some of the atmospheric factors, is an open environment that exchanges with the outside atmosphere flows of matter (mostly air and water but also solid one) and energy mainly in the form of heat (Badino G, 2010). By assessing the influence of external temperatures (with the resulting variations) on the cave environment, three zones can be recognized:

1. A transition zone in which the outdoor effect is still very visible in daily temperature cycles. This zone can be called “heterothermic” (Luetscher & Jeannin, 2004).
2. A neutral zone in which external effects are counterbalanced by internal effects (rock and water). Daily variations, under normal conditions, are absent, while seasonal variations are within the range of 1-2 °C (Badino G, 2010).
3. A homogeneous zone that is unaffected by external variations. This zone can be called “homothermic”.

These three zones are a broad generalization because they depend on the geological and speleogenetic setting. As will be discussed later, in Bossea the partition is not so clear-cut since there is the presence of the Mora stream and anthropogenic passage.

Three processes that generate air currents will be analyzed in the next chapters: the first, forced convective circulation, is due to the fact that, since the density of the cave air is fairly constant because of fairly constant temperature and humidity, there is always a disequilibrium between external and internal atmosphere.

The second, on the other hand, is barometric circulation. It happens because the cave is a reservoir of air that struggles to escape from the entrances. Changes in atmospheric pressure force the cave to expel or draw in air to equilibrate them.

The third is due to the entrainment phenomena of water circulation, particularly that of the main collector.

5.1.1 Barometric circulation

In caves that have entrances (one or more) with small sections relative to the volume of air inside, exchanges between atmospheric and cave air are rather limited (Lismonde, 2002) .This characteristic is directly related to cave response times, which increase as the internal volume increases and the cross-section of the openings decreases. A scheme of current exchange due to barometric effects is shown in Figure 5.2 (Gomell et al., 2021). If it is assumed that the pressure inside the cave equals the pressure outside, no air circulation is generated since the system is already in equilibrium (a). If the external pressure, on the other hand, increases, a negative pressure gradient (toward the cave interior) is established between the inside and outside of the cave. This gradient can't be equalized for the aforementioned reasons, could not be instantaneously balanced, causing a negative pressure inside the cave (b). This leads to an air movement from outside (high pressure) toward the cave interior (low pressure) to achieve the equilibrium. On the other hand, in the case of negative external pressure (c), by the same principle but in reverse, the cave will blow air. Another example is shown in (Figure 5.3, d.)

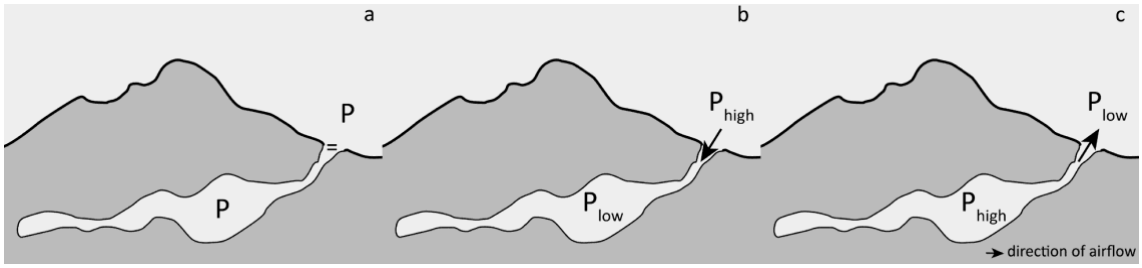

Figure 5.2 1. Schematic representation of an idealized barometric cave system for three different pressure and airflow situations (Gomell et al. 2021): a) equalized pressure between the air column inside and outside the cave: no compensating airflow; b) relative atmospheric overpressure: compensating airflow toward the cave, and c) relative atmospheric under pressure: compensating airflow from the cave.

5.1.2 Convective circulation

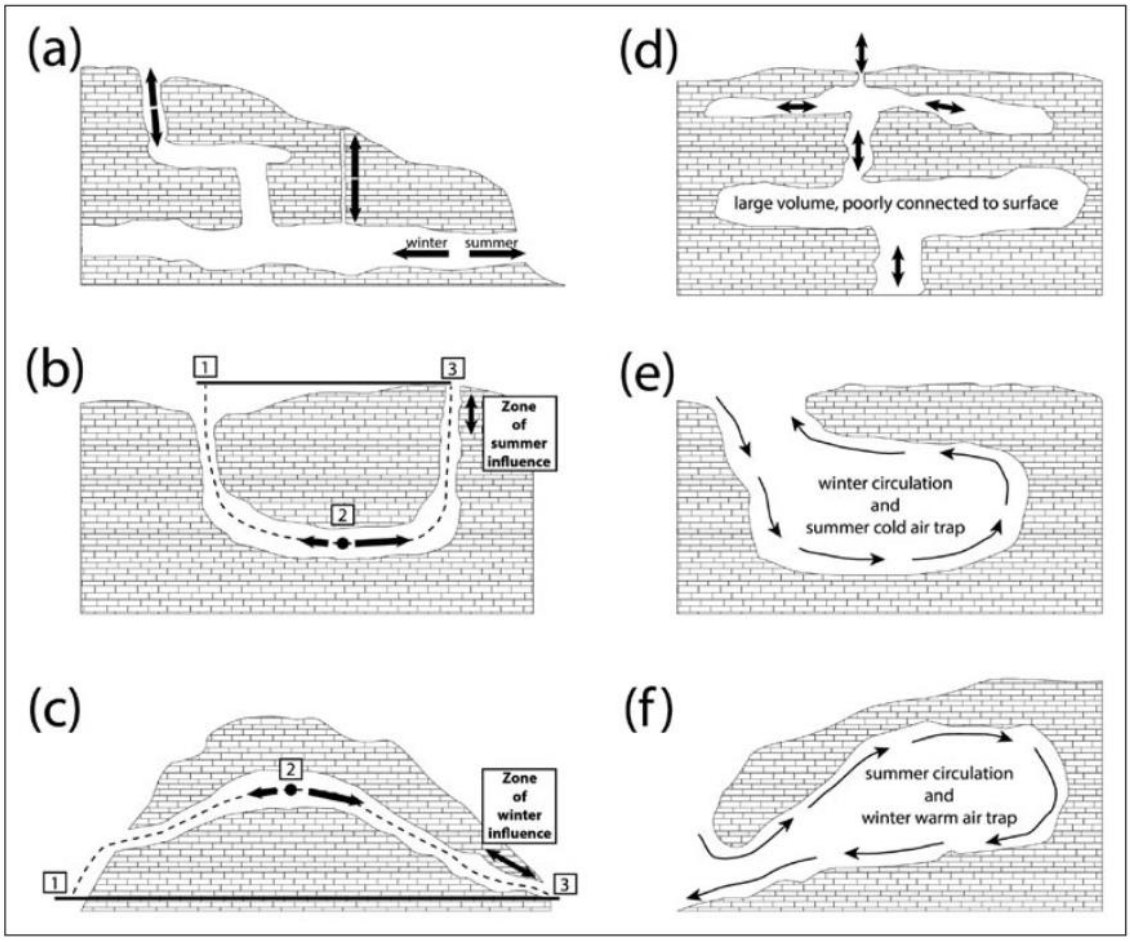

Figure 5.3 Illustrations of cave airflow mechanisms. (Covington & Perne, 2015)

Convective circulation is due to differences in air density between outside and inside and is often coupled with cave morphology (Badino & Chignola, 2019; Lismonde, 2002). In these cases, a distinction must therefore be made between summer and winter periods. In fact, in summer, the outside temperature is in most cases higher than the cave temperature. This leads, in cases of ascending caves (Figure 5.3, c. and f.), that the cold air inside the cave, heavier than the outside one, flows outside without opposition. The inside void is then filled with the warmer (and lighter) outside air. We speak in this case of a heat trap since the heat is stored inside the cave during the colder months, especially in the upper layers of the cave. In contrast, in the case of descending caves (Figure 5.3, b. and e.), by the same mechanism, colder (and heavier) air gradually enters the cave in winter and is then trapped in summer (Luetscher et al. 2008). The case of chimney effect caves (Figure 5.3, a.) occurs when a cave has two or more inlets at different altitudes. In this case, there will be descending air currents in summer and ascending air currents in winter.

At the time of inversion between the two regimes (a few weeks in autumn and spring) the airflow has even daily variations (due to day-night cycles and temperature trends outside).

5.2 The case study of Bossea

Bossea exhibits peculiar behaviour. Simplifying the cave model, the main features are:

- Only one entrance, represented by the tourist entrance: a semi-fossil branch, which will be called the Corridor, flooded only in case of exceptional floods. There is no other inlet that would allow air circulation. In the upstream part of the cave, there is the sump, which is completely flooded, while downstream the Mora flows into the Corsaglia through full-length conduits (Figure 3.3).
- The Mora flows only in the part of the large halls and not in the Corridor. Instead of running along the inlet branch, it infiltrates underneath it and then flows into the corsage, some fifty meters downstream.
- Upward trend: there are about 130 m between the entrance, located at 836 m asl, and the siphon.

5.2.1 Data set

In order to describe the air circulation inside the cave, the following air temperature data will be analyzed in this document:

- Entrance site: the outside temperature (M01), the entrance (M06, “ING High”, at the top and M07, “ING Low”, at the bottom) and the "electrical panel" site (M41, “QE High”, at the top and M42, “QE Low”, at the bottom).
- Porphyroids site: M03, M04, M05 and M06, from lowest to highest within the section. They will be called respectively Low Air, Medium Air, High Air, Very High Air.
- Milan site: M14, "Rock Block", M15 the lowest, M16, "CAI pole" and finally M17 called "Anemometer."
- Fondo site: one temperature at the top within the section and one at the bottom, very close to the water.

Since a strong influence is exerted by the temperature of the rock, they too will be analysed in parallel with the air temperature.

Entrance and electrical panel

The most superficial part of the cave has rather variable temperatures, correlating with the trend of the outside temperature, which has an average (calculated over the period June 2021-June 2022) of 9.8°C. The average, maximum and minimum temperatures recorded for each probe are shown in Table 5.1. The annual mean value was calculated for the 13 July 2021-13 July 2022 dataset. In order to obtain the annual average, the missing data gap was estimated, in the case of the outdoor temperature, by comparison with data obtained at the same point from a sensor installed by ARPA (the Regional Environmental Protection Agency). In order to obtain greater precision in the estimated data, the difference between the temperatures from the ARPA sensor and M01 during the year 2022 was calculated, except for the missing period (09/05/2022-09/06/2022). The average of the deltas thus obtained was then added to the ARPA sensor temperatures for

the missing period. The results are shown in Figure 5.5 while the two datasets (External and ARPA sensor) are shown in Figure 5.4.

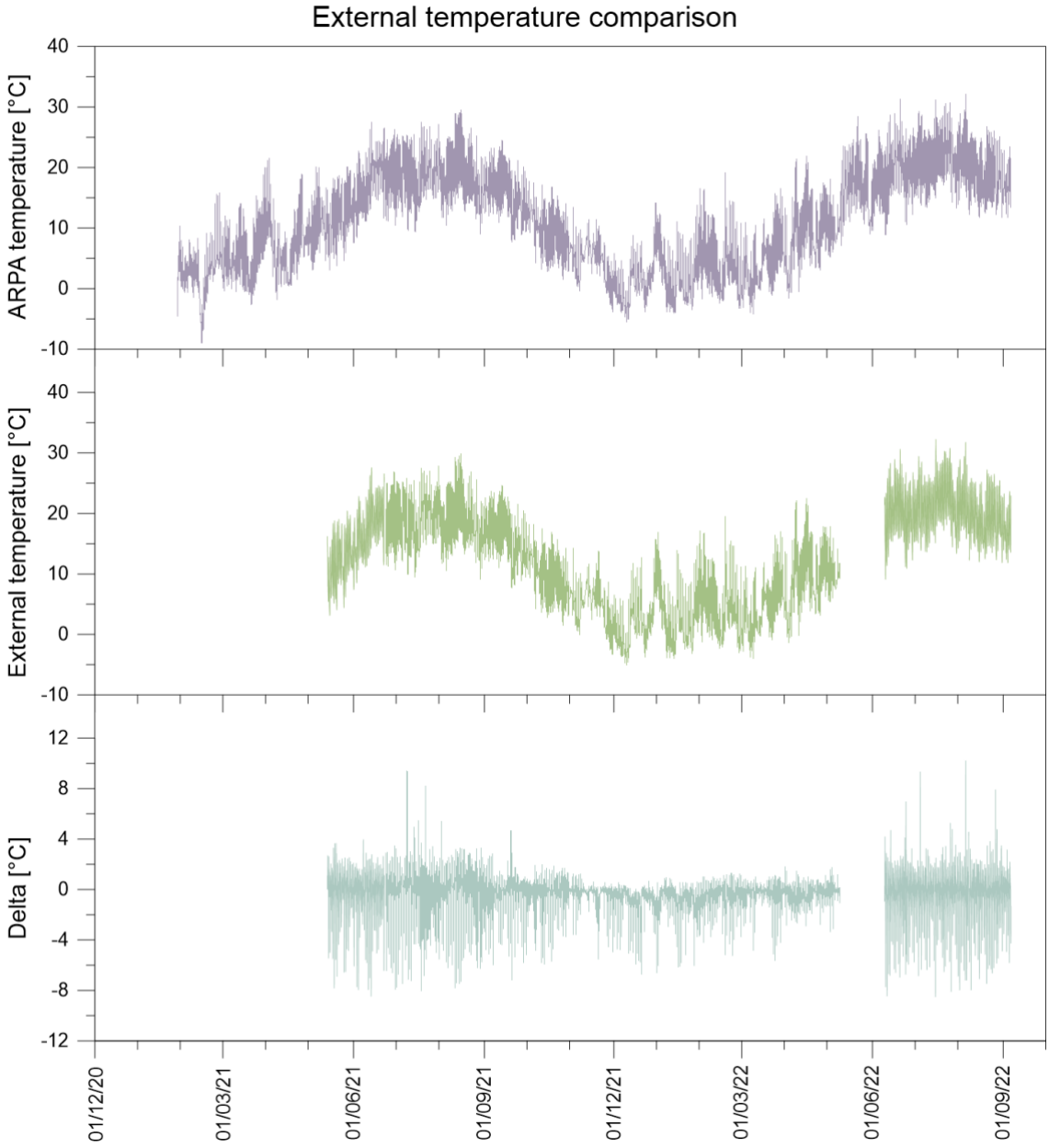

Figure 5.4 Comparison between ARPA and External data. ARPA data were used to interpolate the missing data at the External probe.

To estimate missing data for Entrance and QE sites, a linear interpolation approach was employed. Specifically, this involved using the data point immediately preceding the

missing data and the data point immediately following it to create a straight line, from which the missing data point was then estimated.

Table 5.1 Mean, maximum and minimum values for external probe, entrance (ING) and electrical panel (Q.E.)

	External	ING High	ING Low	Q.E. High	Q.E. Low
Max [°C]	32.22	19.26	13.81	12.68	11.44
Min [°C]	-5.10	6.81	1.19	9.48	8.52
Delta [°C]	37.32	12.45	12.62	3.20	2.92
Avg (07/21-07/22) [°C]	10.00	10.51	7.88	10.32	9.85

Looking at Figure 5.5, it can be seen that the sensor ING High undergoes large daily variations during the summer and fairly constant values during the winter, while the reverse is true for ING Low, which has large variations during the winter season and small variations during the summer season. The daily variations are due to the effect of solar radiation because of their proximity to the external environment.

As expected, temperatures dampen as one goes deeper into the cave: the electrical panel (Q.E. as "Electrical Panel" in the data set) is about 40 meters beyond the entrance.

The change in amplitudes of the probes between summer and winter, in an alternating manner between the ones at the ceiling and at the floor, provides evidence of two types of circulation in this first part of the cave. The first type takes place during the winter period. Bossea is not a descending cave like the one shown in Figure 5.3.e, but the corridor part is almost flat, with only a few tens of centimeters of negative height difference in the first few meters of the cave. During the winter period the largest signal amplitudes are concentrate at ING Low, showing the incoming air which enters the cave, brings itself into thermal equilibrium with it, and then exits, from the top of the entrance (ING High) with rather constant temperatures. The process is shown in Figure 5.3.e.

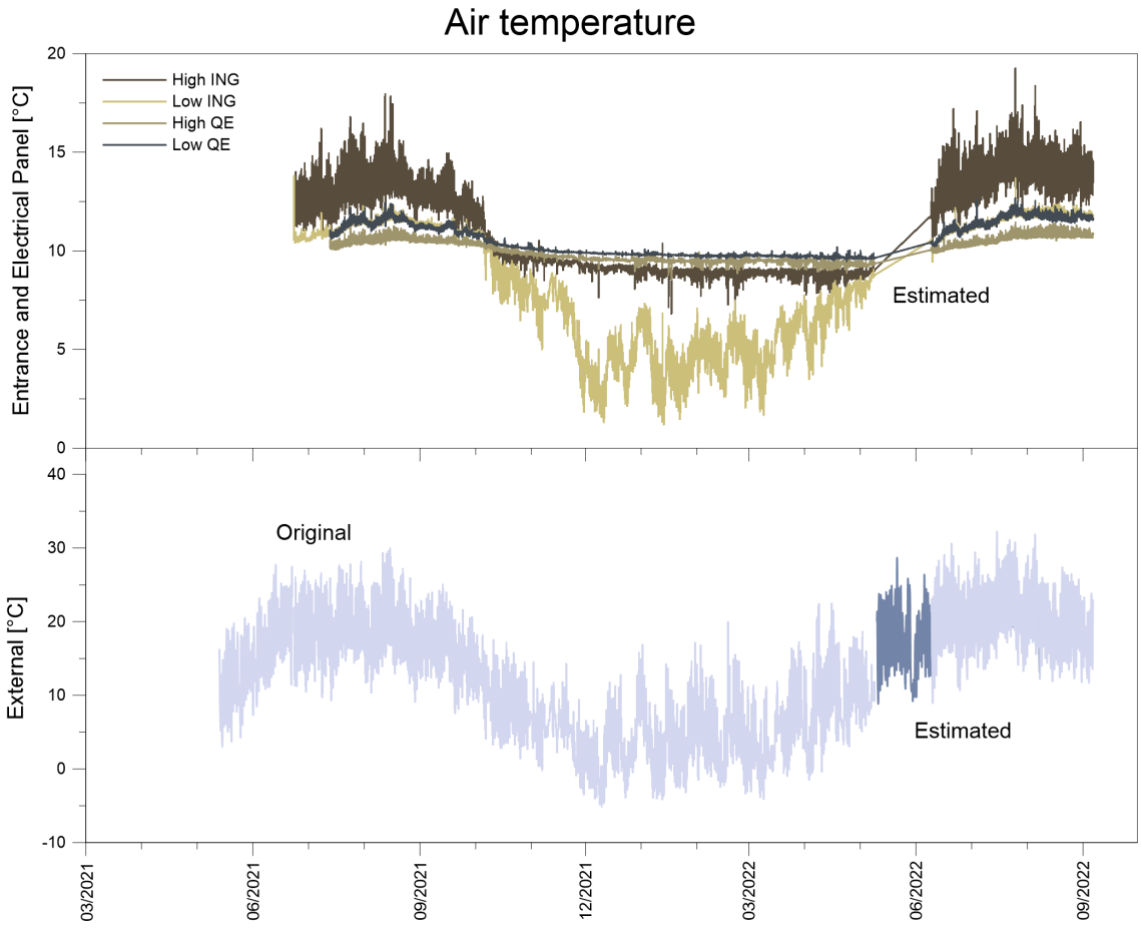

Figure 5.5 Air temperature in the period 06/2021-09/2021 at the Entrance and Electrical panel sites

In summer, on the other hand, large signal amplitudes are concentrated on the upper part of the cross section of the cave (ING High), representing the air entering the cave. The lower part remains quite homogeneous, being the air exiting the cave in thermal equilibrium with it. The process is shown in Figure 5.3.f.

The outgoing air temperatures, in summer at the "ING low" sensor, and in winter at the "ING high" sensor, have daily amplitudes in the order of 1-2°C.

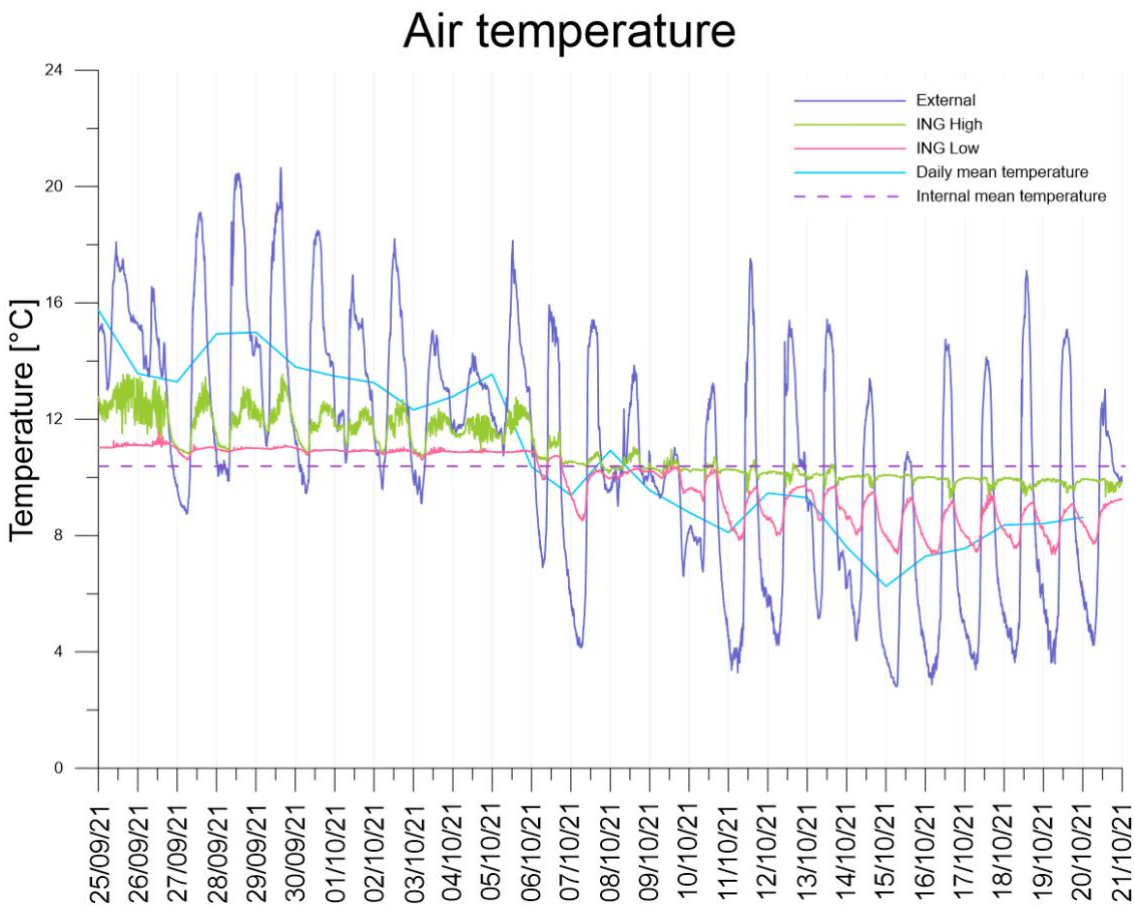

Figure 5.6 Air temperature in the shallow part of the cave

Considering, in particular, the period from 25/09/21 to 20/10/21 (Figure 5.6), it can be seen that the inversion occurs when the average daily temperature falls below the average indoor temperature equal to 10.39°C (calculated as the average of the temperatures at the top and bottom of the electrical panel during the whole set of data, 06/2021-09/2022). The sensor at the top of the entrance continues to have higher temperatures than the one at the bottom, and yet from 07/10/2021, they remain fairly constant, while the one at the bottom of the section begins to be strongly affected by daily variations.

Unfortunately, due to instrumental issues, it is impossible to observe the transition that occurs between 09/05/22 and 09/06/2022.

There are 5 sensors distributed between the entrance and the corridor:

- 2 sensors (one at 1 m and one at 50 cm) outside the cave above the entrance door; these two sensors are exposed to solar radiation (Called 'EXT' in the diagram);
- 2 sensors (one at 1 m and one at 50 cm) just inside the cave, in an area that is sheltered from the sun but very shallow (Called 'ING' in the diagram);
- 1 sensor about 5 m from the entrance (called 'Acquirer 50 cm' in the diagram);

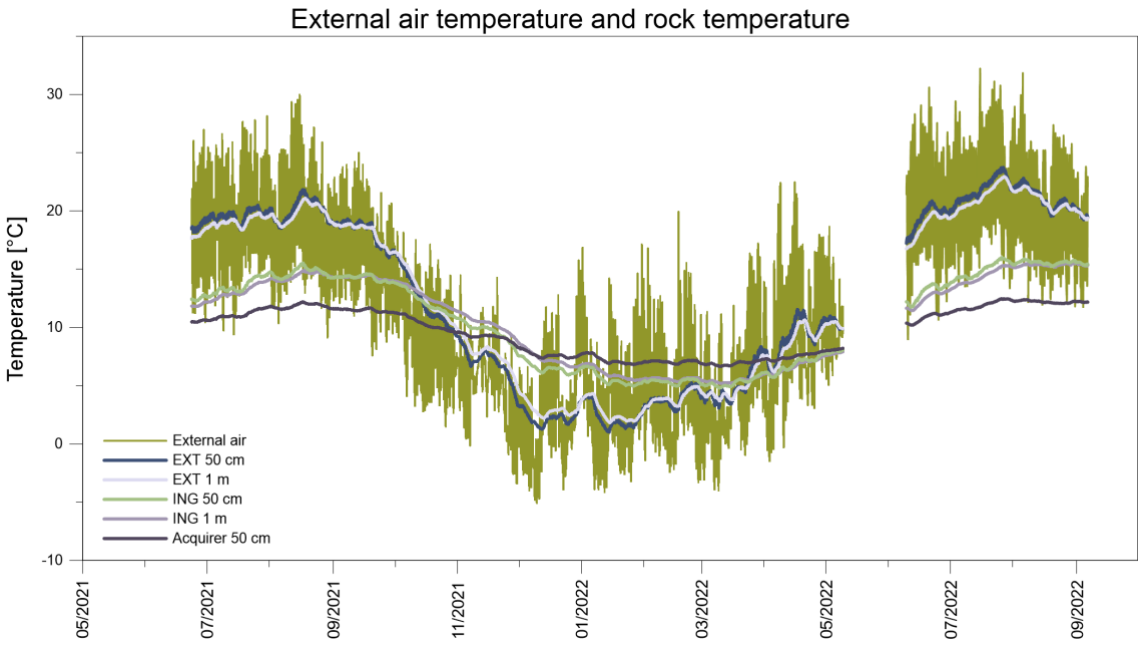

Figure 5.7 Comparison between rock and external temperature

As expected, the sensors most affected by solar radiation are those exposed to the sun outside the cave. They follow the trend of the outside temperature. Since the rock has higher thermal inertia, the rock sensors perceive seasonal changes and temperature peaks later. The two sensors at the inlet and the one at the acquirer show a trend that is even less influenced by seasonal trends.

The annual averages of each sensor are shown in Table 5.2. They are calculated over the period 23/06/21-23/06/22 but in the absence of data over the period 09/05/22-09/06/22.

Table 5.2 Annual averages, maximum and minimum values for rock temperatures

	EXT 1 m	EXT 50 cm	ING 1 m	ING 50 cm	Aquirer 50 cm
Max [°C]	22.94	23.74	15.54	16.00	12.47
Min [°C]	1.82	1.01	5.19	4.78	6.65
Delta [°C]	21.13	22.73	10.35	11.22	5.82
Avg (06/21-06/22) [°C]	10.78	10.73	9.76	9.64	9.14
Avg (09/21-09/22) [°C]	10.99	10.93	9.95	9.82	9.24

Rock temperatures show a similar inversion pattern to that seen for air temperature. In summer, the temperature gradient is directed towards the core of the rock, and in winter towards the outside (see Figure 5.7). This behaviour also applies to the two sensors at the entrance.

Porfiroidi

Porfiroidi is the first site one encounter walking along the tourist path (Figure 4.2). There are five air temperature sensors there: one (called "Stream" in the data) near the Mora River, below some ceiling collapses, one just above them ("Low Air"), one about three meters higher, just below the tourist trail ("Medium Air"). The photo of the latter two is shown in Figure 4.4. There are then two sensors above the tourist path: "High Air" and "Very High Air."

One of the sensors shows very different behaviour from the others due to its peculiar location near the stream (Figure 5.8). Because of the high humidity and low temperature, it is assumed that due to condensation the sensor does not measure the actual air temperature but the temperature of the dew point (very similar to the one of the stream).

Table 5.3 Air temperature at Porfiroidi

	Low Air	Medium Air	High Air	V. High Air	Stream Air
Max [°C]	8.98	8.80	9.12	8.90	7.68
Min [°C]	8.21	8.33	8.43	8.47	7.16
Delta [°C]	0.77	0.47	0.69	0.43	0.52

Avg (06/21-06/22) [°C]	8.33	8.41	8.52	8.56	7.51
Avg (09/21-09/22) [°C]	8.34	8.42	8.53	8.56	7.53

The other four sensors, on the other hand, show parallel trends, with temperature changes between 0.77°C and 0.43°C. Temperatures rise with the increasing of altitude.

The four data sets do not show any kind of inversion as in the case of the entrance site. However, strong peaks are seen during summer periods and every week: this is the effect of tourist presence that will be discussed in the next chapter.

Flood events (the one due to snowmelt between March and late May 2022 and that from autumn rains in November 2021) cause a visible decrease in temperatures even at the highest sensors, although it is less and less obvious as the distance from the main collector increases (Figure 5.8, Air temperature).

The annual average temperatures for both rock and air are shown in Table 5.4. It is interesting to note that annual averages change slightly, depending on the period used to calculate it. This fact is particularly true for air, which has a lower thermal inertia than rock. The summer of 2022 was particularly hot. As far as rock temperatures are concerned (Table 5.4), they are rather constant compared to the more superficial ones. At Porfiroidi, four sensors are found at different depths (5 cm, 50 cm, 1 m and 3 m). Temperatures decrease with increasing depth showing no inversion during the year (Figure 5.8).

The air temperature is intermediate between the one of water and of rock.

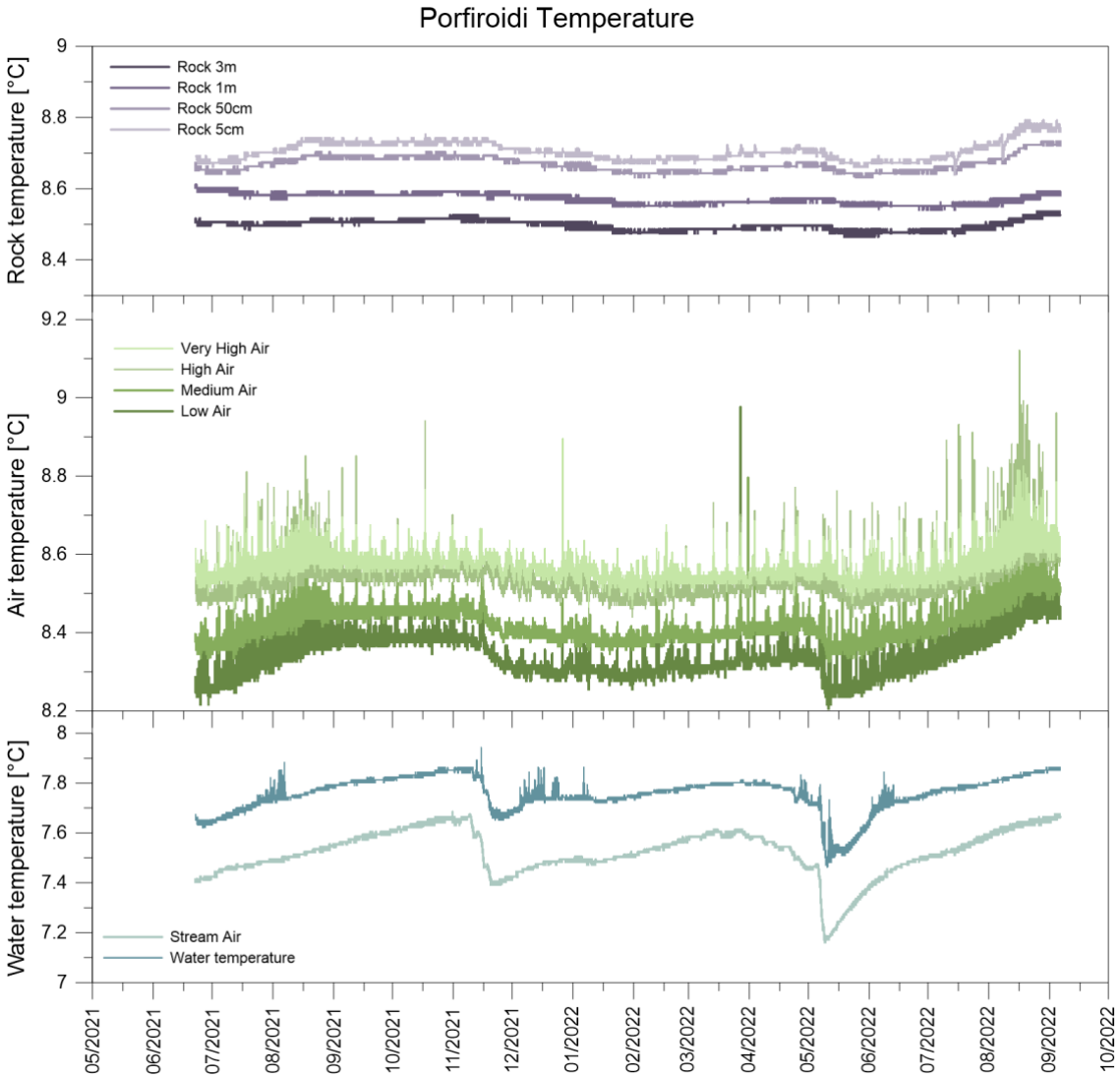

Figure 5.8 Porfiroidi air and water temperature

Table 5.4 Air and rock temperatures at Porfiroidi

	Max [°C]	Min [°C]	Delta [°C]	Avg [°C] (06/21-06/22)	Avg [°C] (09/21-09/22)
Low Air	8.98	8.21	0.77	8.33	8.34
Medium Air	8.8	8.33	0.47	8.41	8.42
High Air	9.12	8.43	0.69	8.52	8.53
V. High Air	8.9	8.47	0.43	8.56	8.56

Stream Air	7.68	7.16	0.52	7.51	7.53
Rock 3m	8.54	8.47	0.07	8.5	8.5
Rock 1m	8.61	8.54	0.07	8.57	8.57
Rock 50cm	8.73	8.63	0.1	8.67	8.67
Rock 5cm	8.95	8.64	0.31	8.7	8.71

Sacrestia

Because of Sacrestia's sheltered location, it will not be considered in the determination of airflow dynamics. It is, however, of particular interest for rock temperatures. As shown in Figure 5.9, the temperatures of the three media are very different from the rest of the cave.

Six probes are found in the Sacrestia site:

- 2 rock thermometers.
- 1 air thermometer.
- 1 water thermometer of the drip, coupled with a rock thermometer near the drip.

First of all, the rock shows an almost perfect sinusoidal pattern. The maximum outside temperature (in august 2021) seems to be dampened and evened out, with about five months delay (arriving in January 2022). The thermal wave penetrating from outside through the rock to Sacrestia surface is clearly visible. This is because, due to a particular morphology of the surface of the slope outside the cave, Sacrestia is the closest point to the surface in terms of overlying rock thicknesses. The amplitude of the sine wave for the rock at 50 cm is 0.69°C, the period is 166 days like for the other probes.

The water temperature represents the water temperature of one of the secondary veins, which is dry for most of the year.

The air temperature are clearly influenced by rock temperatures. The almost instantaneous but also very intense peaks constitute the passages of the laboratory users, which have big influence in such a small and protected environment.

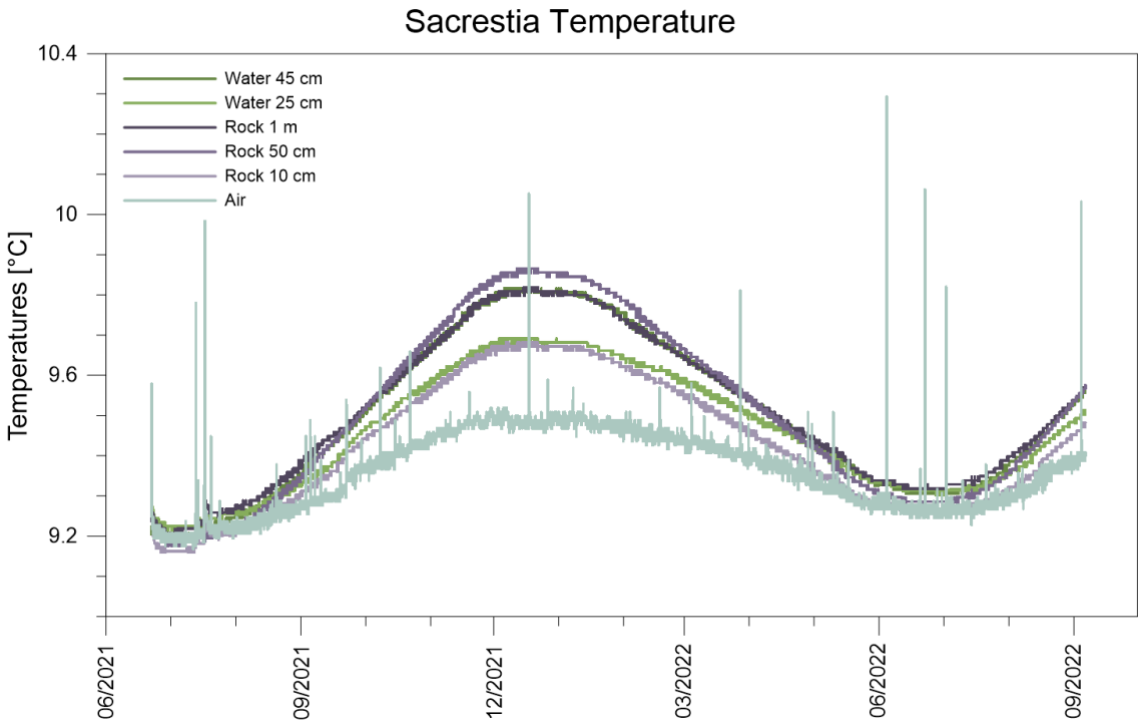

Figure 5.9 Sacrestia air, rock and water temperature

Table 5.5 shows the annual maximum, minimum and average values (for the period June 2021-June 2022 and September 2021-September 2022).

Table 5.5 Average, maximum and minimum temperature values at Sacrestia. All data in °C.

	Air	Water 45 cm	Water 25 cm	Rock 10 cm	Rock 50 cm	Rock 1 m
Max	10.37	9.82	9.69	9.69	9.87	9.82
Min	9.17	9.20	9.21	9.16	9.18	9.21
Delta	1.21	0.62	0.48	0.53	0.69	0.61
Avg (June)	9.37	9.52	9.48	9.44	9.53	9.53
Avg (Sept)	9.38	9.55	9.50	9.47	9.56	9.56

Milano

Milano is located just before the bottleneck between the two main halls (section in Figure 3.3). There are four temperature sensors there: Low Air, Anemometer Air, Rock Block Air, High Air (CAI Pole). Temperature trends are very similar to those shown at Porfiroidi even during flood events, but temperatures are higher on average (Table 5.6). The peaks occur weekly (on Sundays) and correspond to the days of highest tourist attendance, as mentioned above for Porfiroidi.

Table 5.6 Milano air temperature

	Max [°C]	**Min [°C]**	**Delta [°C]**	**Average (06/21-06/22) [°C]**	**Average (09/21-09/22) [°C]**
Low Air	8.53	8.18	0.35	8.39	8.42
Anemometer Air	8.99	8.47	0.52	8.6	8.63
Rock Block Air	8.99	8.6	0.39	8.77	8.79
High (CAI) Air	9.24	8.73	0.51	8.83	8.84
Rock 50 cm	9.05	8.95	0.1	8.99	9
Rock 1 m	9.06	9	0.06	9.02	9.03

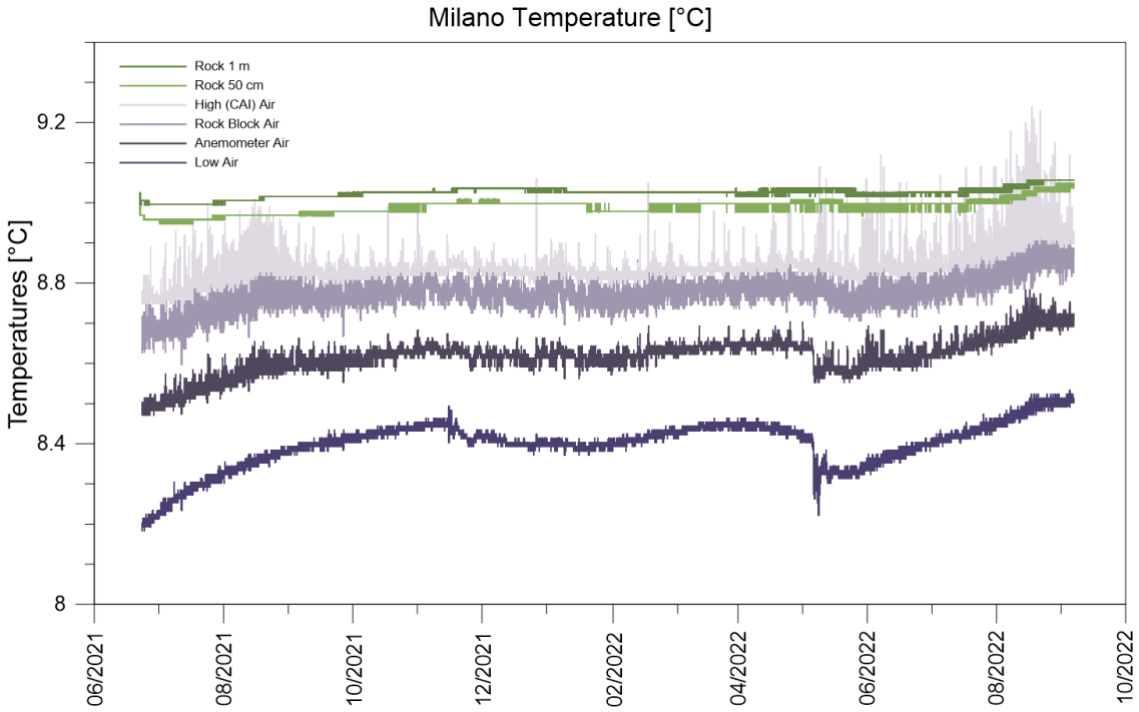

Figure 5.10 Milano air and rock temperature

As far as the temperature of the rock is concerned, it is the most constant measured in the cave. Table 5.6 shows the maximum, minimum and average annual values. They only seem to be slightly affected by the summer of 2022, which showed not only very high temperature, but also a large influx of tourists. As for the rest of the cave, the rock is warmer overall than the air. The direction of the heat remains constant and directed towards the cave.

In contrast to the Porfiroidi site, where temperature probes are located within boreholes in fractured metavolcanic rocks and are therefore more sensitive to changes in external air temperature trends, the rock temperature data exhibits a comparatively stable pattern. This is due to the fact that the temperature probes in the rock are placed within dense carbonate rocks.

Fondo

As for the Fondo station, there are two air temperature probes (Figure 5.11): High Air and Low Air, near the water. Fondo site is located in the flattest part of the cave, upstream

of Lake Ernestina, consisting of a canyon of modest cross section. In this area the air, which is not agitated by turbulence from the stream flowing at the base of the canyon, is very stratified. Unfortunately, however, it is not possible to provide an accurate analysis since much of the data for this station is missing.

Since it is not a tourist area, the air temperature peaks are caused by the passage of cavers.

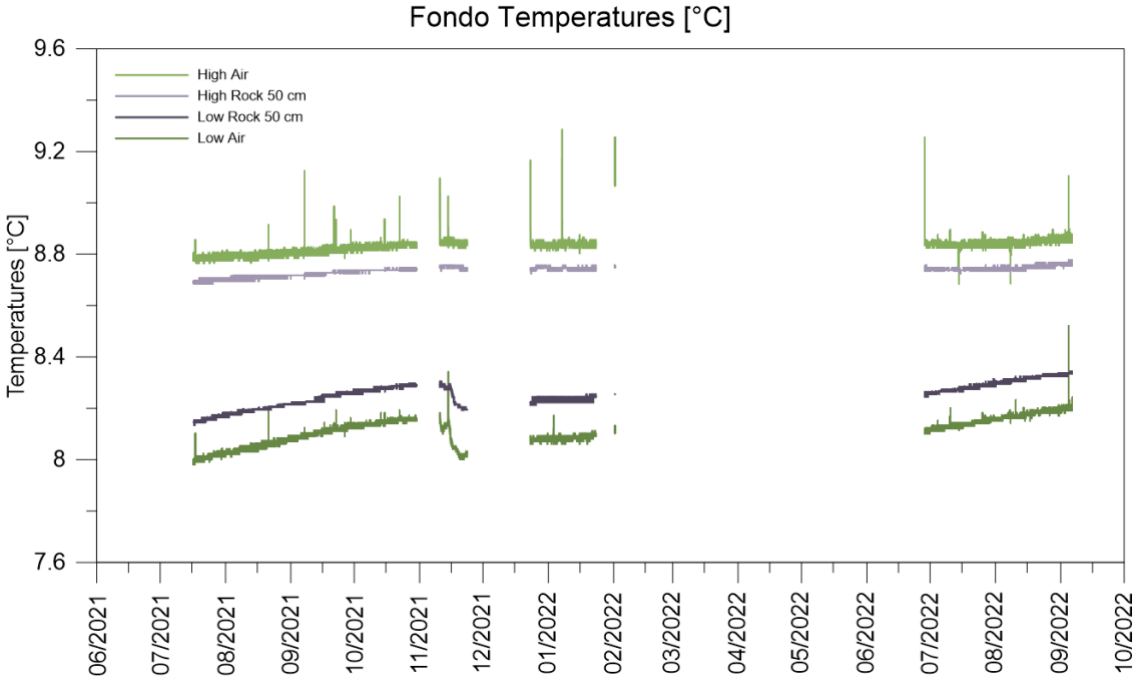

Figure 5.11 Fondo temperature

Regarding rock temperatures, they fall between the two air temperature levels and are measured using probes that are placed at a depth of 50 cm. It should be noted that the low air temperature probe measures the temperature of the sensor itself due to condensation, rather than the actual air temperature. Since this sensor is spatially close to the collector, which is also in proximity to the rock, the rock temperature is significantly influenced by it, but still remains relatively higher. Conversely, in the upper section of the cross-section, temperatures tend to be notably higher due to the stratification occurring in the canyon. Notably different from the rest of the cave, rock temperatures in this area are lower than air temperatures. Table 5.7 presents the annual maximum, minimum, and average values for these temperature readings.

Table 5.7 Fondo rock temperature

	Low Air	High Air	Low Rock 50 cm	High Rock 50 cm
Max [°C]	8.52	9.29	8.34	8.78
Min [°C]	7.98	8.69	8.13	8.69
Delta [°C]	0.54	0.60	0.21	0.09
Average [°C]	8.11	8.83	8.25	8.73

5.3 Anemometer data

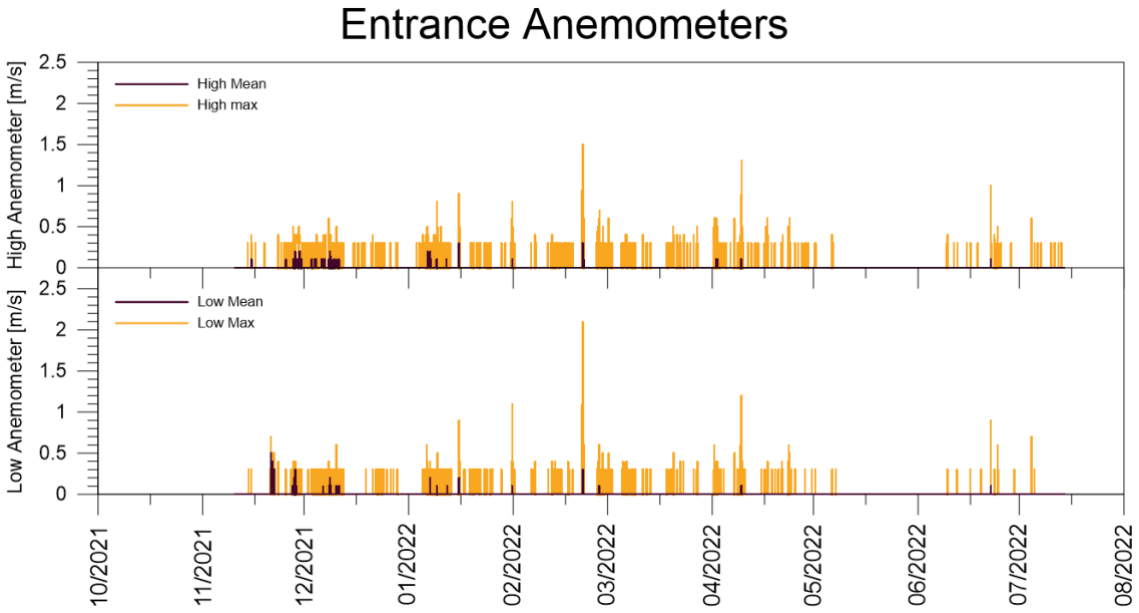

Figure 5.12 Anemometer data at the top and bottom of the entrance

To define the circulation pattern more precisely in the cave, it would be useful to quantitatively define the magnitude of air flows. For this reason, data obtained from the anemometers (which are located at the entrance in the upper part of the section, in the lower part and in the bottleneck between one hall and the other, also in the upper and lower part) could have been useful. However, the ultrasonic anemometers installed in the cave have a sensitivity of 0.3 m/s, which, being slightly higher than the air speed of the cave, measures only at a few times of the year as shown in Figure 5.12.

This type of ultrasonic anemometer returns two types of values every 10 minutes:

- The maximum value recorded in 10 minutes.
- The average of the values recorded in 10 minutes.

5.4 Field tests

Thus, other types of air circulation tests were carried out. During the inspection on September 26, lit incense sticks were used to determine the flow direction. By placing them at different points in the corridor section they gave different responses. In order to analyze the results, it is important to assess that late September/early October is precisely the period during which the inversion between upper and lower incoming flow occurs. During the execution of the test (at 3:30 p.m. on 26/09/22), the outdoor temperature was 20°C.

The smoke from the incense sticks indicated a primarily outward flow in the lower region of the cave, at both the entrance (where two anemometers are located) and electrical panel sites. Conversely, the upper part of the cave exhibited mainly inward flow. Nonetheless, there were brief intervals, lasting roughly ten seconds, where the flow in both upper and lower sections was entirely outgoing or incoming.

Incense was not used in the main halls because of the size of the section and thus the lower air velocities. However, at the height of the bottleneck where the anemometers are installed, a downward flow of air is easily felt on the skin in the lower part of the section where the tourist passage is placed.

In addition, during the inspection on 21/01/23, wind speed measurements were taken at various points with a hand-held hot-wire anemometer, and they are shown in Table 5.8.

The velocities taken near the floor (threshold Low and Low anemometer) are very similar to each other. The highest is the one taken at the ultrasonic anemometer at the top. This fact could be due to a narrowing of the section made with plexiglass in order to channel air to the anemometer. It is not possible to make the same thing on the floor as it would impede the passage of tourists. As expected, the lowest velocity in this region is observed

in the middle of the threshold, where outgoing and incoming flows intersect. In contrast, the velocity measurements in Milan are lower, likely due to the considerably larger section.

Table 5.8 Manual air velocity measurements made with a hand-held hot-wire anemometer

Wind speed		**[m/s]**
Threshold	High	0.34
	Low	0.22
	In the middle	0.06
Low anemometer		0.24
High anemometer Milano		0.19

5.5 Correlation of Wind Gusts, Pressure, and Temperature in the Corridor

The atmospheric air is constantly moving but, except for special conditions, usually does not exceed 50 km/h (Lismonde, 2002). As expected, wind speed increases as it moves away from the earth's surface and generally shows a small vertical component. At the entrance of cavities, wind (and particularly gusts) plays an important role. Particularly in the case of single-entry caves, wind gusts can cause overpressures or under pressures that tend to equalize at the end of the wind gust phenomenon (Lismonde, 2002).

This type of behavior would explain the unifying of the direction of the air current in one direction (i.e., an outflow in each portion of the cross-section) for a few moments during the incense test. In order to verify the influence of external wind on the corridor air currents, data from the anemometer located outside at the same altitude and about ten meters from the entrance were analyzed. This anemometer, being a “cup anemometer” type, does not give directional indications, but still gives average and maximum values every ten minutes as with the ultrasonic anemometer (Figure 5.13).

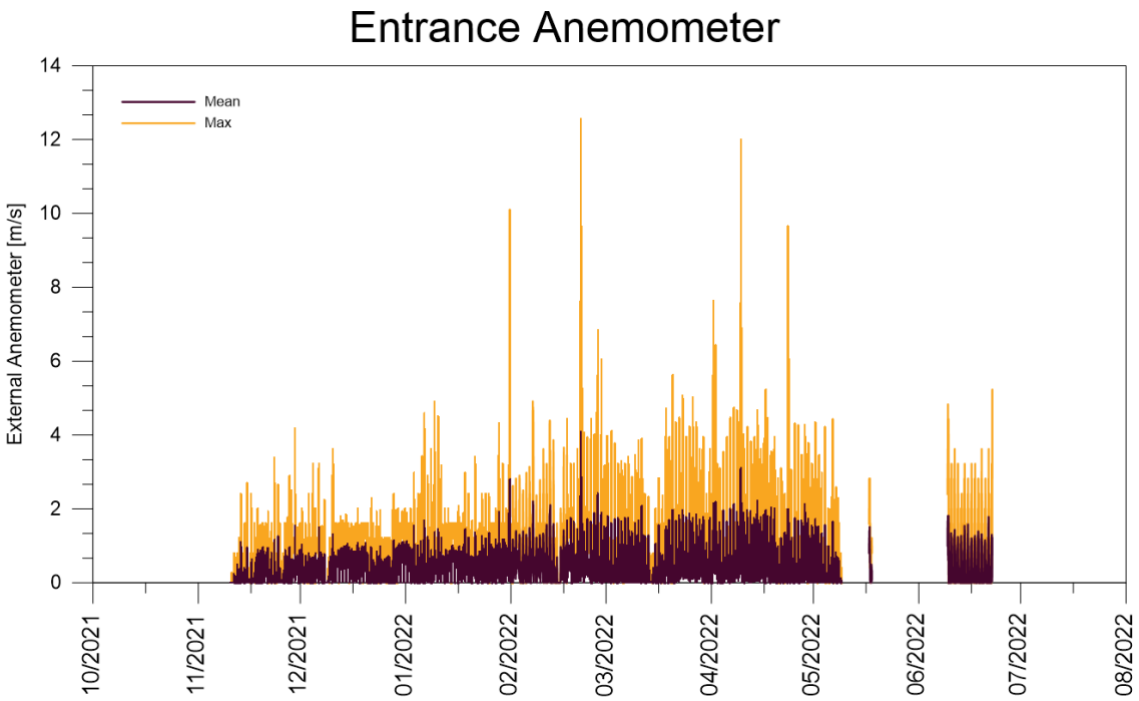

Figure 5.13 External cup anemometer

The three most significant wind gust events were analyzed in detail:

- 31/01/22, in which the external anemometer recorded a wind speed of 10.10 m/s Figure 5.15;
- 21/02/22, in which the external anemometer recorded a wind speed of 12.55 m/s (Figure 5.14)
- 09/04/22, in which the external anemometer records a wind speed of 11.99 m/s (Figure 5.16);

These events represent the times when the anemometers placed at the entrance showed the most noticeable responses, showing how gusts affect at least the first tens of meters of the cave. Excluding intense wind events outside, there are very few cases where anemometers report a wind speed greater than 0.3 m/s without a wind speed of at least 0.64 m/s being reported outside.

They are compared with the values of external pressure and pressure measured at Milan.

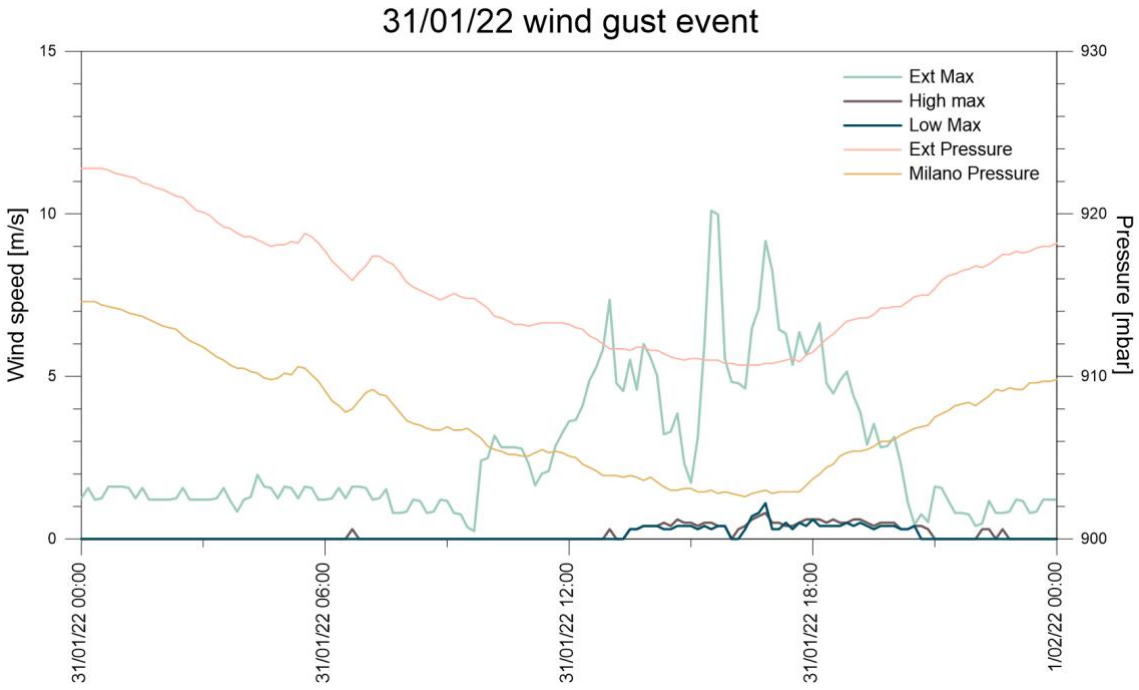

Figure 5.14 31/01/22 Wind gust event and pressure data

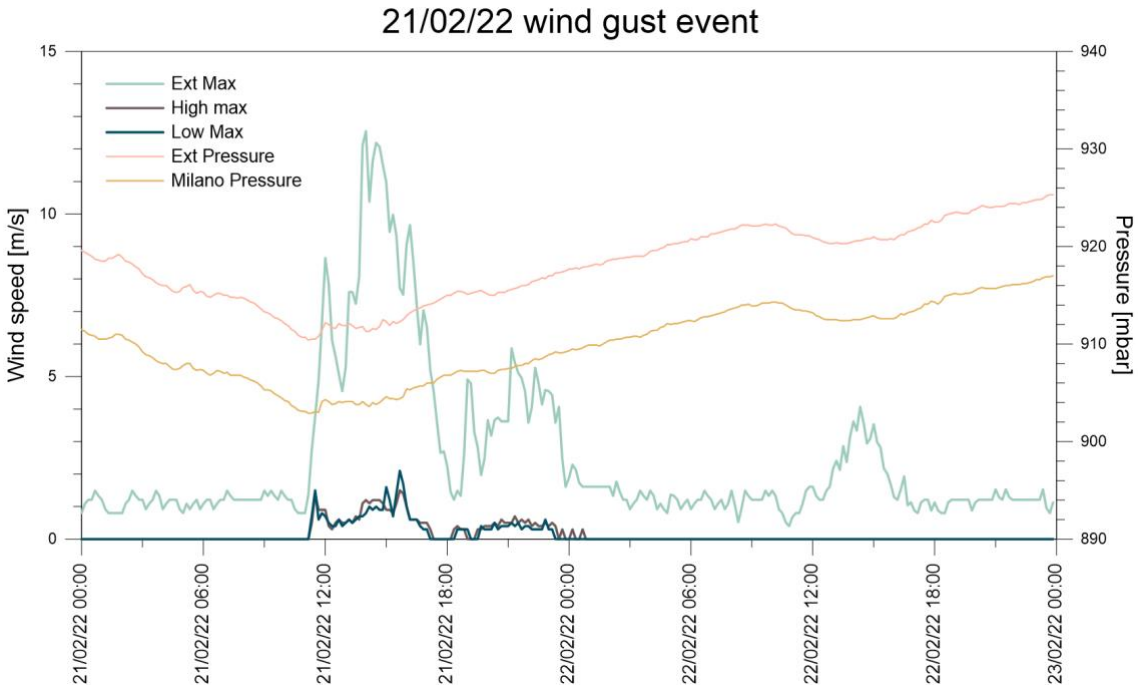

Figure 5.15 21/02/22 Wind gust event and pressure data

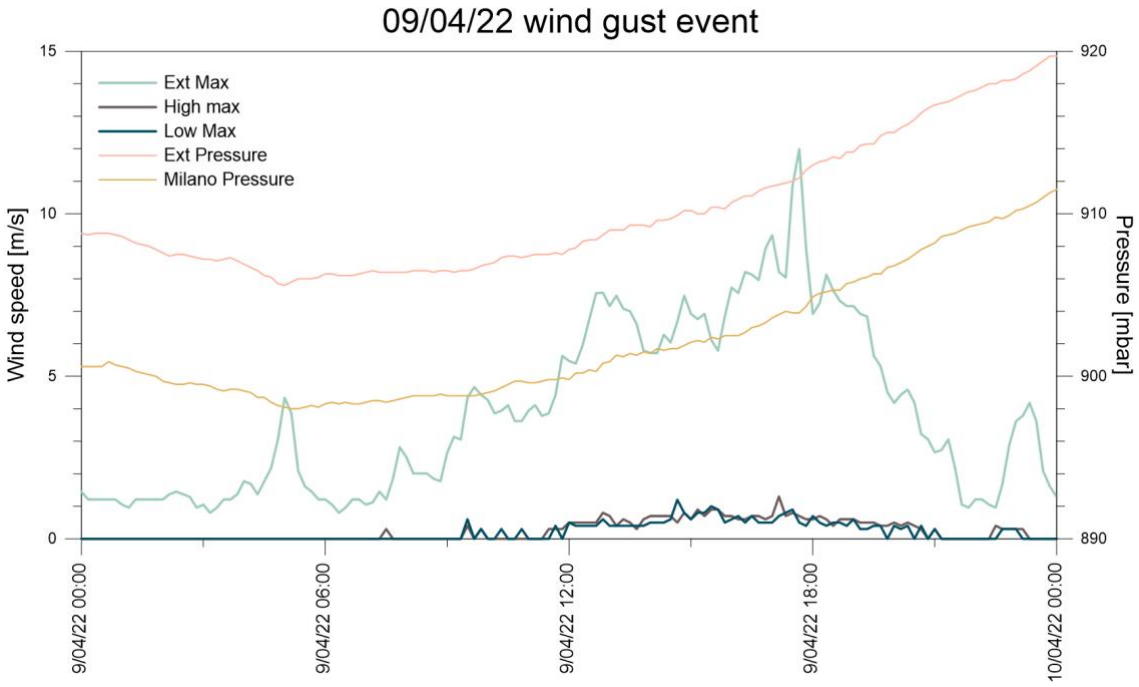

Figure 5.16 09/04/22 Wind gust event and pressure data

To evaluate the potential impact of wind gusts on pressures, Figure 5.17 presents an overview of the calculated pressures at Bossea. Delta, which represents the difference between the two pressures, remains relatively constant at approximately 8.1 mbar. The standard deviation for this measurement is 0.22 mbar. Based on the external pressures calculated using the barometric formula, the internal pressures at the Milano and Fondo sites are also determined.

$$P = P_0 \exp\left(-\frac{g \cdot m \cdot \Delta z}{R\, T_b}\right)$$

Where:

- P_0 = reference pressure, in this case the external one [mbar].
- g = gravitational acceleration: 9.81 m/s^2;
- m = molar mass of Earth's air: 0.0289644 kg/mol;
- Δz = Altitude difference between external pressure measure and Milano and Fondo, respectively taken as 50 m and 110 m.
- R = universal gas constant: 8.3144598 J/(mol·K)

- T_b = external temperature (K)

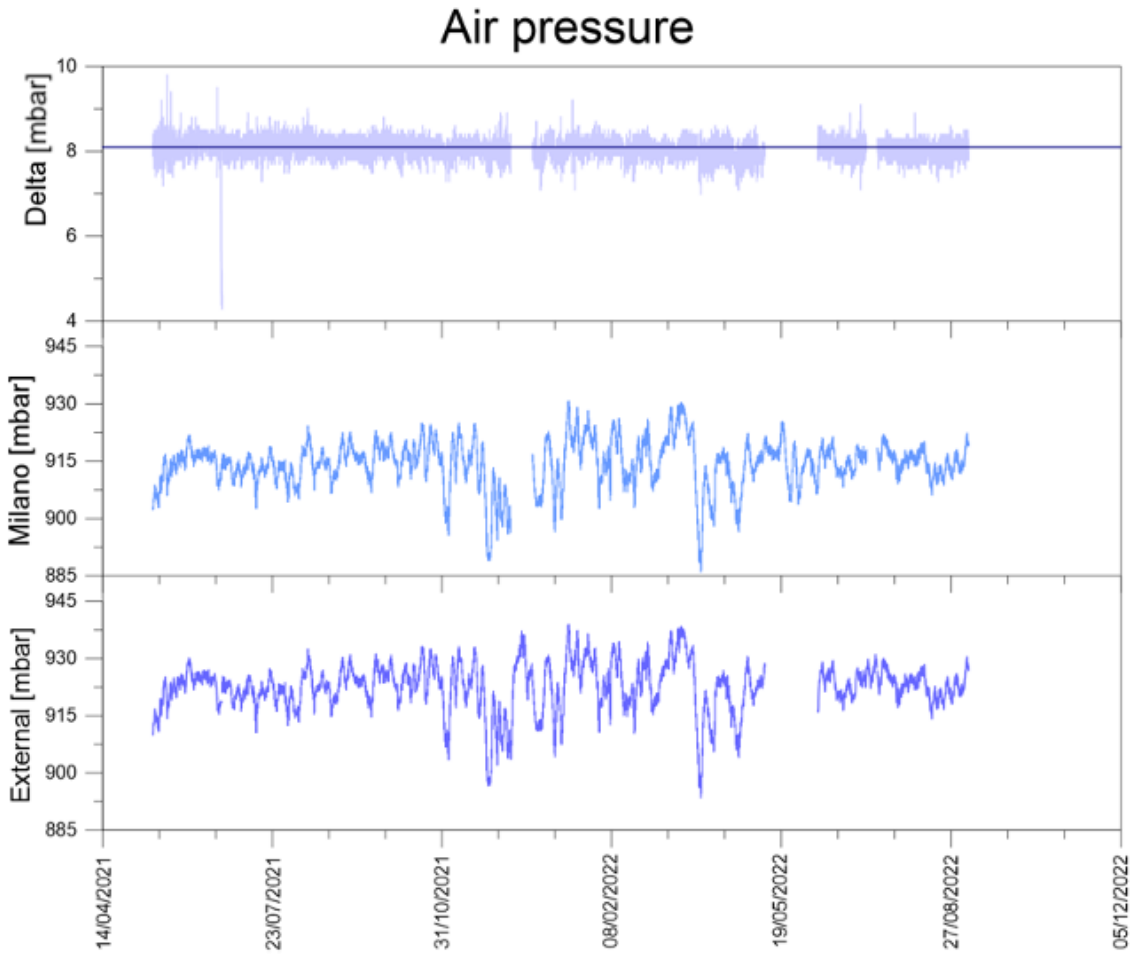

Figure 5.17 Pressure data mesured at the external and Milano probes. Delta is the difference between the two.

To evaluate the accuracy of the pressure data, a comparison was conducted between the calculated pressure values and the actual measurements obtained in Milano and Fondo. The difference between the two values was used as the basis of comparison, resulting in a delta range of 1.3 to 4.3 mbar for Milano and 1.6 to 8.4 mbar for Fondo. The variation between the measured and calculated values is largely attributed to the presence of air movements caused by convective cells that were not taken into account in the barometric equation.

Another comparison was made between the external wind speed and the temperatures of the shallowest areas of the cave (as input parameters ING Low and ING High). The gusts

of wind occurrence analyzed is the one of 21/04/2022. As shown in Figure 5.18, as soon as the air increases in velocity, the temperature at the top (High ING) decreases, the temperature at the bottom increases (Low ING), and together they reach the same value. Due to the cupped design of the outdoor anemometer, there is no directional data available. As a result, the average temperature values for the twelve hours preceding the event were examined for both the outdoor and cave temperatures (excluding E.Q.). It can be observed that both Low ING and High ING reach the same level as the average outdoor temperature, suggesting that the wind is likely blowing in the direction of the cave's interior. This same trend can also be observed for the 24/04 event (Figure 5.19). Not as obvious but still present, the same effect can be seen for the 31/01/2022 event (Figure 5.20)

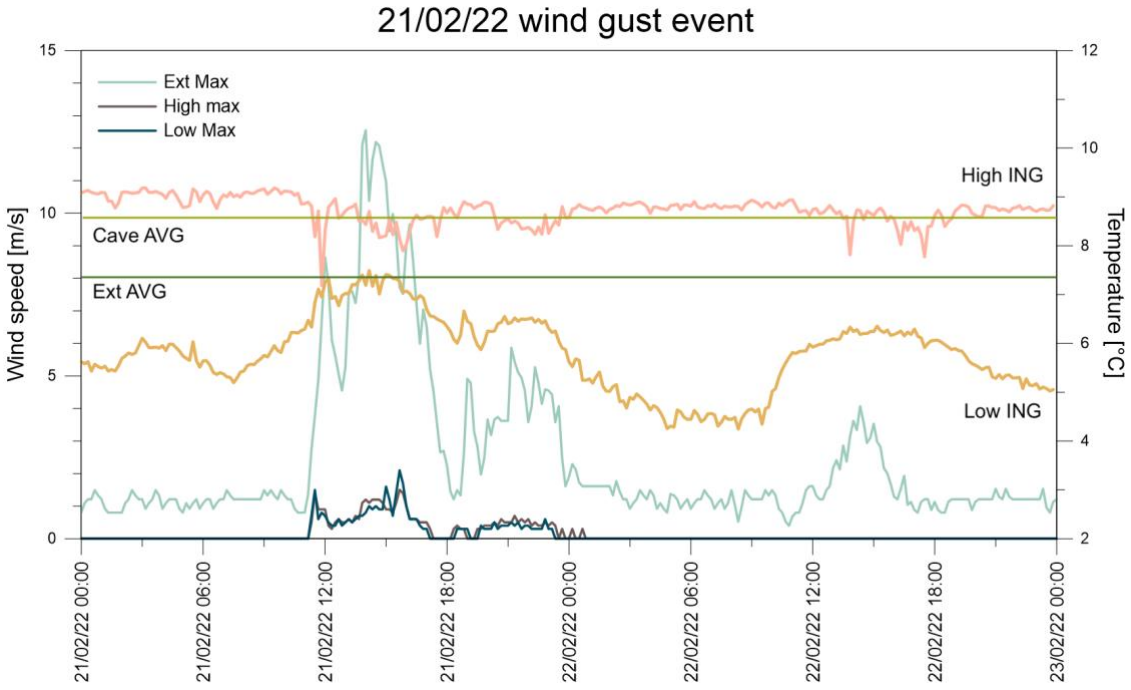

Figure 5.18 21/02/22 Wind gust event compared with the shallowest temperatures

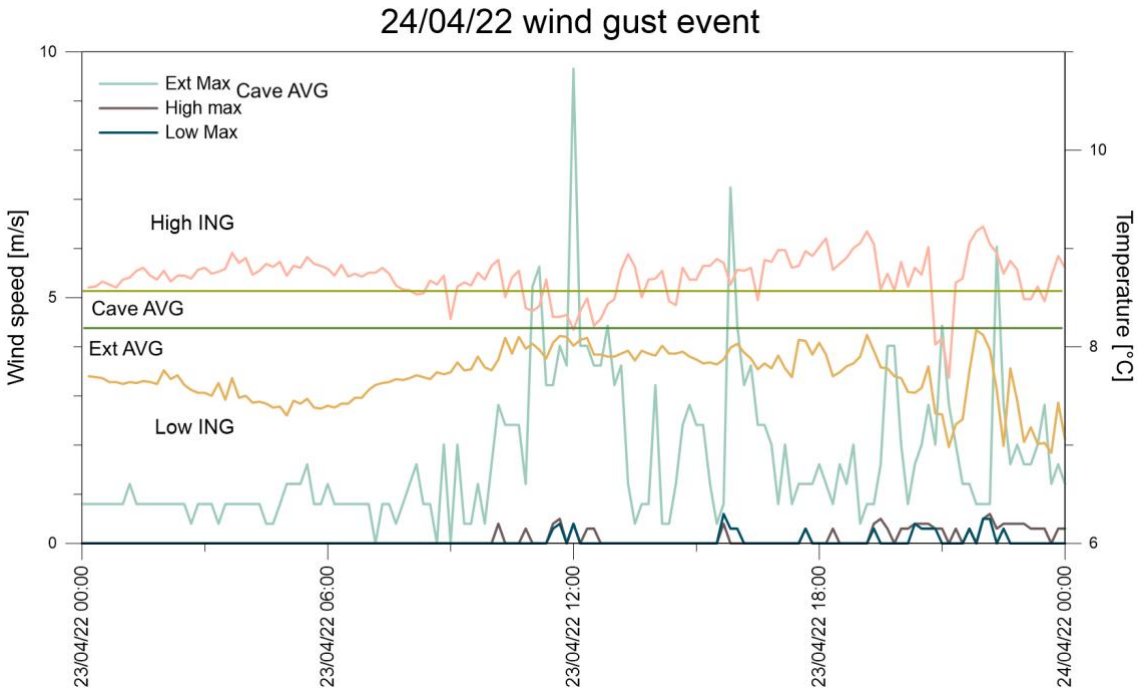

Figure 5.19 24/04/22 Wind gust event compared with the shallowest temperatures

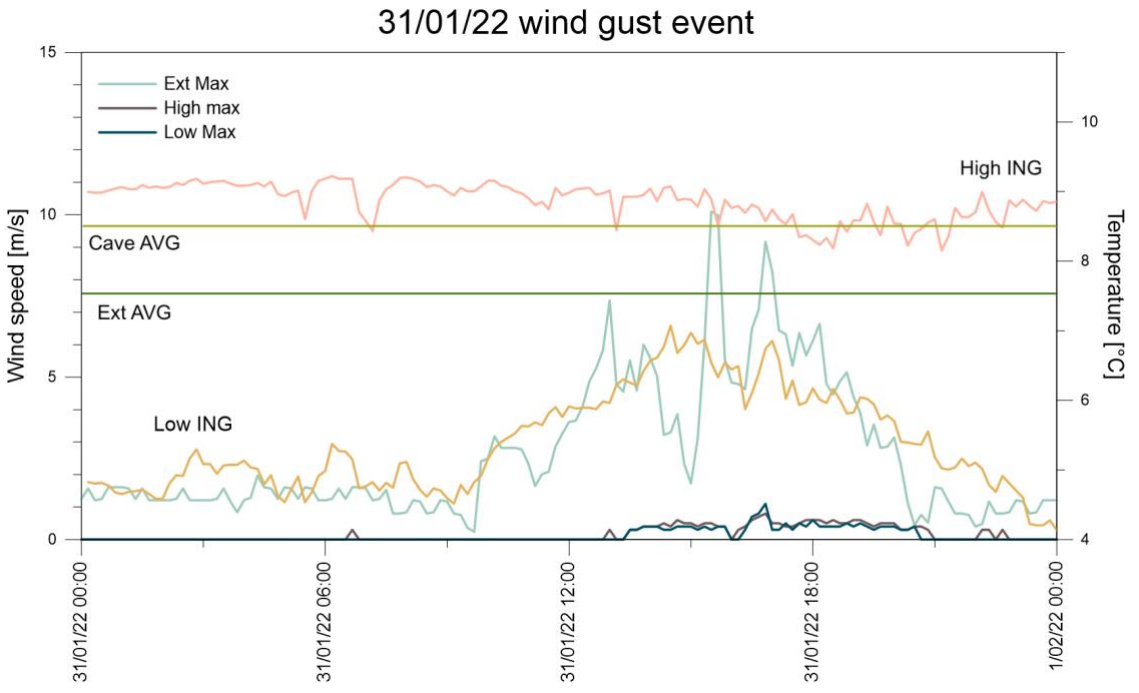

Figure 5.20 31/01/22 Wind gust event compared with the shallowest temperatures

5.6 Cave airflow assessment

Given the above considerations, a box plot was generated to depict the internal temperatures of the cave. This type of plot is particularly useful as it provides a single indicator to visualize the center and distribution of a dataset. Also known as a whisker diagram, it comprises the following main elements:

- The center line of the box represents the median of the data, where half of the values are above and half below. If the data are symmetrical, the median is located in the center of the box. However, if the data are asymmetrical, the median will be closer to the top or bottom of the box.
- The top and bottom of the box show the 25th and 75th quartiles. The difference between these values is referred to as the IQR (interquartile range).
- The "whiskers" extending from the box represent the expected variation in the data and extend 1.5 times from the IQR from the top and bottom of the box. Any measurements outside the whiskers are considered outliers.

This type of representation enables the visualization of the entirety of data in such a complex scenario. As the presence of the convective cell in the entrance corridor was established (chapter 5.2), the data between 06/09/21 and 06/09/22 was divided into two separate sets:

- The summer component, spanning from 06/09/21 to 06/10/21 and then from 09/05/22 to 06/09/21;
- The winter component ranging from 06/10/21 to 09/05/22.

Figure 5.5 displays one year's worth of data obtained by combining the two components, as described earlier. The choice of dates for the two components is based on the date of convective cell inversion, which is shown to occur around 06/10/21. 09/05/22 is chosen as the winter-summer inversion date as it is the last available data of the month, and the temperature trend in Figure 5.5 suggests that the inversion occurred during the period of missing data.

The data were sorted in a way that follows the path of a hypothetical single convective cell, entering from the top of the entrance and exiting from the bottom of the same entrance after traversing the entire cave, as shown in Figure 5.21. The results of the analysis are presented in Figure 5.22.

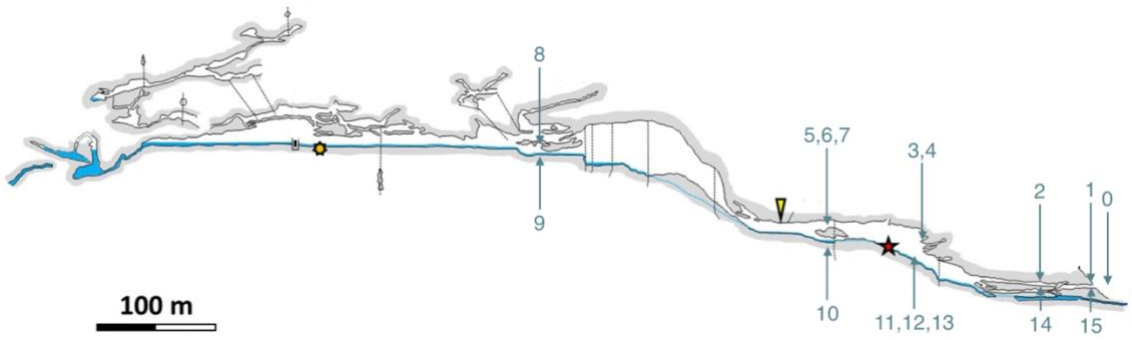

Figure 5.21 Points chosen for the box plot (Antonellini et al., 2019)

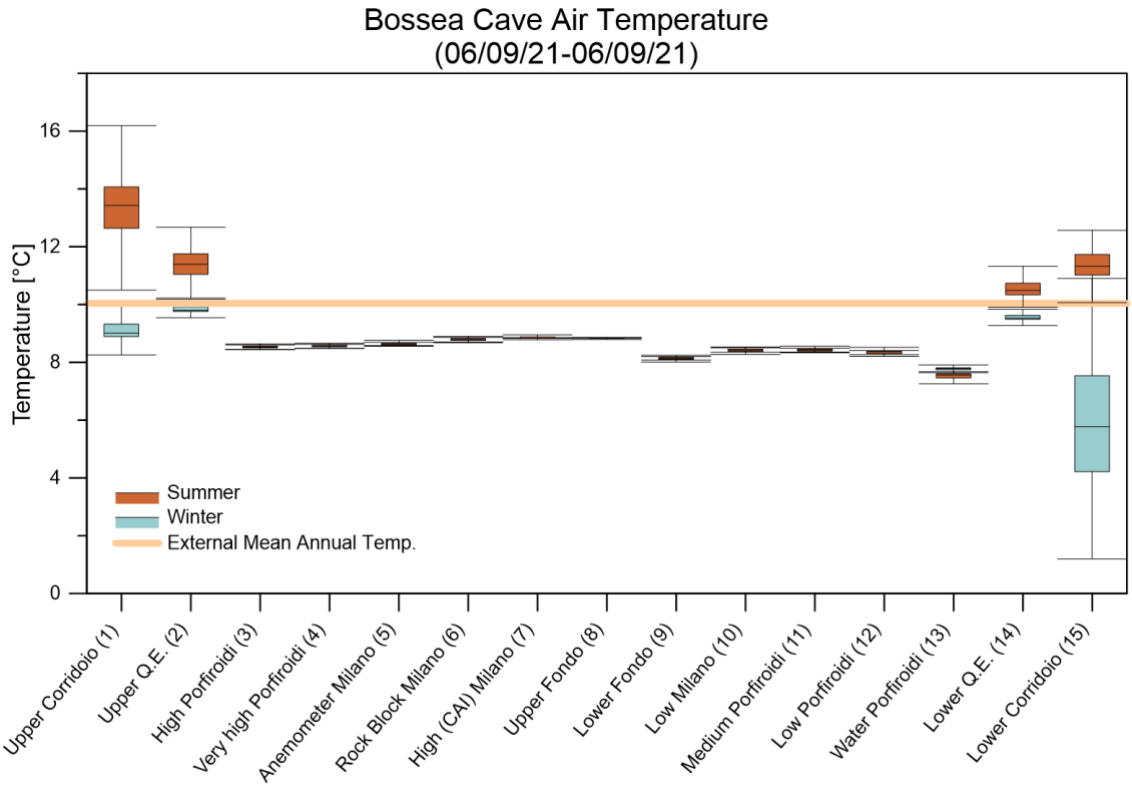

Figure 5.22 Overall view of cave temperatures

As previously discussed, the box plot provides a comprehensive overview of cave temperatures, both spatially and temporally. Figure 5.22 shows that sensors 1, 2, 14, and 15, located in the corridor, exhibit the greatest variability. These four sensors exhibit distinct behaviors between summer and winter, as previously demonstrated. During winter, the sensor located at the bottom of the entrance displays the widest temperature ranges, while the top sensor exhibits the same behavior during summer. The average annual outdoor temperature recorded during the specified period (10.03°C) falls between the summer and winter temperatures of the cave corridor.

In contrast, when examining the deeper parts of the cave, particularly the halls, the variability decreases considerably to the point where the boxes cannot be accurately seen. Figure 5.23 shows a zoomed-in view of only the inner probes.

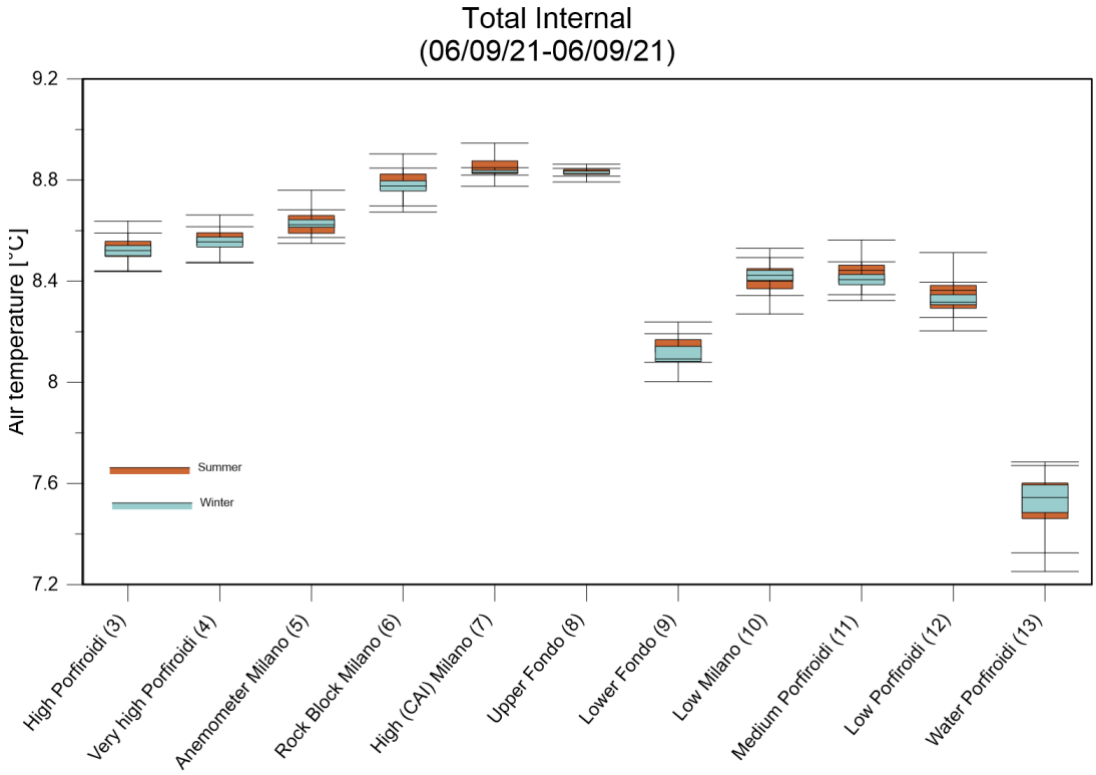

Figure 5.23 Overall view of deeper cave temperatures

As can be noted again, by comparing Figure 5.23 with Figure 5.21 for the location of the points, the temperature increases with increasing elevation in the halls as it travels along

the ceiling (points 3-8) until it reaches Fondo where it reverses the path. Lower Fondo is anomalously cold since, being very close to the stream, it suffers the effects of condensation. After Fondo (9), traveling this time along the bottom of the cave in a downstream direction, there are points 10-12 with temperatures very similar to each other and lower than those found at the points on the ceiling.

The increasing temperature between points 3 and 8 and decreasing (albeit less clearly) between points 10-12 could indicate the presence of a, though weak, convective cell. The cell would be weak since the temperature range of the cave is less than one degree and can therefore be considered rather uniform overall. Point 13 constitutes the stream water temperature at Porfiroidi. The variability of temperatures in the lower part of the cave (points 10-12) may be due to the unevenness of debris (due to the ceiling collapses) separating the Mora from the main hall rooms where most of the sensors are installed.

Another interesting observation is that the data variability between summer and winter is low in the halls, with mean and median values remaining almost the same for the same points. The temperature ranges also tend to be more compact during winter, indicating a low seasonal influence as early as entering the halls.

The temperature trends showed in Figure 5.22 and Figure 5.23 highlight once more the presence of two different convective cells:

- The first, in the corridor part, that seasonally shifts behaviour. This cells has a stronger power and reduce the exchanges that the second cell can have with the exterior.
- The second: a weaker convective cell (seen the homogeneity of the inside temperatures) that flows through the main halls and the Fondo site.

The summer and winter outline for the two cells are respectively showed in Ann. A and B.

6 Anthropic effects on temperature

As previously mentioned, Bossea is classified as a show cave, which means that it is accessible to visitors without requiring specialized equipment or clothing. Due to its easy accessibility, the cave receives a high volume of tourists, with 11,631 visitors in 2021 and 17,471 visitors in 2022. Consequently, the impact of tourism on temperature measurements cannot be overlooked.

This effect is especially evident on December 26, 2021, when a concert was held in the cave with approximately 80 attendees. The impact on temperature readings is clearly noticeable at the Porfiroidi and Milano stations, as illustrated in Figure 6.1. This event is particularly noteworthy as it is an isolated peak, with no significant influx of tourists in the days preceding the concert.

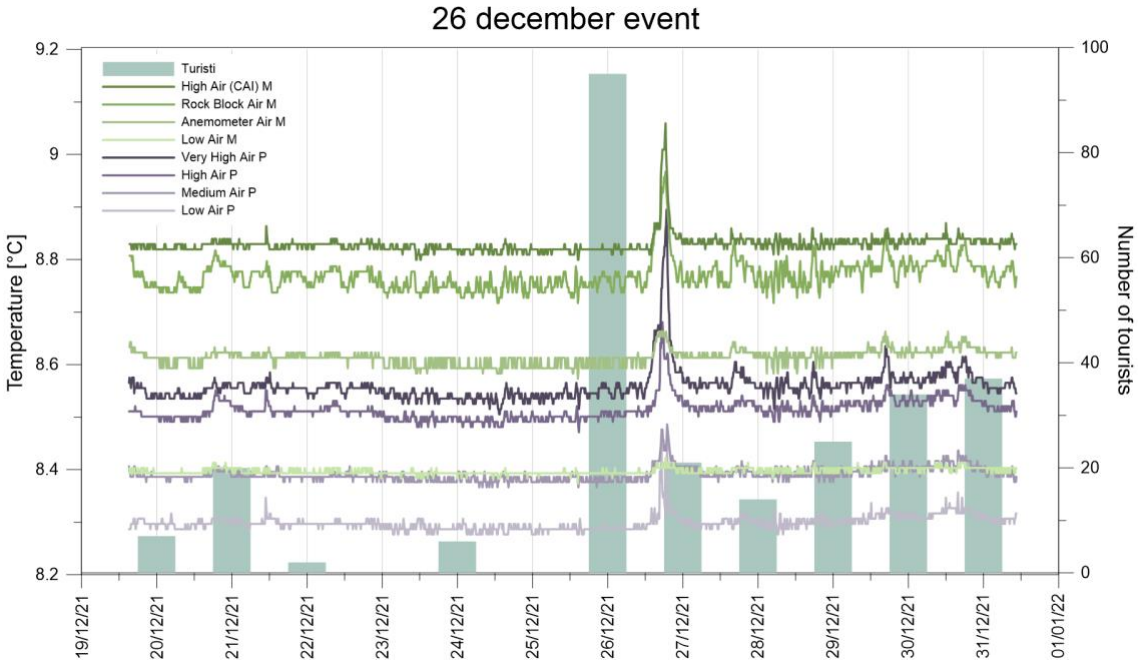

Figure 6.1 26 December music event

Upon analyzing the data from inside the cave (Porfiroidi and Milano, Figure 6.1), it is apparent that the expected influence of tourism is significant, particularly in the higher sensors. However, it is interesting to note that even the lower sensors, which are further away from the areas where people congregate, are also affected by the presence of tourists. It is worth noting the behavior of sensors in the entrance corridor (Figure 6.2), where the convective cell has a higher intensity. The temperature peaks resulting from the entrance and exit are evident in the shallowest sensor (Low ING), with small peaks observed in late afternoon on 26/12/2020. However, in the time interval between the two peaks, which lasts a few hours, the temperature resumes its normal trend and does not exhibit any long-term effects. In contrast, the upper sensor (High ING) shows only a negative peak, displaying an opposite behavior to that observed inside the cave. At the Electrical Panel site, peaks are visible but with a lower magnitude than inside the cave. Interestingly, the sensor on the floor at the Electrical Panel is affected the most bet.ween the two at Q.E. site, in contrast to the sensors placed inside the cave

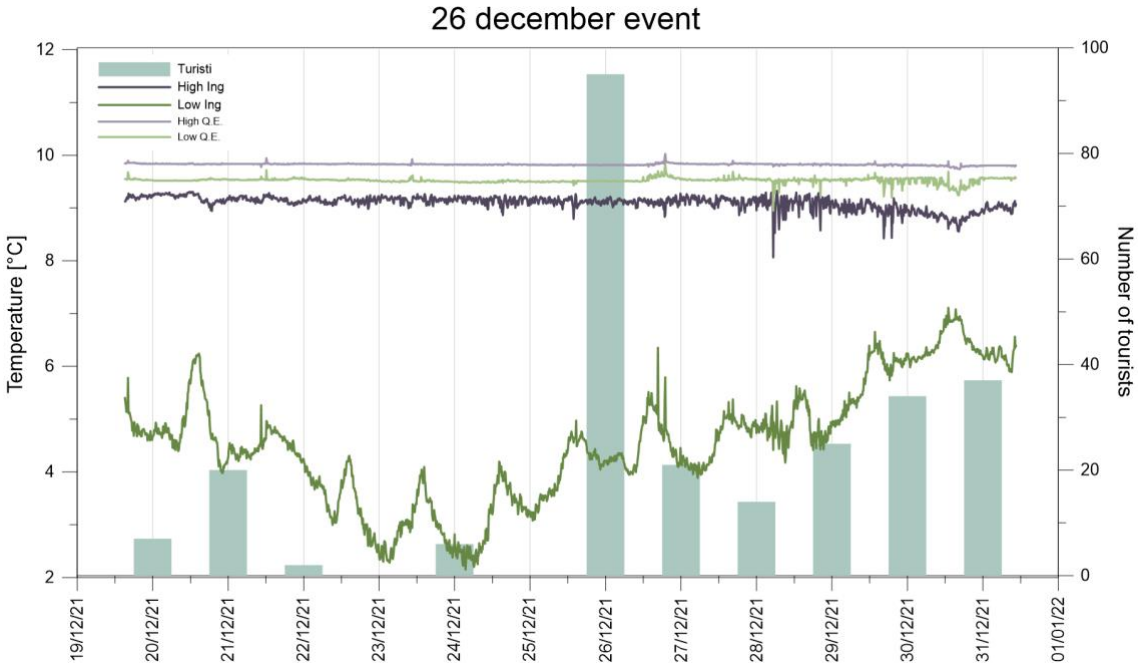

Figure 6.2 Air temperatures during the 26th of december music event

The effect of tourism on temperature measurements is also evident during peak tourist periods, such as August (Figure 6.3), where multiple peaks are observed only during the cave's operating hours, caused by groups of people passing through. This highlights the significance of analyzing the tourist flow.

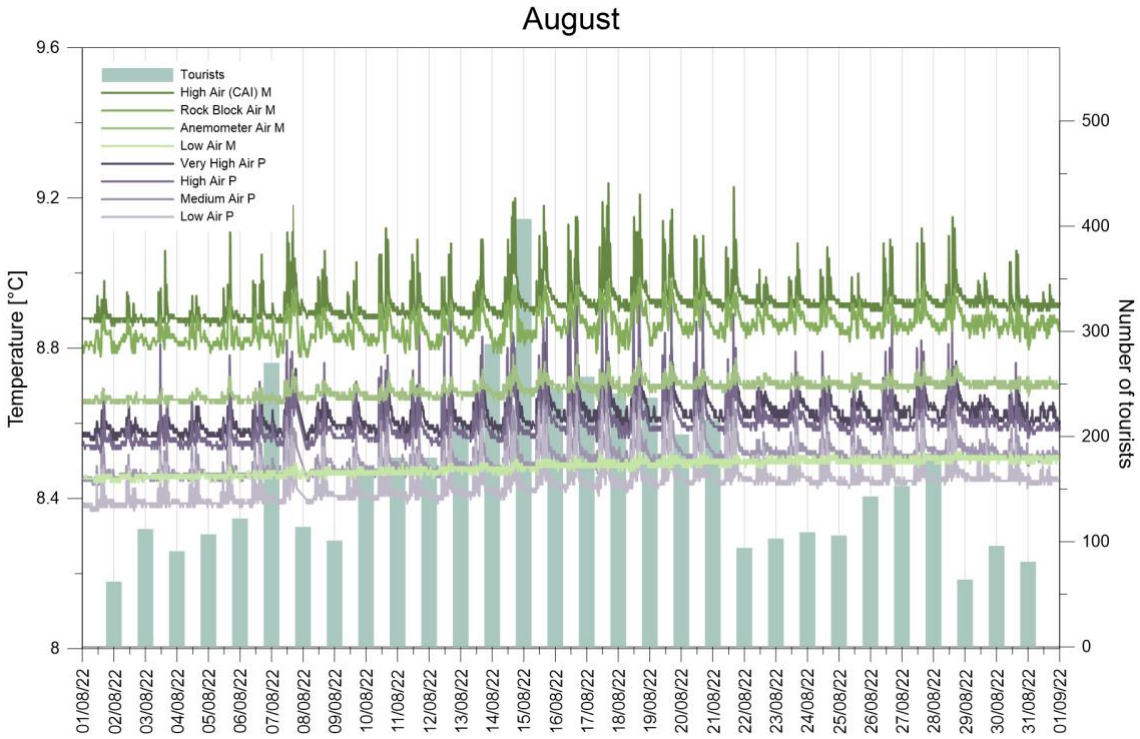

Figure 6.3 Comparison between tourist flux and august temperatures

6.1 Fourier transform and moving mean

Noting the importance of the influence of the flow of tourists, emerges the need to be able to separate two types of effects on temperature:

- The first is that of long-term effects, i.e. the seasonal effect, the decrease in temperatures due to snowmelt or flood events. This type of effect has a frequency of less than one day.
- The second concerns the influence of human body heat emission and other possible types of daily cycles. This type of effect has a higher frequency than daytime.

These two types of effects are divided by two different methods: the Fourier transform and the moving average.

6.1.1 Fourier transform

The Fourier transform (FT) is an operation to obtain the frequency content of a signal. The basic idea is that a signal can always be thought of as a superposition of sinusoidal functions of different frequencies. In this case, we are interested in separating the signal between lower and higher frequencies, so that they can then be transformed by means of an inverse transform into two different signals purified of the components with particular frequencies.

We thus transform the signal from a datum expressed in time (original signal), to a signal in which on the x-axis we find the frequencies, on the y-axis the amplitude. From this graph, frequencies greater than 1/86400, equal to $1{,}157 \times 10^{-5}$ Hz, are extracted (using the high pass filter, HPF), frequencies less than and equal to $1{,}157 \times 10^{-5}$ Hz are extracted using the low pass filter (LPF).

This type of analysis was applied, by way of example, to three datasets: High Air Porfiroidi (most affected by the passage of people), Low Air Porfiroidi and Rock Block Milano. The results are reported respectively in Figure 6.4, Figure 6.5 and Figure 6.6.

Especially from the two Porfiroidi datasets, it can be seen that the division of the data was fruitful. In the series where the high pass filter was applied, the data oscillates around zero. Rock Block Milano is the sensor least affected by the tourist passage among the three and it is in fact the one for which the greatest amount of negative values can be found. For the Porfiroidi sets (especially for high air), it can be seen that the variability of the data during August is mainly maintained during the set to which the HPF was applied, while the set to which the LPF was applied maintains a clear annual trend and an

average close to that of the original data set. The latter is, as desired, the only one affected by decreasing temperatures during flood events (as seen in Figure 6.5).

Note how the 26 December event, visible in all three datasets, is also correctly extracted from the HPF.

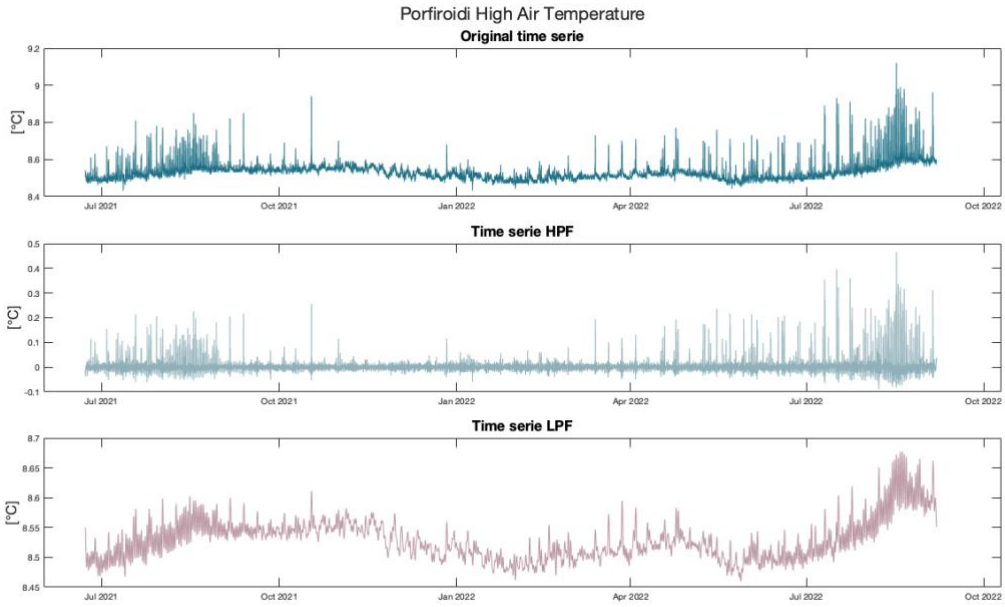

Figure 6.4 Porfiroidi High Air

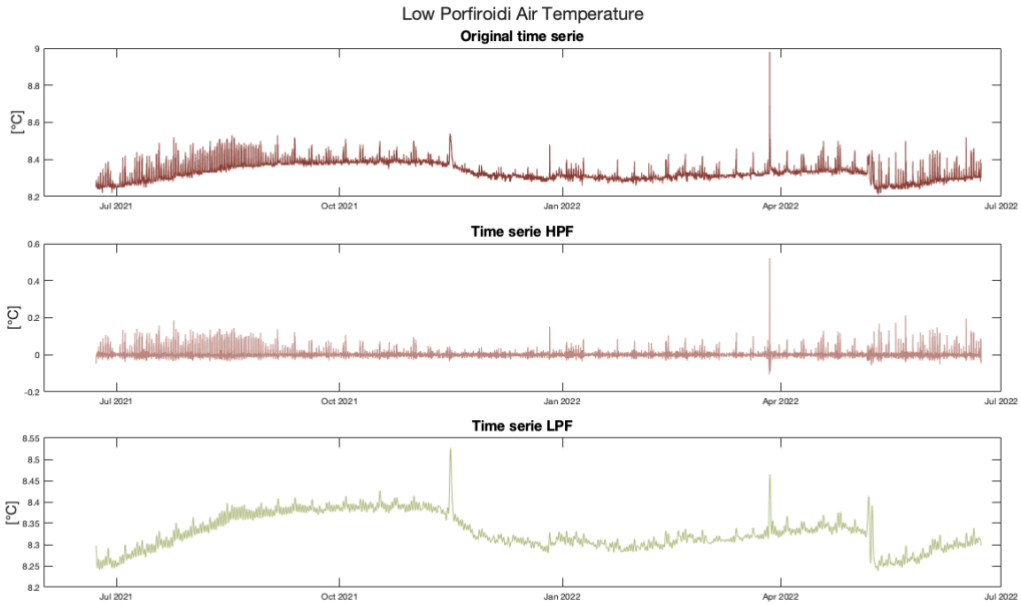

Figure 6.5 Porfiroidi Low air

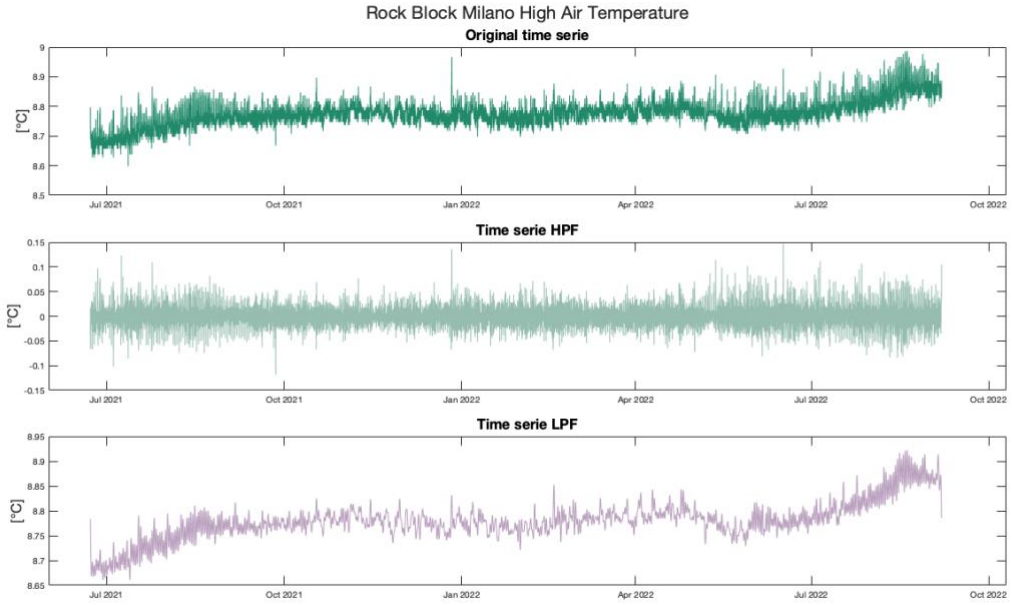

Figure 6.6 Milano Rock Block Air

6.1.2 Moving average

The same results can be obtained by applying the Moving Average (MA), which is, however, a simpler tool both to apply and to understand. Starting from the original data set, the averaged vector (thus representing the overall trend) is obtained by sequential application of the average over a data window of predefined length, which is shifted forward by one value each cycle. The use of different window lengths (12, 24 and 48 hours) for the three vectors taken as examples was evaluated.

As can be seen from the results, larger windows return a smoother trend, while including more data in the short-term effects. Note how the peaks due to the passage of groups during the summer season are in this case almost completely excluded from the long-term effects and included in the short-term ones. On the other hand, information on the general trend of rising temperatures due to the increase in outdoor temperatures is retained (the summer season coincides with both the hottest time of the year and the period with the greatest tourist influence).

The results obtained through the application of the 12h and 24h length windows are very similar to those obtained from the application of the Fourier transform, returning a trend still influenced by a large amount of short-term effects. The peaks coinciding with the Sundays of greatest tourist influx are still clearly visible in the long-term effects in the 12h window MA. Information about the effects of flooding and infiltration of water from snowmelt is correctly preserved in the long-term effects from all three averaging window lengths.

Results are shown in Annexes C-K.

7 CO_2 analysis

Not only does the tourist effect cause an increase in cave temperatures, it also affects the levels of carbon dioxide (Dragovich & Grose, 1990), which is a crucial element in speleogenesis, as previously discussed. Cave CO_2 levels can vary from the normal atmospheric levels of approximately 410 ppm to two orders of magnitude higher, as evidenced by studies such as Batiot-Guilhe et al., 2007, Ek & Gewelt, 1985 and Houillon et al., 2017. According to Kukuljan et al. (2021), the sources of CO_2 in caves are primarily the degassing of water from the main collector or secondary drips, advection and diffusion from soil for the decomposition of organic matter (Pla et al., 2016), anthropogenic respiration, and geogenic production. Additionally, soil is responsible for emitting the largest amount of CO_2 in the terrestrial ecosystem, according to Goffin et al. (2014) and .Ryan & Law (2005)

The carbon dioxide concentration trends also show cycles of varying magnitude: on the one hand, as can be seen in Figure 7.4 for the laboratory site, there are daily cycles, influenced by the anthropic presence. On the other hand, there are annual cycles. During the period 01/01/21-01/05/21 (Figure 7.1), the tourist presence was almost absent due to the COVID-19 regulations. Surprisingly, the average of CO_2 levels during that period are higher than those in 2022 (Table 7.1), This observation highlights the presence of a second major source of CO_2 originating from natural factors, such as direct diffusion and/or convection from the ground and the decomposition of organic matter washed down into the unsaturated zone (Pla et al., 2016).

Table 7.1 CO_2 levels at high and low main laboratory

	2021 [ppm]	2022 [ppm]
High laboratory	857.7	823.1
Low laboratory	882.3	847.4

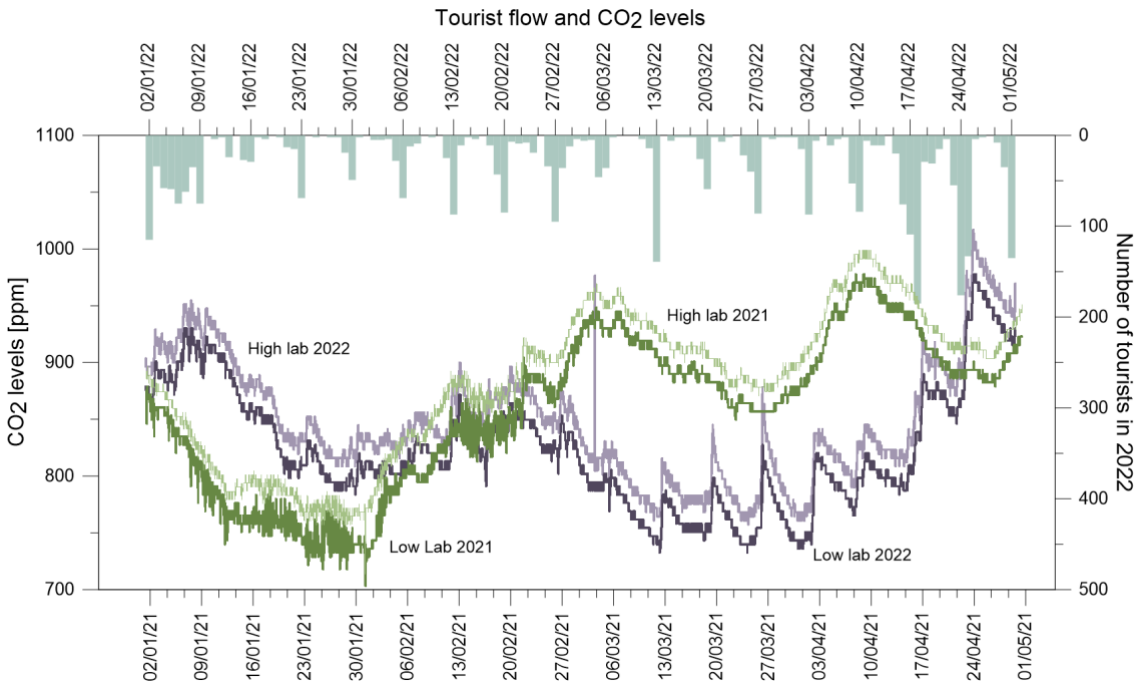

Figure 7.1 CO_2 levels for the periods 01/01/2021-01/05/2021 (in green shades) and 01/01/2022-01/05/2022 (in violet shades) compared to tourism flux

During the peak tourism season, there is a concurrent increase in soil carbon dioxide levels, which poses a challenge in distinguishing natural and human-induced effects. The cavity has four locations for measuring CO_2 levels, including two in the main laboratory above and below the access path, and two newly installed ones as of May 17th, 2022, at the weir upstream of the Ernestina waterfall. In Figure 7.2 shows the number of daily visitors in 2021 and 2022 compared with CO_2 levels. The two values show a parallel trend except for the beginning of 2021, where there was no tourist flow due to the closure for COVID-19. In that period, the trend seems to be very similar to that of the same period in 2022.

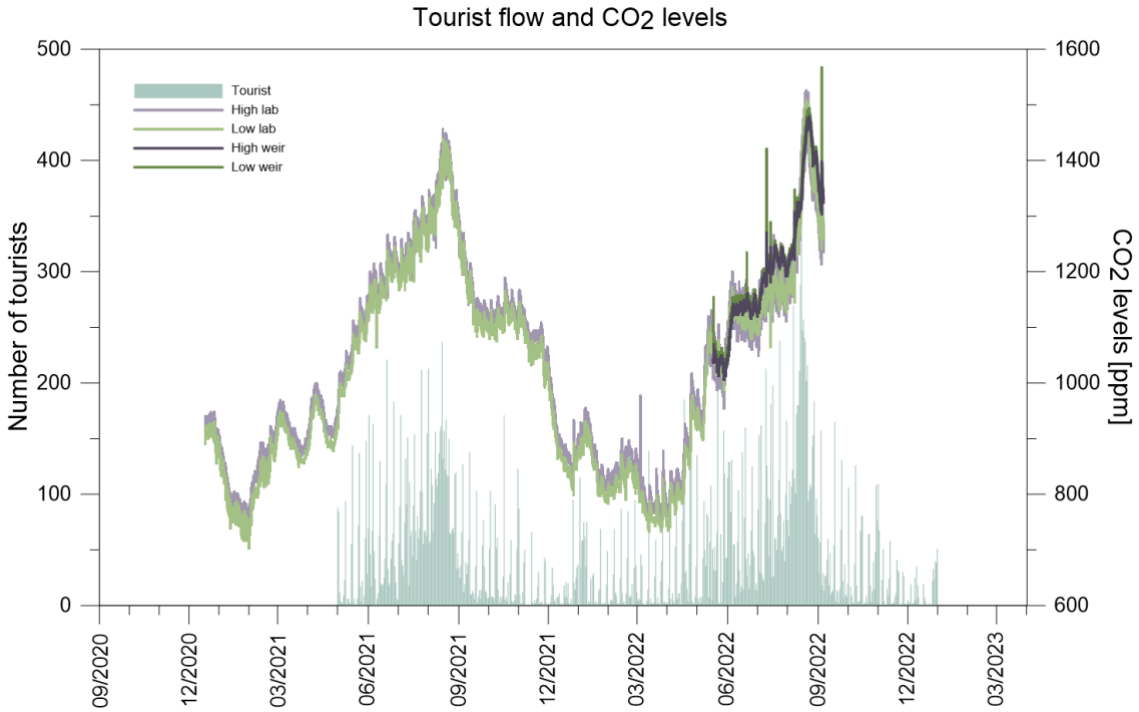

Figure 7.2 Daily visitors and CO_2 levels

Table 7.2 Annual averages of CO_2 levels at the main laboratory

	High laboratory [ppm]	**Low laboratory [ppm]**
Dec 2020 - Dec 2021	1013.6	1031.3
Sept 2021 – Sept 2022	1040.7	1060.8

The annual averages are shown in Table 7.2. They were calculated for the period December 2020-December 2021 and the period September 2021-September 2022.

It was not possible to calculate annual averages for newly installed sensors at the weir, due to the small amount of data available. The differences between the averages of the data available at the weir and the same number of data at the main laboratory were therefore calculated in order to compare the levels. The period runs from the date of installation of the new instruments (17/05/2022) to the last available data (dated 06/09/2022).

Table 7.3 17/05/2022-06/09/2022 period CO_2 average values

Sensor	Average [ppm]
Low Laboratory	1189.0
High Laboratory	1196.2
Low Weir	1218.5
High Weir	1208.1

Although there is limited data to draw general conclusions, it is worth noting that CO_2 levels are typically higher at the weir site compared to the laboratory. Specifically, the sensor at the weir with the highest readings records the highest levels. In contrast, at the laboratory, the sensor with the highest readings is the one located closest to the tourist passage, but it records lower levels than the other sensors.

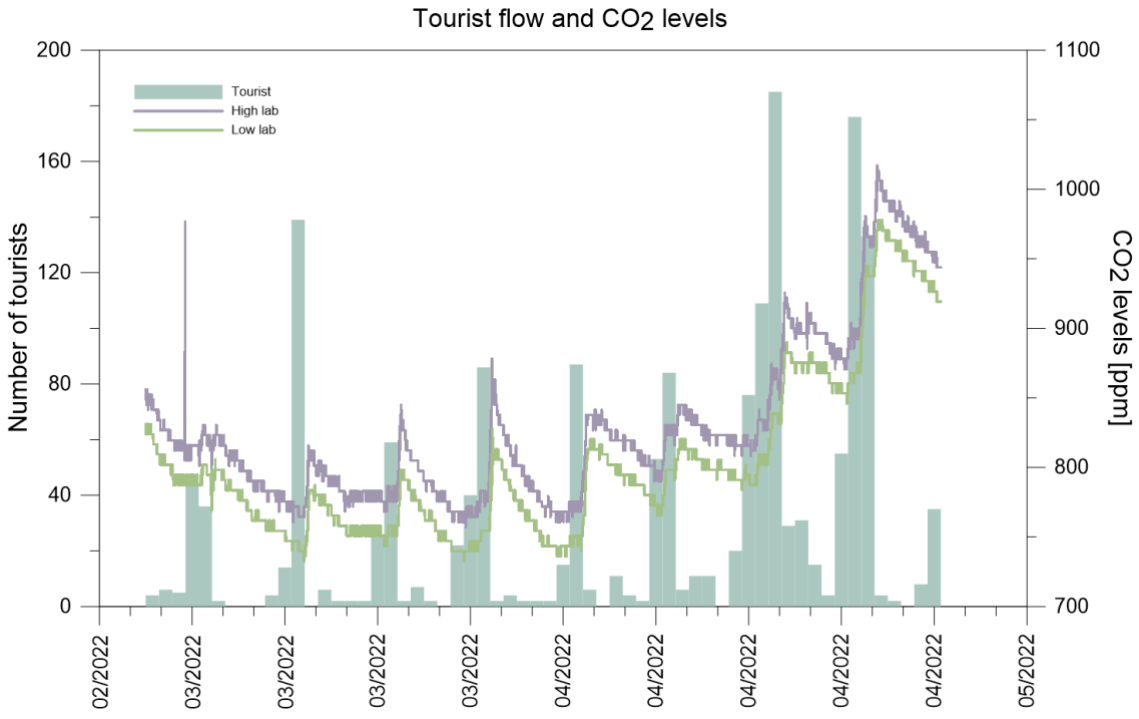

Figure 7.3 Weekly peaks of co2 levels at the main laboratory

Figure 7.3 of the dataset shows that during a period of high tourist activity, particularly on Sundays, the maximum peaks for CO_2 levels at the laboratory coincide with Sunday evenings. Additionally, when examining the August dataset, which includes CO_2 levels for both the laboratory and weir sites, the values for the main halls of the laboratory display daily cycles with a peak trend that corresponds with the evening of August 19, 2022. The weir site also shows the same overall trend as the laboratory, but with smaller daily cycles, and the peak is slightly dampened and shifted forward to August 22, 2022. Similar shifts can also be observed for weekly peaks.

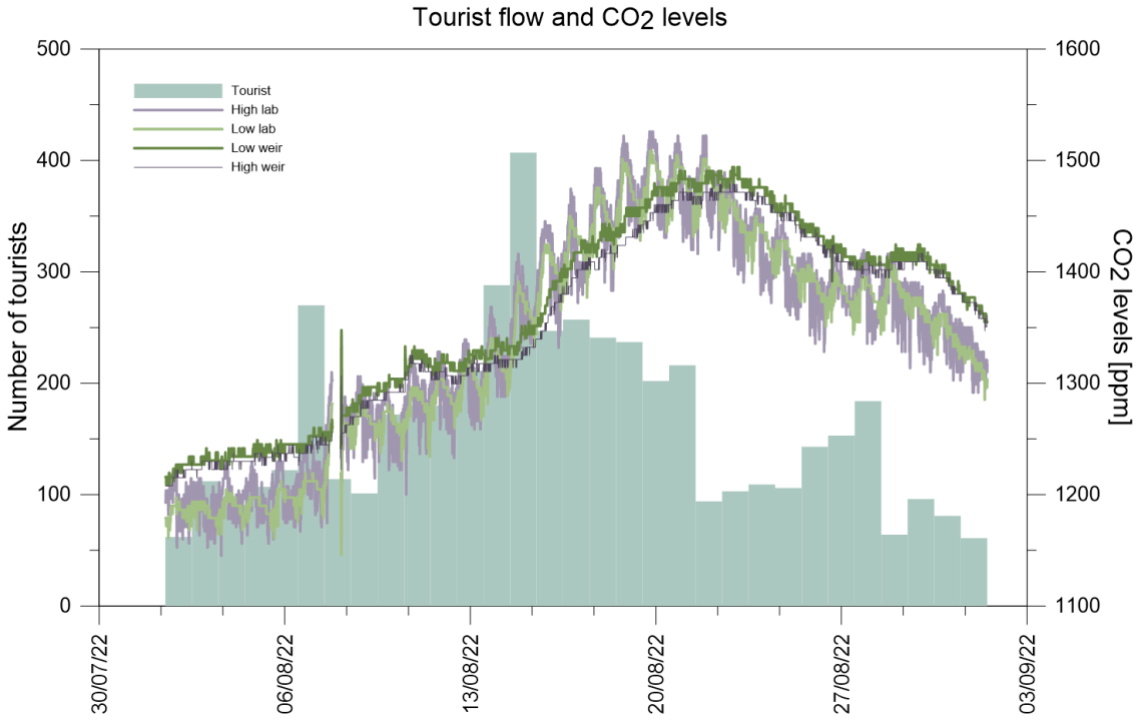

Figure 7.4 Trend of co2 levels during August 2022 at the main laboratory and weir.

The presence of CO_2 levels caused by touristic flux in the deepest part of the cave suggests that the canyon area is affected by the convective cell described above. Specifically, the CO_2 emitted by the tourist passage is transported to the parts not accessible to tourists with a delay of approximately three days.

The second source of CO_2 investigated concerns carbon dioxide from the main collector and transferred to the cave atmosphere through outgassing. CO_2 in water can escape into

the air through a process called outgassing. When the concentration of CO_2 in the air is lower than the concentration of CO_2 in the water, the CO_2 molecules in the water will diffuse across the air-water interface and enter the air. This process is influenced by factors such as temperature, pressure, and turbulence in the water. For example, as water temperature increases, the solubility of CO_2 in water decreases, making it easier for CO_2 to escape into the air. Similarly, increased turbulence in the water, such as from rapids or waves, can increase the rate of outgassing.

Figure 7.5 and Figure 7.6 show that some of the flood peaks are accompanied by an increase in CO_2. However, these increases are not significant enough to consider CO2 from the main collector as the main source of CO2 in the cave. In fact, the peaks caused by tourist inflow are of the same magnitude, as indicated by the April months in Figure 7.6.

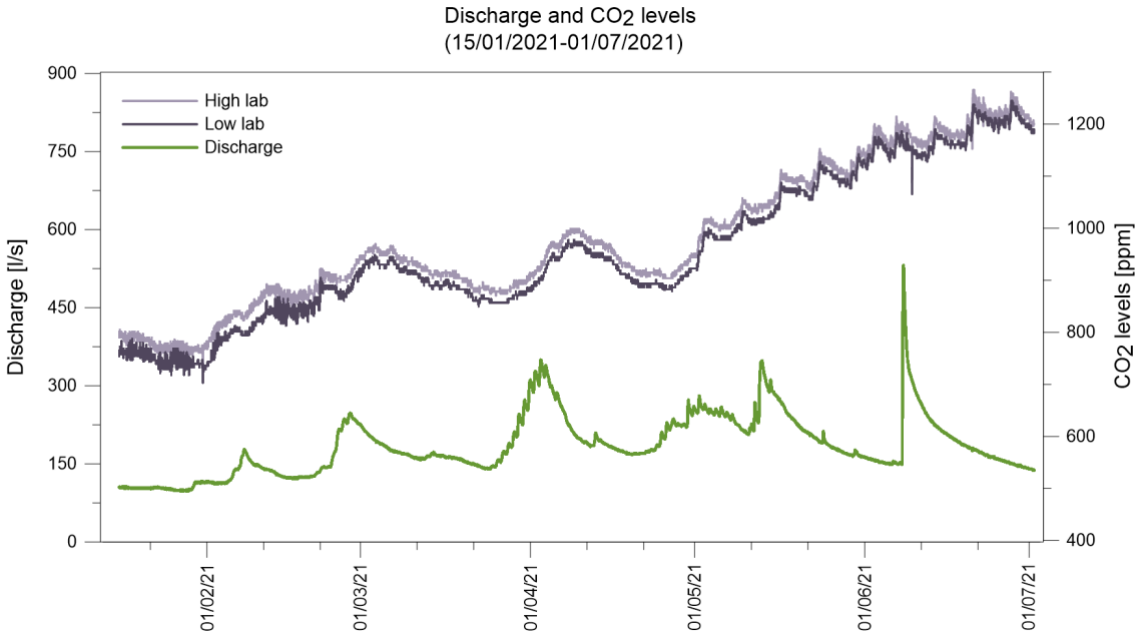

Figure 7.5 Main collector discharge and CO_2 levels during flood events in 2021

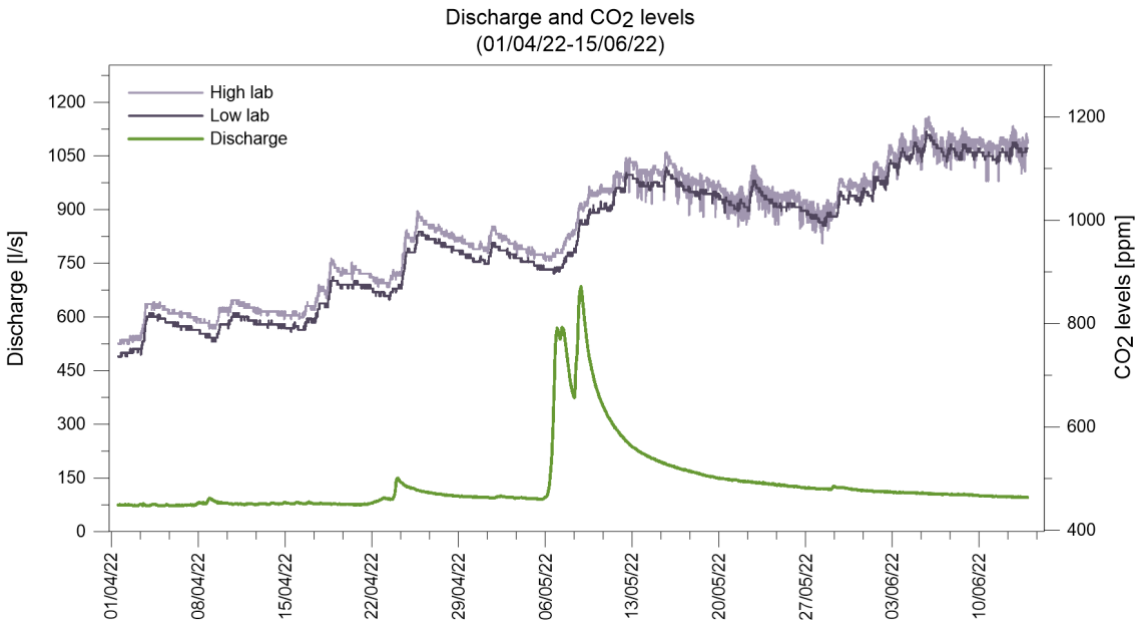

Figure 7.6 Main collector discharge and CO_2 levels during flood events in 2022

8 Conclusions

In conclusion, this study investigated the airflow mechanisms in a cave system to better understand how air circulates and ventilates within the cave environment. The aim was carried out thanks to the dense network of probes both inside and outside the cave.

The study findings encompassed three primary themes, including the identification of two distinct convective cells within the cave, the impact of human activity on temperature levels, and the correlation between human presence, flooding events and CO_2 fluctuations.

By analyzing two datasets which displayed different patterns of behavior, specifically the corridor and main hall sections of the cave, the presence of two convective cells within the cave was confirmed. Evidence of this was found in the significant summer fluctuations observed in the upper section of the cave entrance and the pronounced winter fluctuations in the lower section. These fluctuations suggest that the air entering the cave stabilizes in temperature before exiting with near-constant values. More precisely, during the summer, the air exits the cave from the lower section, while during the winter, it exits from the upper section, as shown in Figure 5.5.

However, the same phenomenon is not evident in the sensors located deeper within the cave. In this region, temperatures among probes from the same site show similar trends. The altitude of the catchment area of the karstic system is considerably higher than that of the Bossea cave. Due to the fast movement of water within the fractures that supply the main collector and the difference in altitude, the temperature of the collector is significantly lower than that of the cave environment. Consequently, an increase in flow rate, such as from snowmelt with a near-zero infiltration temperature, leads to a marked reduction in air temperature across all cave sensors, including those located far from the primary collector.

The cold water flowing at the bottom of the cave causes a dragging effect on the air above, which is subsequently pulled towards the shallower part of the main halls are. During their journey, both river and air warm up. As the air reaches the shallowest part of the halls, it is heated up and rises towards the ceiling. Being the rock inside the cave warmer than air (as illustrated in Figure 5.7, Figure 5.8, Figure 5.9 and Figure 5.10) it thus heats up the air, which is then drawn towards the deeper sections of the main halls, leading to the formation of a second convective cell. Furthermore, in standard atmosphere conditions, gradients tend to be negative as altitude increases in both the atmosphere and the cave. However, in this case, the gradients are positive precisely because of the presence of this convective cell (Figure 5.8 and Figure 5.10). The temperatures inside the cave remain relatively constant and are not influenced by seasonal changes, as demonstrated in Figure 5.23. This supports the idea that the incoming convective cell limits the exchange of air between the cave and the outside environment.

The study's second finding examined how tourist activity affects cave temperatures. Despite the large size of the main hall, the sensors in the cave were affected by the movement of tourists, as showed in Figure 6.1. To address the issue of the peak tourist season aligning with the hottest time of the year, the attempt was made to differentiate between the long-term effects (e.g., floods, snowmelt, and solar radiation) and short-term effects (i.e., the impact of people passing through) on cave temperature. The separation of long-term and short-term effects on cave temperature would allow for independent analysis and study of these effects, without being influenced by each other. To achieve this differentiation, two distinct methods were employed: the Fourier transform and the moving average. The study employed three different moving window sizes (12, 24, and 48 hours) for the moving average, and two filters (low-pass and high-pass) for the Fourier transform. The low-pass filter was used to extract short-term effects, while the high-pass filter was used for long-term effects. The results obtained from the Fourier transform closely resemble those obtained from the 12-hour moving average. However, both methods showed that the series of long-term effects was contaminated by daily peaks. This contamination was alleviated by increasing the width of the moving average

window. Notably, the 48-hour window size showed a strong correlation between the short-term effects series and the number of tourist entries.

In order to determine the preponderance of natural and anthropogenic factors, CO_2 levels were assessed in Bossea, a tourist cave that has both types of origins for carbon dioxide. The study focuses on the Sacristy and Bottom site, where approximately two years of data were collected between December 2020 and September 2022. During the initial months of 2021, Bossea cave was closed to the public, providing an opportunity to compare the CO_2 data from that period to the same period in 2022 when there was tourist activity (Figure 7.1). It's interesting to note the correlation between CO_2 levels and tourist arrivals (Figure 7.4), indicating the impact of human activities on the environment. However, the presence of higher average CO_2 levels in the absence of tourist flow suggests that natural sources of CO_2 also play a significant role. The observation that CO_2 levels are highest during the hottest time of the year aligns with the fact that soil naturally releases CO_2 during warm temperatures. Once again, the high laboratory dataset was analyzed using a moving average technique to differentiate between the short-term and long-term effects. This approach helped to highlight the underlying trends and patterns by extracting any fluctuation due to anthropic breathing.

Despite the comprehensive nature of this study in investigating the thermal exchange of the cave, several questions remain unanswered and provide a basis for future research in this field.

One of the topics that remains open for further research is the delineation of the heat exchange of the more superficial convective cell with the outside world, as well as the exchange between the two cells in terms of both thermal energy and flow rate. To achieve this, more sensitive anemometers could be installed. By combining the data from these anemometers with the dimensions of the cross-sections obtained by laser scanner survey in 2019, a quantitative determination of the flow rate of air entering and leaving the cave could be obtained, rather than the qualitative determination provided by this study.

Although this study aimed to comprehensively understand the factors involved in the thermal exchange of the Bossea cave, it did not discuss in detail the heat exchange between rock and air, as well as the propagation of heat in the rock. Since a considerable number of sensors have been installed at different depths throughout the cave, a more detailed analysis of the gradients, in correlation with the temperature at the surface, can provide valuable insights into the air circulation in not only Bossea but also other caves. Therefore, further investigation is required to better comprehend the relationship between rock temperature and air temperature and how they impact each other in the cave environment. The Sacrestia site, which exhibits interesting data for rock temperature, should also be included in further research.

9 Bibliography

Affolter, S., Häuselmann, A. D., Fleitmann, D., Häuselmann, P., & Leuenberger, M. (2015). Triple isotope (δD, δ17O, δ18O) study on precipitation, drip water and speleothem fluid inclusions for a Western Central European cave (NW Switzerland). *Quaternary Science Reviews*, *127*, 73–89. https://doi.org/10.1016/j.quascirev.2015.08.030

Antonellini, M., Nannoni, A., Vigna, B., & De Waele, J. (2019). Structural control on karst water circulation and speleogenesis in a lithological contact zone: The Bossea cave system (Western Alps, Italy). *Geomorphology*, *345*. https://doi.org/10.1016/j.geomorph.2019.07.019

Badino G. (1995). Fisica del clima sotterraneo. In *Mem. Ist. Ital. Speleologia Ser. II: Vol. Vol. 7* (1st ed.). Istituto Italiano di Speleologia.

Badino G. (2010). Underground meteorology - "What's the weather underground?" *ACTA CARSOLOGICA 39/3*, 427–448.

Badino, G., & Chignola, R. (2019). Fluctuations of Atmospheric Pressure and the Sound of Underground Karst Systems: The Antro del Corchia Case (Apuane Alps, Italy). *Frontiers in Earth Science*, *7*. https://doi.org/10.3389/feart.2019.00147

Batiot-Guilhe, C., Seidel, J.-L., Jourde, H., Hébrard, O., & Bailly-Comte, V. (2007). Seasonal variations of CO_2 and ^{222}Rn in a mediterranean sinkhole - spring (Causse d'Aumelas, SE France). *International Journal of Speleology*, *36*(1), 51–56. https://doi.org/10.5038/1827-806X.36.1.5

Chen, Z., Auler, A. S., Bakalowicz, M., Drew, D., Griger, F., Hartmann, J., Jiang, G., Moosdorf, N., Richts, A., Stevanovic, Z., Veni, G., & Goldscheider, N. (2017). Le programme de la Carte Mondiale des Aquifères Karstiques: concept, procédure de

cartographie et carte de l'Europe. *Hydrogeology Journal*, *25*(3), 771–785. https://doi.org/10.1007/s10040-016-1519-3

Covington, M. D., & Perne, M. (2015). Consider a cylindrical cave: A physicist's view of cave and karst science. In *Acta Carsologica* (Vol. 44, Issue 3, pp. 363–380). Zalozba Z R C. https://doi.org/10.3986/ac.v44i3.1925

Dai, Q., Peng, X., Yang, Z., & Zhao, L. (2017). Runoff and erosion processes on bare slopes in the Karst Rocky Desertification Area. *Catena*, *152*, 218–226. https://doi.org/10.1016/j.catena.2017.01.013

De Freitas, C. R. (1987). Cave climate: Assessment of Heat and moisture exchange. In *JOURNAL OF CLIMATOLOGY* (Vol. 7).

De Freitas, C. R., & Schmekal, A. (2006). Studies of condensation/evaporation processes in the Glowworm Cave, New Zealand. *International Journal of Speleology*, *35*(2), 75–81. https://doi.org/10.5038/1827-806X.35.2.3

Domínguez-Villar, D., Fairchild, I. J., Baker, A., Carrasco, R. M., & Pedraza, J. (2013). Reconstruction of cave air temperature based on surface atmosphere temperature and vegetation changes: Implications for speleothem palaeoclimate records. *Earth and Planetary Science Letters*, *369–370*, 158–168. https://doi.org/10.1016/j.epsl.2013.03.017

Dragovich, D., & Grose, J. (1990). Impact of Tourists on Carbon Dioxide Levels at Jenolan Caves, Australia: an Examination of Microclimatic Constraints on Tourist Cave Management. In *Geoforum* (Vol. 21, Issue 1).

Ek, C., & Gewelt, M. (1985). Carbon dioxide in cave atmospheres. New results in belgium and comparison with some other countries. *Earth Surface Processes and Landforms*, *10*(2), 173–187. https://doi.org/10.1002/esp.3290100209

Eusebio, A., Lovera, U., Milanese, N., Silvestro, C., Veerman, L., Vigna, B., Alterisio, D., Badino, G., Banzato, C., Barale, M., Bengaso, V., Bertorelli, V., Bonino, D., Calcagno, D., Domenico Cella, G., Chesta, M., Cicconetti, I., Cirillo, A., Cossutta,

F., … Gruppi Speleologici Piemontesi, A. (2010). *Atlante delle aree carsiche piemontesi*.

Gattinoni, P., & Scesi, L. (2018). Short review of some methods for groundwater flow assessment in fractured rock masses. *Acque Sotterranee - Italian Journal of Groundwater*, *7*(3), 7–17. https://doi.org/10.7343/as-2018-342

Goffin, S., Aubinet, M., Maier, M., Plain, C., Schack-Kirchner, H., & Longdoz, B. (2014). Characterization of the soil CO2 production and its carbon isotope composition in forest soil layers using the flux-gradient approach. *Agricultural and Forest Meteorology*, *188*, 45–57. https://doi.org/10.1016/j.agrformet.2013.11.005

Goldscheider, N., Chen, Z., Auler, A. S., Bakalowicz, M., Broda, S., Drew, D., Hartmann, J., Jiang, G., Moosdorf, N., Stevanovic, Z., & Veni, G. (2020). Global distribution of carbonate rocks and karst water resources. *Hydrogeology Journal*, *28*(5), 1661–1677. https://doi.org/10.1007/s10040-020-02139-5

Gomell, A. K., Austin, D. C., Ohms, M. J., & Pflitsch, A. (2021). Air pressure propagation through wind cave and jewel cave: How do pressure waves travel through barometric caves? *International Journal of Speleology*, *50*(3), 263–273. https://doi.org/10.5038/1827-806X.50.3.2393

Houillon, N., Lastennet, R., Denis, A., Malaurent, P., Minvielle, S., & Peyraube, N. (2017). Assessing cave internal aerology in understanding carbon dioxide (CO2) dynamics: implications on calcite mass variation on the wall of Lascaux Cave (France). *Environmental Earth Sciences*, *76*(4). https://doi.org/10.1007/s12665-017-6498-8

Jeannin P-Y. (1989). Paramètres physico-chimiques des eaux dans le karst. *Centre d'hydrogéologie - Université de Neuchâtel*, *Vol. 1*.

Jeannin P-Y, Liedl R, & Sauter M. (1997). Some concepts about heat transfer in karstic systems. *Proceed. of the 8e Intern. Cong. of Speleology*.

Kašing, M., & Lenart, J. (2020). Cave airflow mechanism of a crevice-type cave: A case study from Czechia. *International Journal of Speleology*, *49*(1), 55–67. https://doi.org/10.5038/1827-806X.49.1.2285

Kukuljan, L., Gabrovšek, F., Covington, M. D., & Johnston, V. E. (2021). CO2 dynamics and heterogeneity in a cave atmosphere: role of ventilation patterns and airflow pathways. *Theoretical and Applied Climatology*, *146*(1–2), 91–109. https://doi.org/10.1007/s00704-021-03722-w

Lismonde, B. (1946-. . . .). (2002). *Climatologie du monde souterrain. Tome 1, Vent des ténèbres*. Ed. du Comité départemental de spéléologie de l'Isère.

Luetscher, M., & Jeannin, P. Y. (2004). Temperature distribution in karst systems: The role of air and water fluxes. *Terra Nova*, *16*(6), 344–350. https://doi.org/10.1111/j.1365-3121.2004.00572.x

Luetscher, M., Lismonde, B., & Jeannin, P.-Y. (2008). Heat exchanges in the heterothermic zone of a karst system: Monlesi cave. *Journal of Geophysical Research*, *113*. https://doi.org/10.1029/2007JF000892ï

Medellin, R. A., Wiederholt, R., & Lopez-Hoffman, L. (2017). Conservation relevance of bat caves for biodiversity and ecosystem services. *Biological Conservation*, *211*, 45–50. https://doi.org/10.1016/j.biocon.2017.01.012

Nannoni, A., Vigna, B., Fiorucci, A., Antonellini, M., & De Waele, J. (2020). Effects of an extreme flood event on an alpine karst system. *Journal of Hydrology*, *590*. https://doi.org/10.1016/j.jhydrol.2020.125493

Peano, G. (2002). *IL MONITORAGGIO AMBIENTALE NELLA GROTTA DI BOSSEA: PROBLEMI TECNICI E SOLUZIONI ADOTTATE*.

Pflitsch, A., Wiles, M., Horrocks, R., Piasecki, J., & Ringeis, J. (2010). Dynamic climatologic processes of barometric cave systems using the example of Jewel Cave and Wind Cave in South Dakota, USA. *Acta Carsologica*, *39*(3). https://doi.org/10.3986/ac.v39i3.75

Pla, C., Cuezva, S., Garcia-Anton, E., Fernandez-Cortes, A., Cañaveras, J. C., Sanchez-Moral, S., & Benavente, D. (2016). Changes in the CO2 dynamics in near-surface cavities under a future warming scenario: Factors and evidence from the field and experimental findings. *Science of the Total Environment*, *565*, 1151–1164. https://doi.org/10.1016/j.scitotenv.2016.05.160

Pulido-Bosch, A., Martín-Rosales, W., López-Chicano, M., Vallejos, A., & Rodríguez-Navarro, C. M. (1997). Human impact in a tourist karstic cave (Aracena, Spain). In *Environmental Geology* (Vol. 31). Springer-Verlag.

Riechelmann, D. F. C., Deininger, M., Scholz, D., Riechelmann, S., Schröder-Ritzrau, A., Spötl, C., Richter, D. K., Mangini, A., & Immenhauser, A. (2013). Disequilibrium carbon and oxygen isotope fractionation in recent cave calcite: Comparison of cave precipitates and model data. *Geochimica et Cosmochimica Acta*, *103*, 232–244. https://doi.org/10.1016/j.gca.2012.11.002

Ryan, M. G., & Law, B. E. (2005). Interpreting, measuring, and modeling soil respiration. *Biogeochemistry*, *73*(1), 3–27. https://doi.org/10.1007/s10533-004-5167-7

Salmon, F., Lacanette, D., Lharti, H., & Sirieix, C. (2023). Heat transfer in rock masses: Application to the Lascaux Cave (France). *International Journal of Heat and Mass Transfer*, *207*, 124029. https://doi.org/10.1016/j.ijheatmasstransfer.2023.124029

Šebela, S., Baker, G., & Luke, B. (2019). Cave Temperature and Management Implications in Lehman Caves, Great Basin National Park, USA. *Geoheritage*, *11*(3), 1163–1175. https://doi.org/10.1007/s12371-019-00367-0

Šebela, S., & Pipan, T. (2015). *Cave micro-climate and tourism: Karst Carbon Cycle-Quantitative physicogeographical determination for the various climate-relief types of Slovenia View project Karst research View project*. https://www.researchgate.net/publication/282986421

Šebela, S., & Turk, J. (2011). Local characteristics of Postojna Cave climate, air temperature, and pressure monitoring. *Theoretical and Applied Climatology*, *105*(3), 371–386. https://doi.org/10.1007/s00704-011-0397-9

Šebela, S., & Turk, J. (2014). Natural and anthropogenic influences on the year-round temperature dynamics of air and water in Postojna show cave, Slovenia. *Tourism Management*, *40*, 233–243. https://doi.org/10.1016/j.tourman.2013.06.011

Stevanović, Z. (2019). Karst waters in potable water supply: a global scale overview. *Environmental Earth Sciences*, *78*(23), 662. https://doi.org/10.1007/s12665-019-8670-9

Vigna, B. (2020). *Assetto geologico ed idrogeologico del Sistema carsico di Bossea (SW Piemonte, Italy)*.

Wang, S., Du, J., Li, S., He, H., & Xu, W. (2019). Impact of tourism activities on glacial changes based on the tourism heat footprint (THF) method. *Journal of Cleaner Production*, *215*, 845–853. https://doi.org/10.1016/j.jclepro.2019.01.120

Zunino M. (2020). *L'orso delle caverne del Piemonte meridionale: paleobiologia di una specie estinta e storia delle ricerche tra passato, presente e futuro*.

10 Annexes

Annex A: Outline of the convective cells direction during winter time

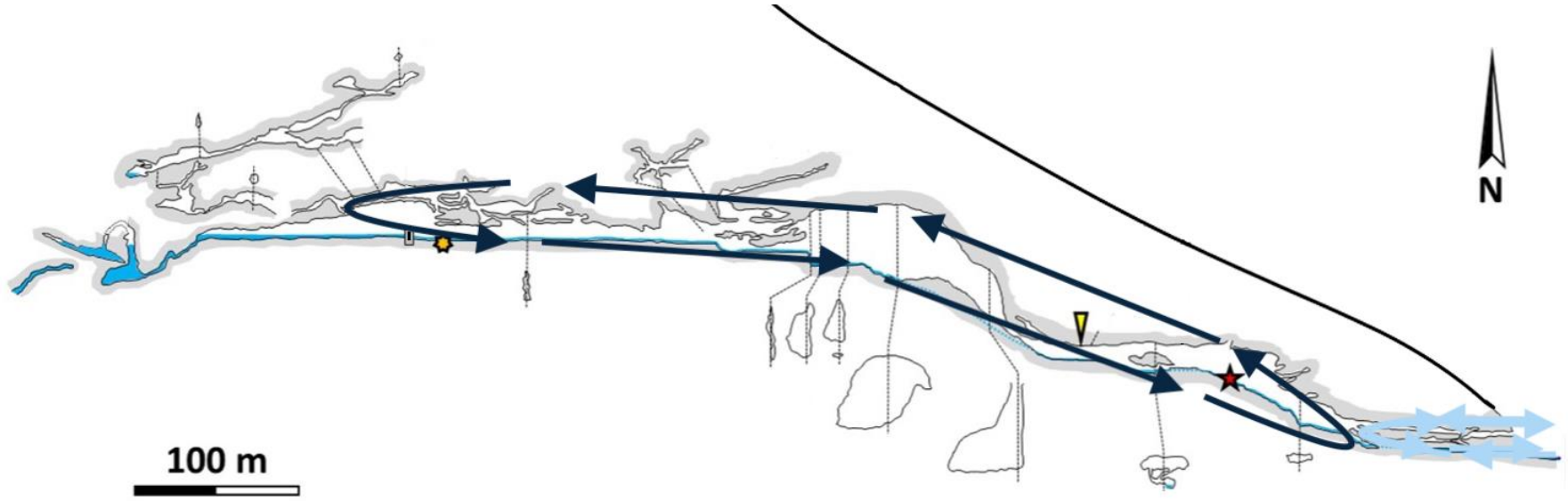

Annex B: Outline of the convective cells direction during summer time

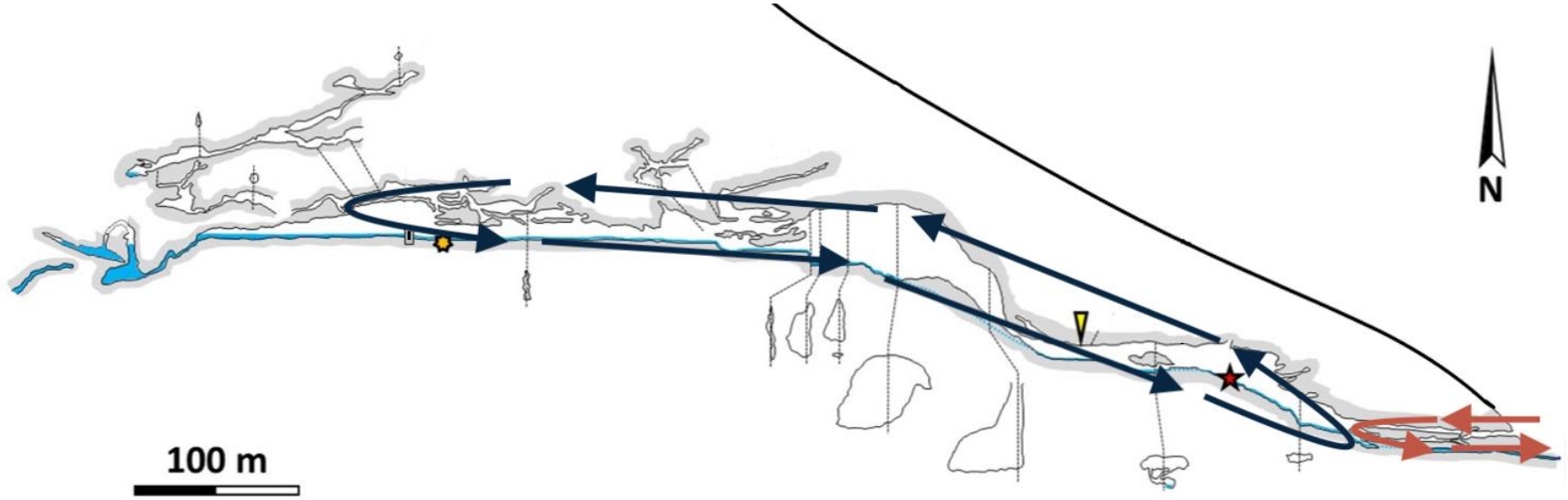

Annex C: Porfiroidi High Air Temperature 12 h

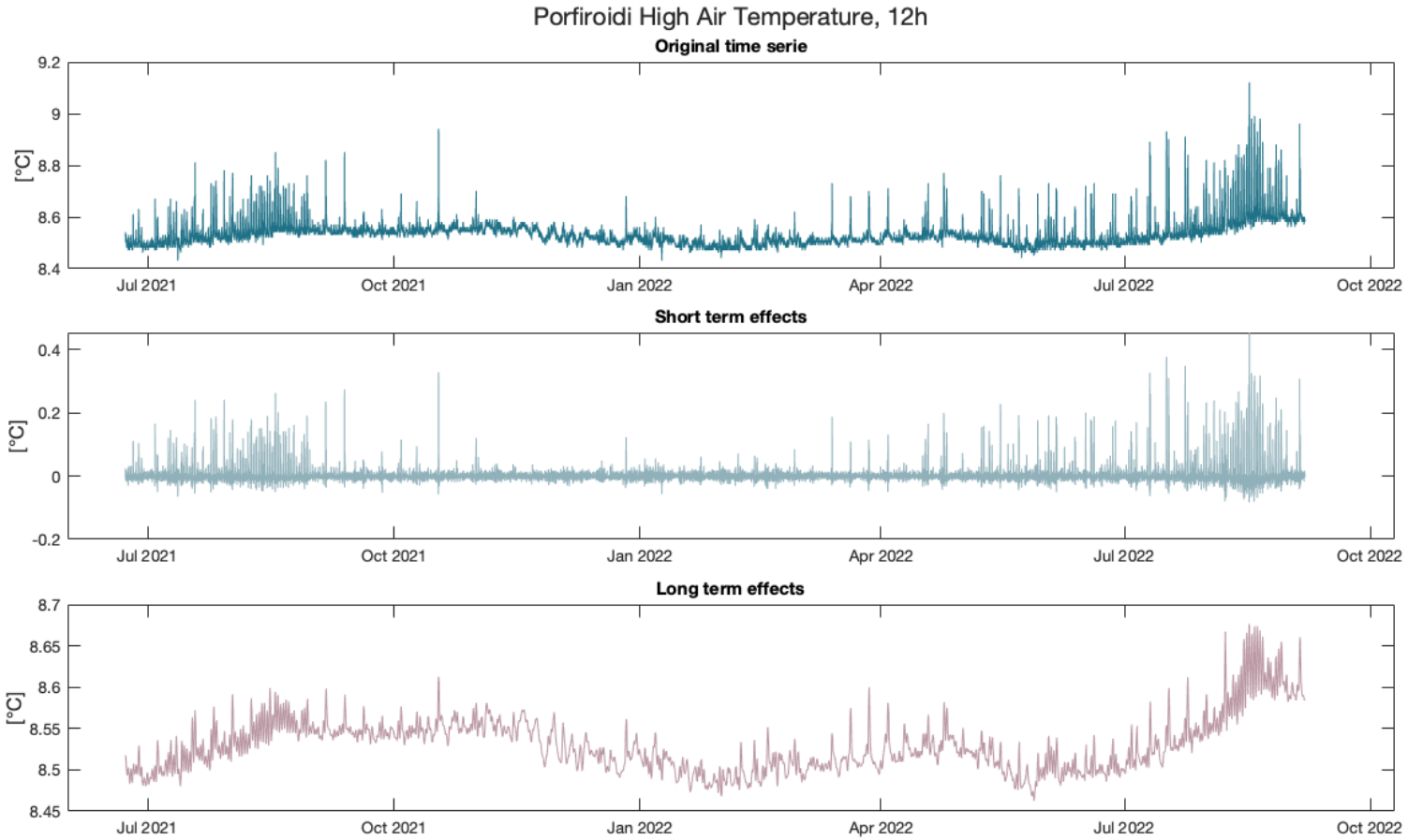

Annex D: Porfiroidi High Air Temperature 24 h

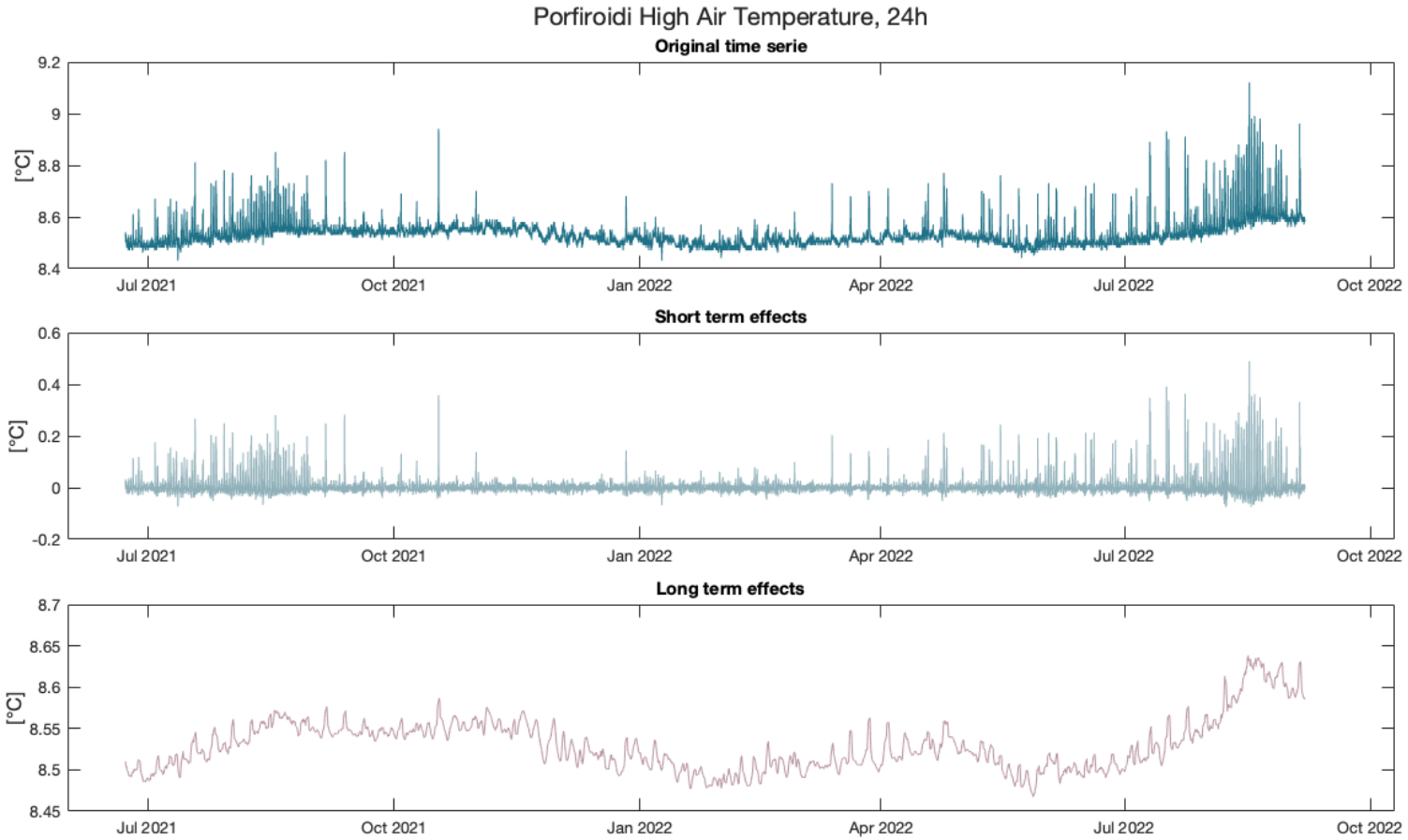

Annex E: Porfiroidi High Air Temperature 48 h

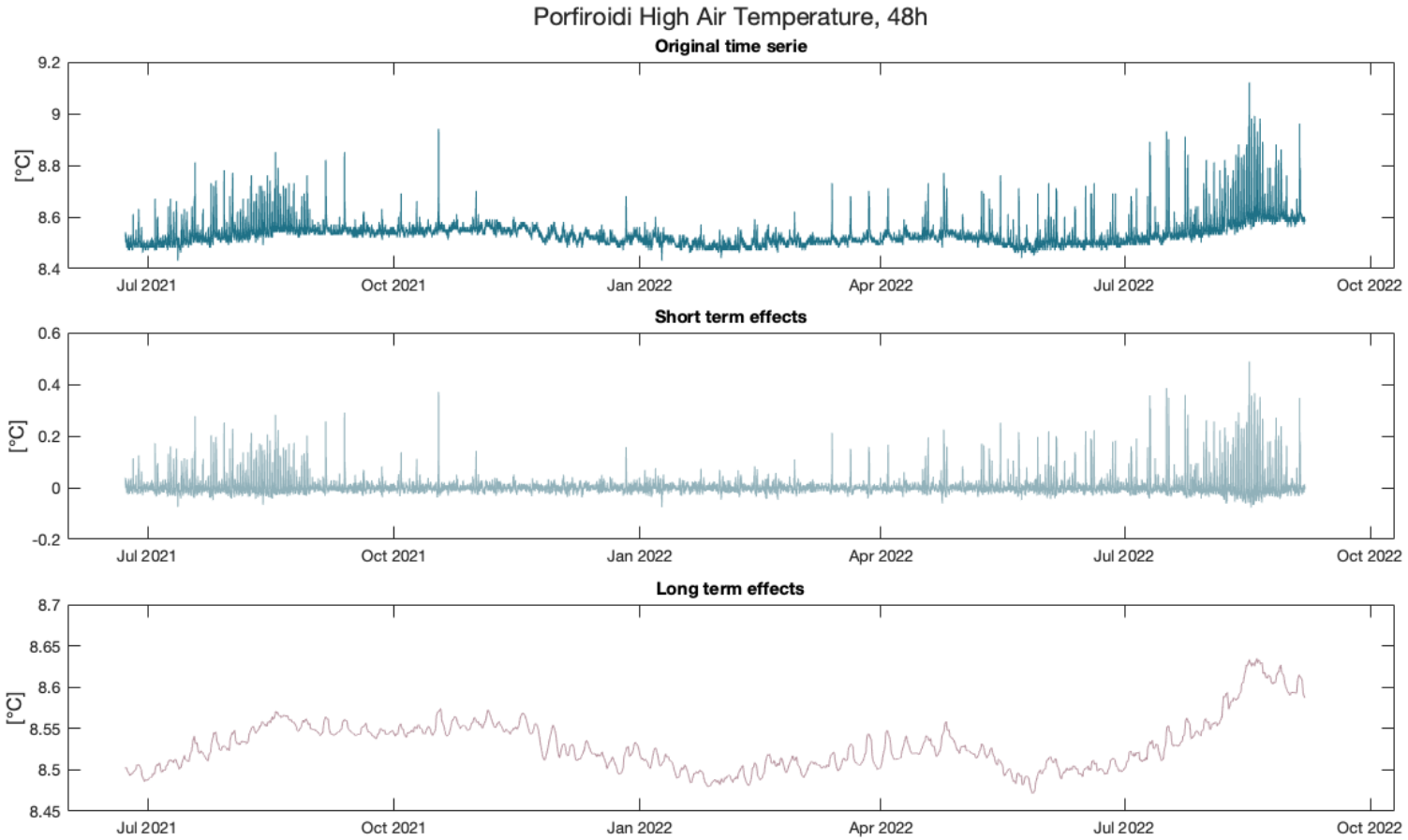

Annex F: Porfiroidi Low Air Temperature 12 h

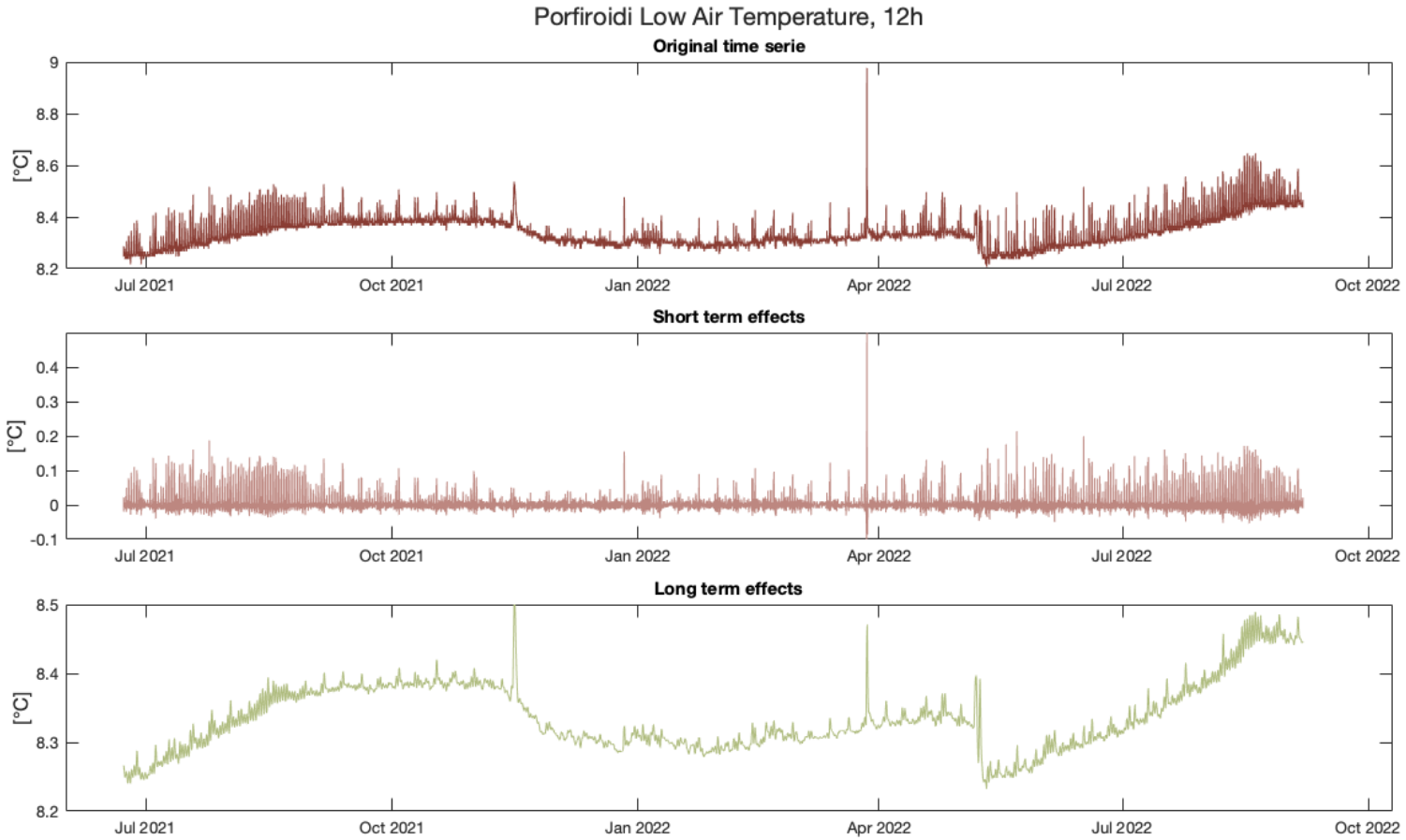

Annex G: Porfiroidi Low Air Temperature 24 h

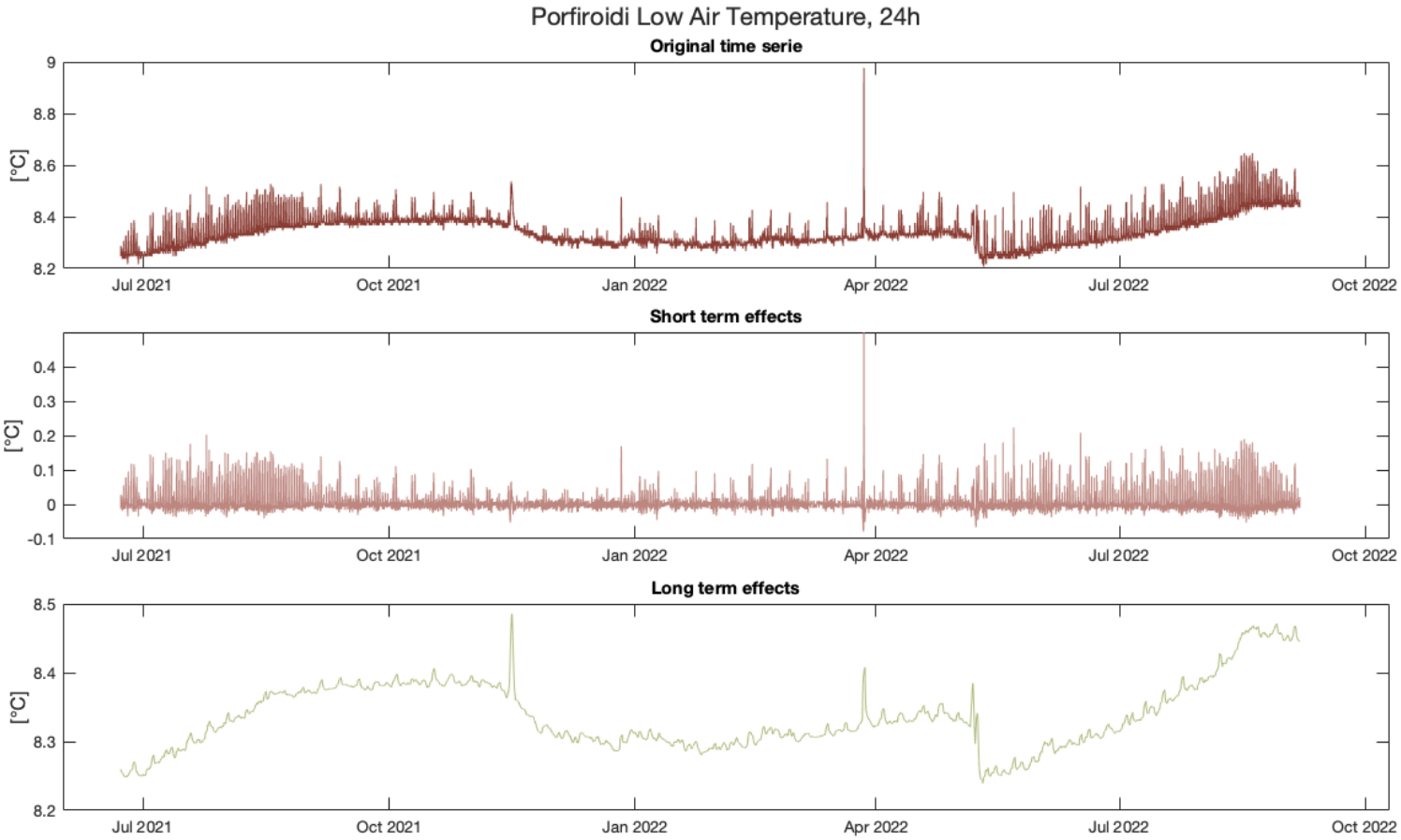

Annex H: Porfiroidi Low Air Temperature 48 h

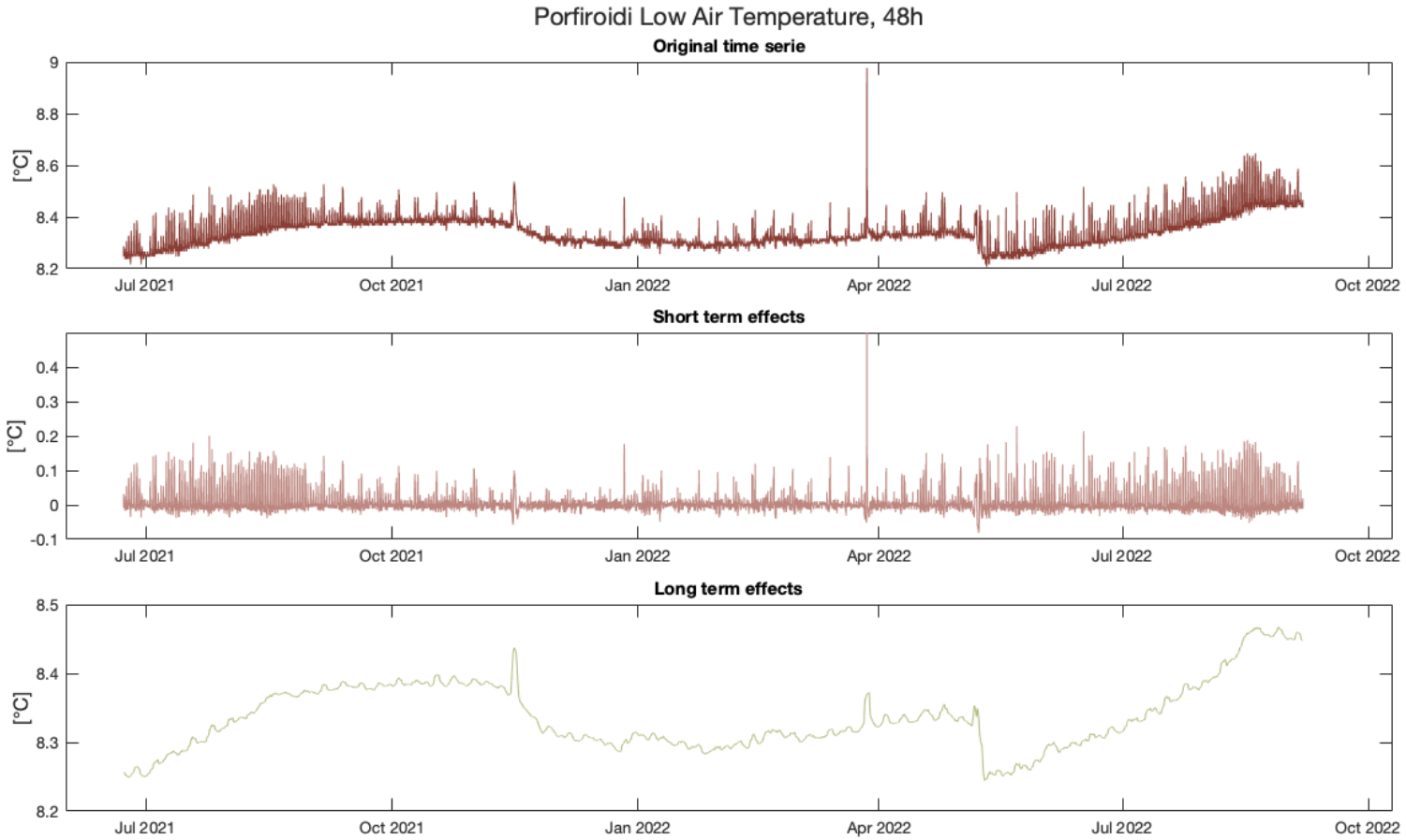

Annex I: Rock Block Air Temperature 12 h

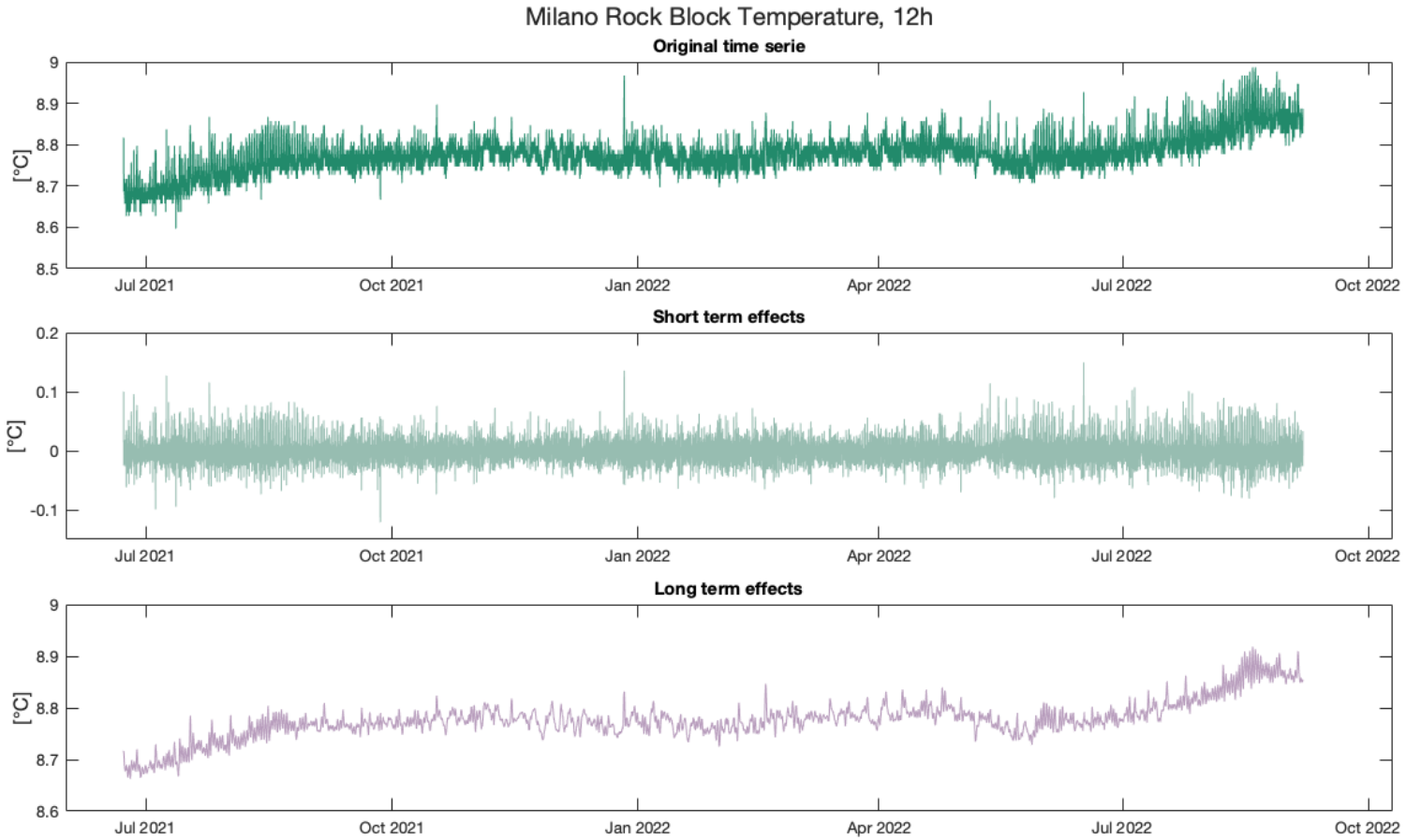

Annex J: Rock Block Temperature 24 h

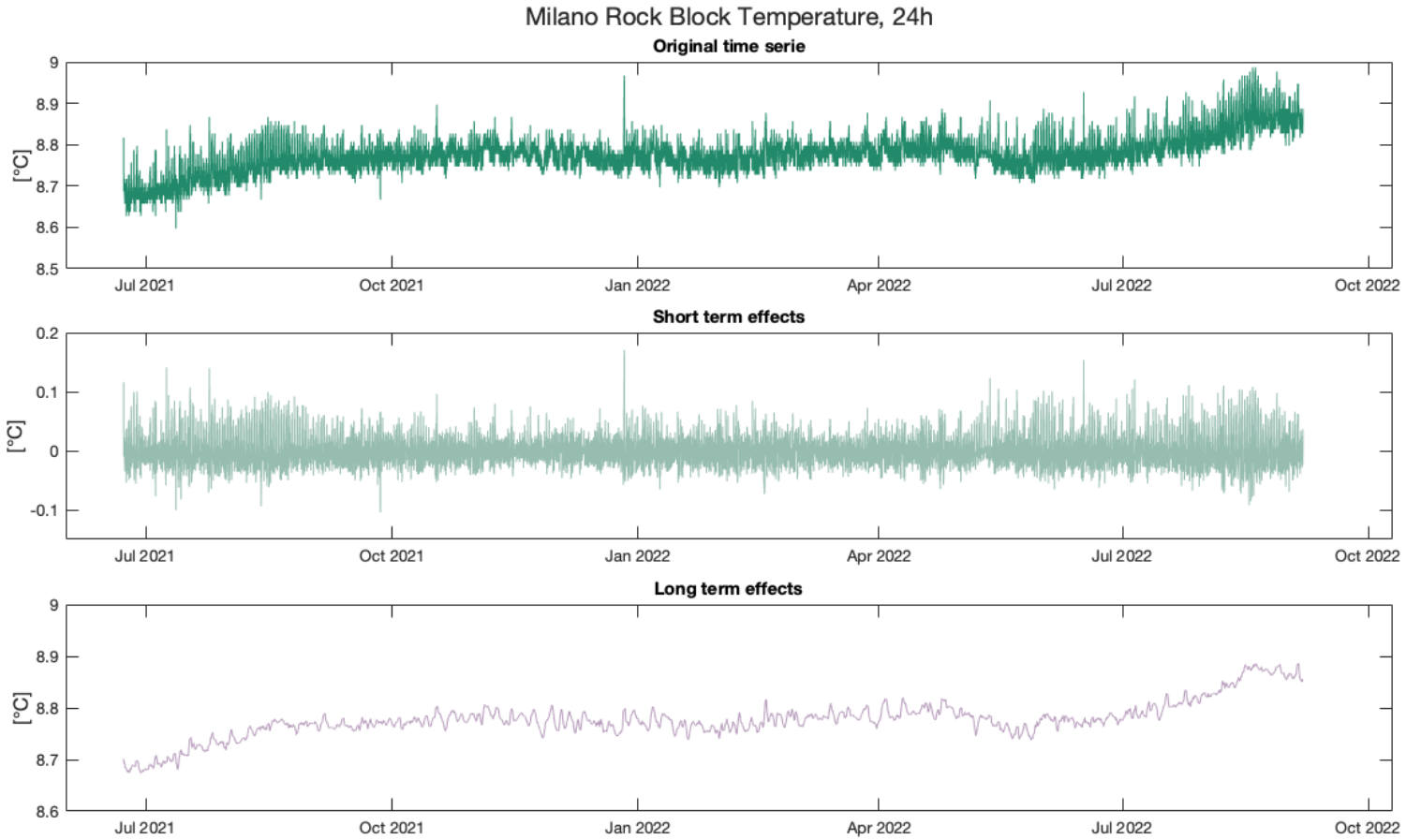

Annex K: Rock Block Temperature 48 h

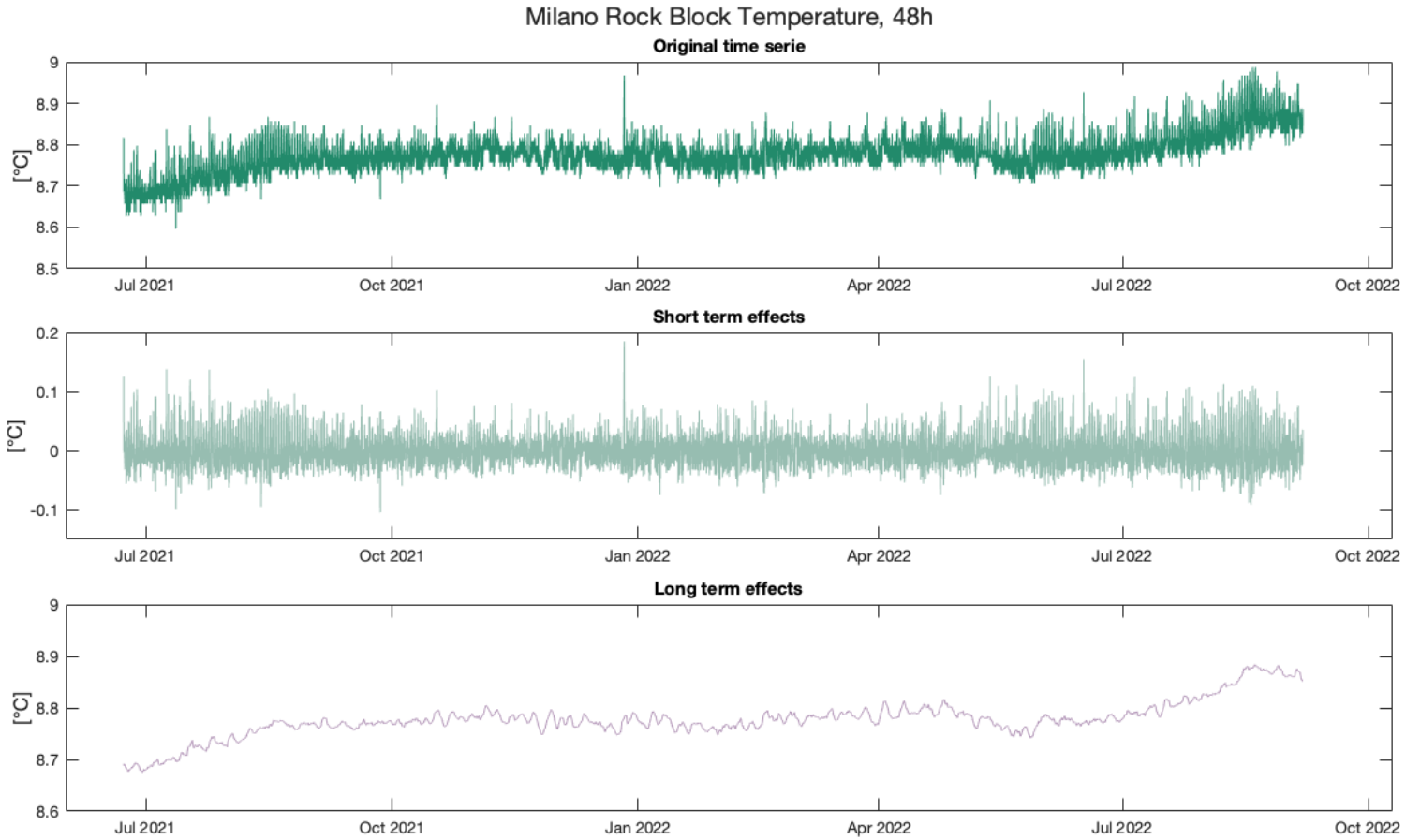

11 Acknoledgements

I would like to express my deepest gratitude to Adriano Fiorucci, Pierre-Yves Jeannin, Marc Luetscher, Amir Sedaghatkish and Bartolomeo Vigna, for their guidance, support, and expertise throughout the research process. Their invaluable feedback and constructive criticism helped shape this work and made it possible to achieve the level of quality that was required.

Specifically, I would like to express my gratitude to Claudio Pastore, whose insightful feedback, encouragement, and support at different stages of my research were crucial in bringing this project to completion.

I am extremely thankful to Gabi and Charles-Henry, welcomed me into their home but also made me feel like part of their family in Le Locle.

My sincere appreciation also goes to the staff at ISSKA for welcoming me for a few months as part of the staff.

Grazie alla mia famiglia e ai miei amici più stretti per il supporto costante che mi offrono da tutta la vita. Siete il motore di ogni mia scelta.